Quantitative live cell imaging of glucocorticoid receptor dynamics in the nucleus

Keizer, V.I.P.

QUANTITATIVE LIVE CELL IMAGING OF GLUCOCORTICOID RECEPTOR DYNAMICS IN THE NUCLEUS

VEER INGRID PAULINA KEIZER

Cover, layout-out by VIP Keizer

ISBN 978-94-6332-421-2

Printed by GVO

Research funded by FOM, NWO

QUANTITATIVE LIVE CELL IMAGING OF GLUCOCORTICOID RECEPTOR DYNAMICS IN THE NUCLEUS

Proefschrift

ter verkrijging van

de graad van Doctor aan de Universiteit Leiden,

op gezag van Rector Magnificus prof. mr. C.J.J.M. Stolker,

volgens besluit van het College voor Promoties

te verdedigen op donderdag 1 november 2018

klokke 16:15 uur

door

VEER INGRID PAULINA KEIZER

geboren te Utrecht

in 1989

Promotores:	Dr. M.J.M. Schaaf
	Prof. dr. ir. S.J.T. van Noort
Promotiecommissie:	Prof. dr. T. Schmidt
	Prof. dr. H.P. Spaink
	Prof. dr. O.C. Meijer (Leiden University Medical Center)
	Prof. dr. A. Cambi (Radboud University, Nijmegen)

Als je goed kijkt zie je dat alles verbonden is

CONTENT

1 INTRODUCTION

In this thesis, the focus lies on studying glucocorticoid receptor dynamics in living cells with the aim of understanding how this transcription factor finds its DNA target sites to regulate transcription. In addition, we have advanced the experimental techniques used to answer this question through development of novel analysis tools as well as investigations of alternative labeling methods.

1.1 THE PARADIGM

Proteins are essential for us to function properly. To make sure the right proteins are produced at the right time, the transcription of genes needs to be tightly regulated. Transcription factors do this job, by recognizing a specific DNA sequence and binding to it. This sequence can be located at the start of the gene, which is termed the promotor region, or at a more distant enhancer site. After the transcription factor has bound to the DNA, they will recruit other factors. These include, most importantly, RNA polymerase that will bind at the promotor and will initiate the transcription of a gene. This process includes partial unwinding of the double stranded DNA to form a complementary RNA strand. Not the whole sequence is translated into proteins. The introns are spliced out of the RNA transcript, such that only the coding regions, or exons, remain. This final mRNA product is then translated into protein. However, to regulate this whole process, the transcription factors must first find their specific target sites. With over a total of 6.5 billion basepairs of DNA within every human cell, and only a sequence of 5-10 nucleotides to recognize, this can be a daunting task.

1.2 NUCLEAR ORGANIZATION

In eukaryotic cells, the DNA is stored in the nucleus of the cell. The nucleus is separated from the rest of the cell by a double membrane, the nuclear envelope. To allow traffic of larger molecules, the nuclear membrane is dotted with nuclear pores through which molecules with a diameter up to 10 nm can diffuse passively (1). Proteins can also be transported actively when they carry a nuclear localization sequence (NLS) that is recognized by the nuclear pore complex. In this manner, proteins with a diameter of up to 40

nm can be translocated to the nucleus (2–4). Although the bare DNA only occupies around 0.65% of the nuclear volume (with one base pair has a volume of 1 nm^3 and a nuclear volume of 10^3 μm^3 (5,6)), there is still around 3 m of DNA that must be stored in an organized way in this compartment. Moreover, this must be done in a manner that still allows access of proteins, such as transcription factors, to the DNA. To package DNA, it is wrapped around histone proteins to form nucleosomes. Strings of nucleosomes form chromatin fibers of which the higher-order structure is a subject of active research. In turn, these fibers are folded in higher-order structures that in humans shape the 23 pairs of chromosomes. In spite of all of this compaction and organization, transcription factors can successfully bind to the DNA and initiate transcription.

1.3 MEET THE FAMILY: THE NUCLEAR RECEPTOR SUPERFAMILY

In this thesis, the glucocorticoid receptor (GR) is used as a model system to study transcription factor dynamics and distribution. This receptor is part of the nuclear receptor (NR) superfamily. Nuclear receptors are involved in the regulation of many essential processes such as reproduction, development, metabolism and the immune response. In contrast to most other receptor proteins that reside on the plasma membrane and bind molecules (ligands) that are outside the cell, nuclear receptors reside in the cytoplasm or nucleoplasm. Hence, their ligands must diffuse across the plasma membrane to activate their receptor inside the cell. Ligand binding induces a conformational change of the receptor that results in its activation. Once activated, nuclear receptors function as transcription factors that regulate gene transcription. Two modes of action exist: some nuclear receptors are bound to the DNA before the ligand is bound in a repressive capacity, and change their mode of action upon ligand binding. Others only bind to DNA upon ligand binding. About half of the NRs has been designated as orphan receptors, since no ligands have been identified for these receptors. In these receptors, the ligand binding pocket is either absent or constitutively occupied by a small lipid molecule or heme.

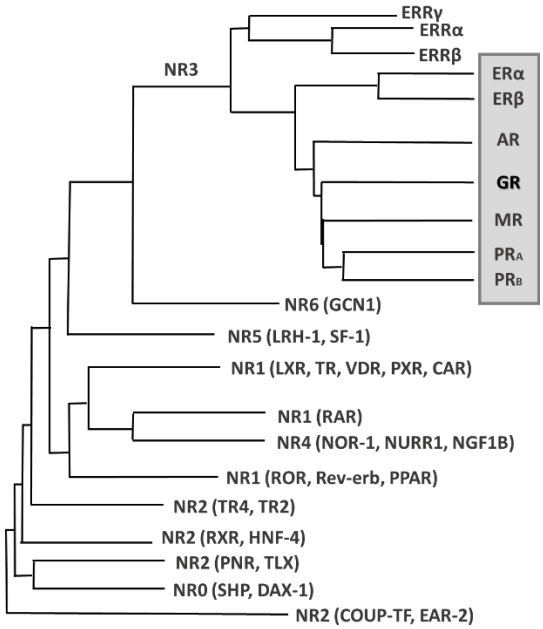

Figure 1. Nuclear receptor superfamily members. Steroid receptors (nuclear receptor subfamily 3; NR3) are boxed. Adapted from (7).

One class of nuclear receptors are the steroid receptors (figure 1). The ligands for these receptors are steroids, which are cholesterol-derived molecules that can easily traverse the plasma membrane. There are five classes of steroid hormones: androgens, estrogens, progestogens, mineralocorticoids and glucocorticoids. Secretion of these hormones by the endocrine organs in which they are produced (testis, ovary or adrenal gland) leads to circulation of these hormones in the bloodstream, so they can reach all cells in the body. Inside cells, these hormones are recognized by their respective receptors. This class contains the five steroid receptors: the androgen receptor (AR), estrogen receptor (ER), progesterone receptor (PR), mineralocorticoid receptor (MR) and glucocorticoid receptor (GR). Upon ligand binding, steroid receptors become activated, which enables them to bind specific target sites in the DNA, which are termed hormone response elements. These sites include repressive as well as activating sites. Subsequent recruitment of transcriptional coregulators can lead to either

transcription initiation or inhibition of associated genes. In addition to direct DNA-binding, steroid receptors can regulate gene expression through tethering to other transcription factors. These genomic effects of steroid receptors affect transcription and therefore the *de novo* synthesis of proteins, which are slow processes. Steroid receptors also perform more rapid non-genomic functions by playing on cytoplasmic signaling cascades, but much less is known about these latter pathways.

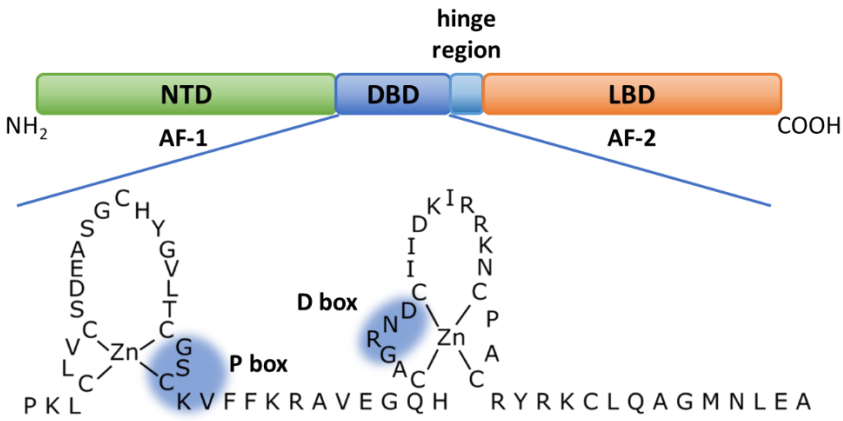

Figure 2. Modular structure of the GR. All steroid receptors share a common structure that includes an N-terminal-domain (NTD), a DNA-binding-domain (DBD) and a Ligand-binding-domain (LBD). Two transactivation domains (AF-1 & AF-2) allow for binding of coregulators to the GR. The amino acid sequence of the GR DBD is given. The DBD consists of two loops that are held together by Zinc residues. The proximal box (P box) contains the residues that are in direct contact with the DNA. The distal box (D box) contains residues that are involved in dimerization of the receptor.

All steroid receptors share a common structure encompassing three domains; an N-terminal domain (NTD), a DNA-binding-domain (DBD) and a ligand-binding-domain (LBD). In figure 2, the structure of the GR is given as an example. The N-terminal domain varies in length and is typically not well-conserved. It is thought to function as a docking site for transcriptional coregulators in the form of an activating function region (AF1) (8). The DBD is highly conserved and is involved in the recognition of specific DNA sequences. It contains two loops (so-called zinc fingers) that are shaped by

four cysteine residues that coordinate a zinc atom. The first loop contains the proximal box (P box), which includes residues that interact directly with the DNA. The second loop contains the distal box (D box) that is involved in dimerization of the receptor. The LBD is folded into multiple helices that together form the ligand binding pocket. Because different receptors bind slightly different ligands, the LBD is moderately conserved. The LBD also contains a transactivating domain (AF2) which interacts with different coregulators in a ligand-dependent way.

1.4 MEET THE MAIN ACTOR: THE GLUCOCORTICOID RECEPTOR (GR)

The main endogenous ligand of the glucocorticoid receptor in humans is cortisol. Cortisol is produced, in a diurnal rhythm and in response to stress, by the adrenal glands upon stimulation by ACTH from the pituitary, which in turn is under the control of the hypothalamic CRF secretion. Together these organs constitute the hypothalamic-pituitary (HPA) axis and are involved in maintaining homeostasis in a circadian and ultradian rhythm as well as controlling our response to stress. At the pituitary and the hypothalamus, cortisol functions as an inhibitor resulting in a negative feedback loop.

Cortisol affects a wide range of systems in our body. These effects are mediated by the GR and another steroid receptor, the MR. The MR has a higher binding affinity for cortisol and is activated under basal conditions, whereas the GR only becomes activated when cortisol levels are increased upon stress due to its lower affinity. The GR evokes different responses in different cell types. In general, it is tasked with maintaining metabolism and energy homeostasis. For example, during starvation or exercise the GR regulates gluconeogenesis and glycogenolysis in the liver. It is also involved in maintenance of blood pressure homeostasis through inhibition of vasodilators (9). Effects on brain function and behavior have been demonstrated as well. Elevated levels of cortisol have been associated with psychiatric disorders and studies indicate that functioning of the GR correlates with anxiety behavior (10). The GR has also been implicated in memory formation (11–13). Finally, the GR affects functioning of almost all cells of the immune system. In general activation of GR leads to suppression

of the immune system, although some stimulating effects have been observed as well (14).

The immunosuppressive effect of the cortisol is widely used clinically. Injections of cortisol were first used in 1940 by Philip Hench to treat patients with rheumathoid arthritis. Nowadays synthetic glucocorticoid drugs such as dexamethasone, prednisolone and fluticasone proprionate are commonly used in patients with immune-related diseases that include asthma, skin and ocular infections and patients undergoing organ transplants (14,15). Unfortunately, two major concerns impede the use of glucocorticoids in disease: serious side effects and glucocorticoid resistance. Up to one third of patients that receive chronic treatment with glucocorticoids show reduced glucocorticoid sensitivity (16). It is of note that not only exogenous supplementation of glucocorticoids, but also chronic stress leading to chronic glucocorticoid exposure is thought to lead to glucocorticoid resistance (16). Multiple mechanisms have been implicated in resistance, including an increase in the expression of the ß-isoform of the GR, changes in posttranslational modifications of the GR, reduced nuclear translocation of the GR, down-regulation of GR expression and repression by NF-κB (14,17). It has been suggested that the absence of the pulsatile changes that naturally occur under healthy conditions might also contribute. The side effects of glucocorticoid treatment include hyperglycemia, weight gain, osteoporosis, hypertension, depression, delayed wound healing, osteoporosis, reduced muscle regeneration and protein degradation (14,16). To reduce these side effects, selective GR agonists and modulators are being developed.

1.5 DNA BINDING UP CLOSE

In the absence of ligand, the GR is associated with heat shock proteins and immunophilins to form an inactive multiprotein complex. This conformation promotes high-affinity ligand binding, after which a conformational change most likely exposes as second nuclear localization signal of the GR, which facilitates active translocation of the GR to the nucleus, where it interacts with DNA. Several motifs have been associated with GR binding to DNA either directly or indirectly (figure 3). Classically, it can bind to specific target sites, so-called glucocorticoid-response elements (GREs). On these sites, the GR

homodimer binds to a half of the consensus sequence that is comprised of an inverted palindromic hexamer separated by three basepairs: AGAACAnnnTCTTGT. In the DBD of the GR, there are three amino acid residues that make base-specific contacts in the major groove of the DNA. Lysine 442 interacts directly with a thymine that is strongly conserved in the consensus GRE sequence. Valine 443 interacts with a guanine that is strongly conserved in all hormone response elements (18,19). The third residue to be involved in specific DNA binding is arginine 447. This residue has a direct interaction with a guanine that is present in canonical GREs. A stretch between the two zinc fingers of the DBD makes nonspecific contacts with the DNA helix backbone and the minor groove (18,20). Mutation of one of the residues involved in these interactions, arginine 477, leads to cortisol resistance in humans (21). The binding site as well as the sequence directly flanking the binding site influence the transcriptional effect of the GR, making the DNA an allosteric regulator of the GR (22–24). Recently it was shown that DNA binding can also trigger tetramerization of the GR, which might influence GR functioning (25).

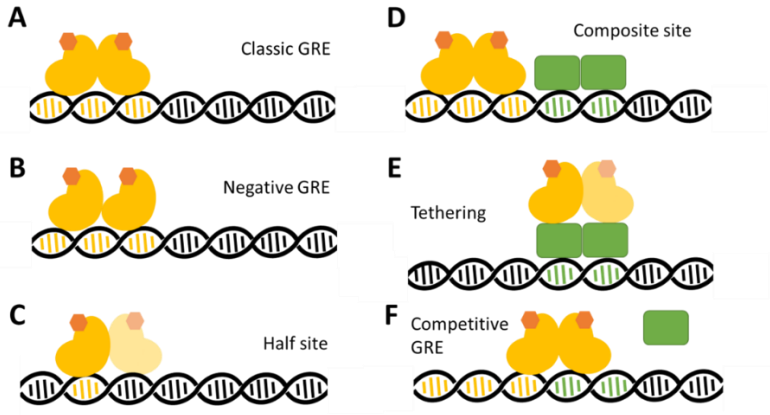

Figure 3. Types of GR binding in the nucleus. Four types of direct DNA binding and one type of indirect DNA binding have been identified. A. Binding of a homodimer to a GRE (yellow DNA). B. Binding of GR homodimer in a different conformation to negative GRE (nGRE). C. binding of GR to a GR half site (only one GR directly interacts with the DNA). D. Binding of GR that promotes interaction with another transcription factor. E. Indirect DNA binding through tethering to other transcription factors. F. Binding of GR to a GRE that prevents binding of transcription factors to neighboring DNA binding motifs.

Alternatively, the GR can bind to variations of the CTCC(n)$_{0-2}$GGAGA consensus sequence. A different GR dimer conformation has been correlated with these binding sites (26,27). These sequences were termed negative GREs because in general the activity of genes associated with them is downregulated by GR. In addition, it has been shown that the GR can bind to half sites as well as composite sites (14). A composite site is a functional unit of DNA with two or more different transcription factor binding sites. Through the interaction between the transcription factors gene expression is regulated (this can by synergistic or antagonistic). This term was originally coined for the composite site of a GR binding site that was found to be adjacent to an AP-1 binding site, which regulated the mouse proliferin promotor (28). Through binding of GR to other transcription factors (tethering), the GR has been shown to regulate their transcription. Tethering can occur through direct interactions between the transcription factors, but can also be mediated by a cofactor (29). Furthermore, the GR can bind to GREs and inhibit binding of transcription factors on a neighboring motif (30). Although recently it was suggested that the GR can also bind directly to other transcription factor motifs (31). Indeed, GR regulation of genes also involves many other transcription factors as was shown by analysis of gene regulatory networks (32). A number of genes is regulated by the GR without associated GR binding sites (32).

Between 6,000 to 50,000 target sequences may be bound by the GR, and this is highly context dependent (33–36). Of all GR binding sites only 4 to 11 percent overlaps between cell types (33). Moreover, genes associated with GR binding sites that overlap between cell types do not show the same magnitude of the response. Although the GR is able to recruit chromatin remodelers, 70-90% of GR binding sites is situated in pre-accessible chromatin (33). In line with these results, it was shown in an *in vitro* study that the GR has a higher affinity for DNA which is further away from a nucleosome and hence more accessible (24). Accessibility of DNA is regulated through epigenetic markers that locally compact or decompact chromatin and regulate nucleosome occupation. These variations in chromatin accessibility determine the cell type specificity of GR action. In addition, the cell type specific chromatin arrangement in the nucleus can bring binding

sites in enhancer regions and regulated genes together. It was shown that this arrangement is pre-established by other factors prior to binding of the essential transcription factor (37).

Further cell type specific regulation is conferred by posttranslational modifications brought about by different actors that are present in the cell (38). At least one posttranslational modification, phosphorylation, is dependent on the cell cycle, which suggests that there might be cell cycle dependent responses to glucocorticoids (39). Posttranslational modifications might affect the conformation and hence the function of the GR as different conformational changes lead to different coregulator binding patterns. Finally, although the GR is produced from one gene, different isoforms occur through alternative RNA splicing and variations in translation initiation. They have slightly different functions and abundancy, leading to fine tuning of GR signaling in a cell and tissue specific manner (40).

Gene expression is the result of a complex interplay between modification of GR through factors available in the cell, accessible DNA sequences and the ligand, which together induce conformational changes in the receptor, which enable different transcriptional coregulators to bind (figure 4). Once bound to DNA, the GR interacts with many different other proteins, the so-called transcriptional coregulators. The GR is known to recruit chromatin remodelers, e.g. the SWI/SNF complex, which moves or removes nucleosomes or replaces histone proteins in an ATP-dependent manner. This most likely further opens up the chromatin, resulting in increased DNA accessibility, as was suggested by FAIRE-seq experiments (41). Furthermore, histone methyl- and acetyltransferases, such as CARM1 and CBP/p300, interact with the GR to further make the chromatin accessible and mark the chromatin region by a specific pattern of acetylations and methylations on the tails of histone proteins (42). Interaction of the GR with mediating complexes, such as TRAP/DRIP, facilitate recruitment of the components of the basal transcription machinery like RNA polymerase II. Together, these factors enable the initiation of the transcription process. When different proteins, such as NcoR, are part of the complex, transcription can also be repressed.

Although the way the interactions are described here imply a successive buildup of factors that lead to transcription initiation, the process is not so linear. For example, recruitment of chromatin remodelers leads to dissociation of GR from DNA (43). In addition, p23 and the proteasome also play a role in the residence time of the GR on DNA (44). This residence time is relevant, because longer residence times are associated with greater transcriptional output (44). These results indicate that it is important to understand not only the interactions between factors, but also the dynamics of their interplay.

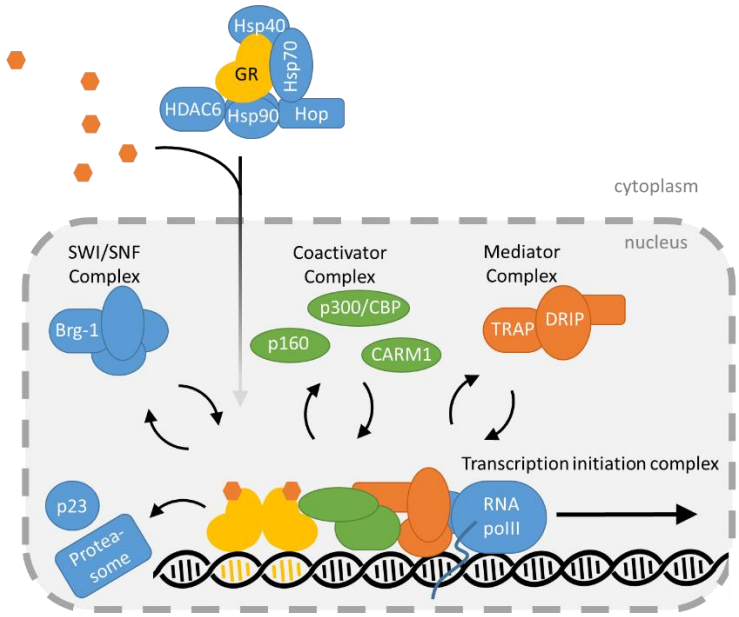

Figure 4. Coregulators of the GR. In the cytoplasm the GR is kept inactive through binding with heatshock proteins (Hsp), HDAC6 and Hop. Upon ligand binding the GR is shuttled to the nucleus and binds to DNA. At the DNA three main classes of coregulators interact with the GR in a dynamic manner, chromatin remodelers (SWI/SNF complex), coactivators (p160, p300, CRM1) and mediators (TRAP/DRIP). Subsequently, the transcription initiation complex is recruited, which includes RNA polymerase II (RNA polII). The proteasome and p23 play a role in the residence time of the GR on the DNA.

1.6 SEEING IS BELIEVING; CAPTURING THE INVISIBLE THROUGH MICROSCOPY

To understand the role of transcription factors in transcription regulation, we need to investigate both the distribution of molecules and their dynamics. In this thesis, advanced microscopy techniques are used to access this temporal and spatial information. In particular, single molecule microscopy and fluorescence recovery after photobleaching are employed.

In one of the earliest microscopes used for science in the late 17th century, Antoni van Leeuwenhoek used a single lens to magnify an object. Specimens were placed within the focal length of the lens and by placing the eye at a certain distance from the objective lens, a magnified image of the specimen would be projected in focus on the retina. This required a good eye and a lot of light. It took the advancement that Van Leeuwenhoek made in making the lenses to obtain the magnification important to life sciences. Even though larger magnifications were now possible, aberrations as a result of the different diffraction of different colors of light were limiting to the imaging of small objects. Compound microscopes, in which more than one lens were used to obtain a higher magnification, had already been discovered, but the aberrations limited the use of these microscopes.

Around 1850, the German instrument maker Carl Zeiss, joined by the chemist Otto Schott and the mathematician Ernst Abbe, made yet another improvement in microscopy. Otto Schott continued to optimize the glass formulation and optical properties of lenses, where Ernst Abbe aided the corrections for chromatic aberrations and developed a theoretical framework to understand the principles of microscopy. He created a formula that defines the resolution limit of a light microscope (equation 1), supporting it with experimental and theoretical work.

$$d = \frac{\lambda}{2\,N.A.} \qquad \text{Eq. 1}$$

with d the resolution and λ the wavelength of the light that is used. Abbe defined the numerical aperture (N.A.) of an objective lens as the sine of α (half the angle of the light cone that enters the objective), times the

refractive index of the medium between the objective and the cover glass. With this formula, we can calculate the resolution, which is defined as the smallest distance between two objects at which they can still be detected as individual objects. The highest quality objectives used in light microscopes today have an N.A. of 1.49, so for visible light (380-680 nm) the resolution *d* ranges between 128 and 2228 nanometer.

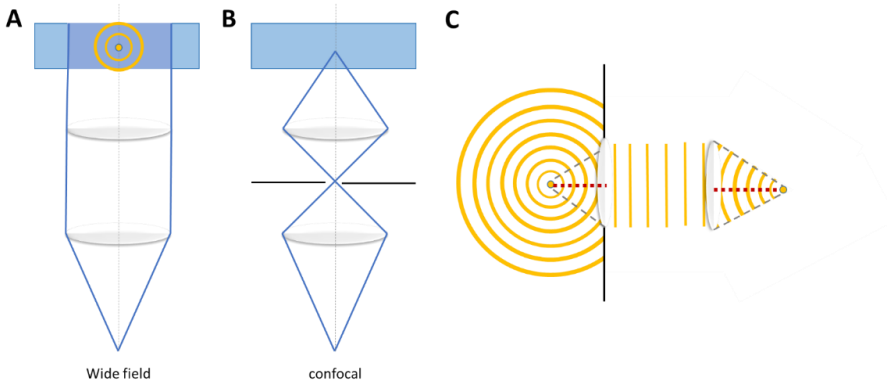

Figure 5. General principles of microscopy. A. Principle of wide field microscopy in which a large portion of the specimen (light blue bar) is illuminated (dark blue bar). The yellow point with concentric circles represents a single molecule that is illuminated. B. Principle of confocal microscopy. The captured light is restricted through a pinhole (black lines) and light from only a small volume of the sample is detected. C. A point source emits light in concentric circles. When a lens is placed at a distance that is equal to the focal length of the lens (red dashed lines), the wave propagates as a plane. When another lens is encountered, the image of the point source is in focus at the focal length of the lens. At this point, the image of the point source no longer looks like a point, but as an Airy disc (see text).

When the light source directly illuminates the whole sample, throughput its full width and depth, we speak of wide field microscopy (figure 5a). Although the whole depth of the sample is illuminated only a part of the sample is in focus, and other regions of the sample contribute to a high out-of-focus background signal. To reduce this noise, confocal microscopy was developed. By placing a pinhole in front of the detector, only the emitted light from a plane in the sample with a limited thickness reaches the detector, resulting in so-called optical sectioning (figure 5B). The pinhole also limits the portion

of the sample that is illuminated in the x,y-plane (figure 5B). To obtain a full image of the sample, the beam is scanned along the x,y plane of the image. To circumvent the time-consuming task of scanning, spinning disk microscopy was developed. In this microscope, through a series of thousand or more lenses combined with pinholes the sample is illuminated simultaneously. In this thesis both wide field microscopy as well as spinning disk microscopy have been used.

Light originating from a point source that is at the focal length from the objective lens, propagates as a spherical wave around the point source (figure 5C). The spherical wave is translated into a plane wave by the objective lens. Another lens, the imaging lens, can then convert the plane wave back to a spherical wave, which will focus into a point at the focal length of the imaging lens. If a camera is placed at the focal length of the imaging lens, we can capture an image of our object. However, when light passes through an object with a finite aperture, such as a lens, diffraction occurs. The resulting diffraction pattern due to interference of the diffracted waves causes the image that is obtained to be a series of concentric rings with decreasing intensities rather than a single point. This particular pattern is called an Airy disc. The diameter of this pattern is directly related to the wavelength and the size of the aperture. When two point emitters are close, their diffraction patterns overlap and the interference makes it impossible to distinguish the two objects. This caused Lord Rayleigh to adjust the resolution limit described by Abbe to be based on the smallest distance between two Airy discs where they can still be resolved separately (equation 2).

$$d = \frac{1.22\lambda}{2\ N.A.} \qquad \text{Eq. 2}$$

When the object is smaller than the diffraction limit, it appears larger through the interference pattern that is created. The point spread function is the description of the 3D image that the point object creates on the camera. As a general approximation, we can use a 2D-Gaussian to fit the central peak of the Airy disc and determine the center of the Gaussian with large accuracy (figure 6). This method is termed single molecule microscopy

and is used to observe single molecules in live cells. In this manner, the position of a molecule can be determined with precision of up to 30 nanometer, which is well beyond the resolution limit described by Abbe and Rayleigh. Through the use of modern high-speed cameras, their mobility can be captured with a time resolution of 5 milliseconds. Initially, experiments in live cells were focused on proteins inside membranes (45–48). In more recent years, the diffusion of proteins in 3D volumes, such as the nucleus, has also been explored. The first transcription factor study reported to use single molecule microscopy was the lac repressor in *Escherichia Coli* in 2007 (49). Soon after, many other transcription factors followed. In particular, the GR and other family members have been well characterized.

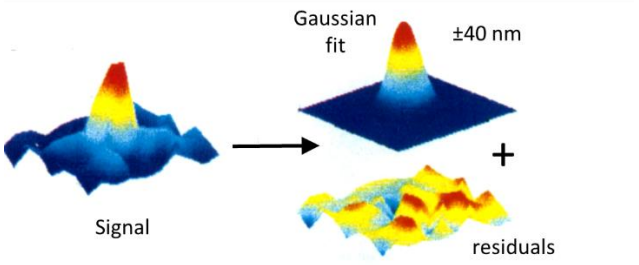

Figure 6. Single molecule identification. The signal obtained from the projection of a single molecule on the camera is fitted with a 2D Gaussian with an accuracy of ± 40 nm. The residuals compare to the background noise. Adapted from Schmidt et al. 1995 (50).

1.7 Making proteins visible for microscopy

To observe proteins such as the GR using conventional microscopy the proteins are often conjugated to a fluorescent protein or tagged with a fluorescent dye. The principle of fluorescence relies on the excitation of an electron of the fluorescent molecule from the ground state to an excited state upon absorption of a photon. After a rapid relaxation to the lowest vibrational energy state, the electron falls back to the ground state and light is emitted. The emitted photon has a lower energy than the photon that excited the electron due to the first rapid relaxation (figure 7). Hence, the emission light has a longer wavelength than the excitation light and can be separated allowing for the detection of only the emitted photons.

Occasionally, the electron does not fall back to the ground state immediately, but is retained in a dark state. Once the photon decays to the ground state, it can be excited again. The detection of alternatively, direct decay to the ground state and retention in the dark state, is recorded on the camera as blinking behavior. Simultaneous absorption of two photons, with both photons carrying half the energy, can also result in excitation of the electron to the same excited state as mentioned before. This can be advantageous as the difference between the photons used to excite the electron and the photon emitted is larger, which results in lower background. Moreover, two photon excitation results in confocal excitation, and the lower energy photons incur less damage in live cells.

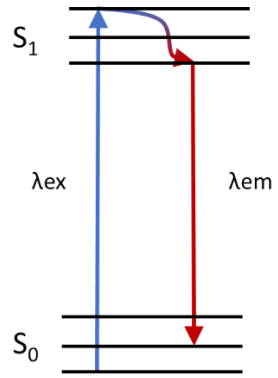

Figure 7. Jabloinski diagram of an electron. Excitation of an electron from the ground state (S_0) to the excited state (S_1) occurs due to absorbance of a photon. The first step consists of thermal decay. In the second step, the electron is returned to the ground state and a photon is emitted.

Photobleaching is the photochemical alteration of a molecule after excitation such that it can no longer be excited, and this process can be exploited to study the dynamics of proteins such as the GR in live cells. By sending a large number of photons to a well-defined area within the cell, the fluorescent molecules in that area are bleached, rendering these molecules invisible. By observing, over time, the dissipation of the bleached molecules to other areas in the cell as well as the movement of fluorescent molecules into the

bleached area we can infer the mobility pattern of the fluorescent molecules. This method is named fluorescent recovery after photobleaching (FRAP).

Because photobleaching and blinking of fluorescent proteins remains an issue in studying the diffusion of proteins over long time scales, efforts are being made in the search for alternative labels for the visualization of proteins inside living cells. Noble metals offer such an opportunity. In particular gold nanoparticles, spherical or rod-shaped have been used in live cells. Upon bombarding particles made of these materials with photons, rather than excitation and decay of a single electron, a collective oscillation of the free electrons on the surface of the particle is generated in a process termed plasmon resonance. Upon recombination of an electron with a hole in the lattice a photon is emitted that can be detected. For this type of interaction the optimal excitation wavelength is dependent on the ratio between the longitudinal and transverse axis of the particle. Interestingly, gold nanorods lend themselves well for anti-Stokes imaging. When after excitation (but before decay) additional energy is absorbed by the particle, for example through heat, there is a possibility that the emitted photon of a higher energy than the excitation wavelength, so light is emitted that has a shorter wavelength than the excitation light. As this process is rare for cellular structures, exclusive detection of photons that are produced via this anti-Stokes process results in near background-free imaging of gold nanorods in living cells (51).

1.8 FROM IMAGES TO NUMBERS; QUANTIFICATION.

Quantification of data obtained using microscopic imaging of biological samples is perhaps as difficult as getting the images in the first place, and therefore methods to analyze data are continually in development. In this thesis, in particular single molecule and FRAP experiments are quantitatively analyzed in detail.

Quantification of FRAP experiments by directly fitting the data is complicated by the large number of variables that need to be taken into account. This can be circumvented by using an approach in which the experimental data is compared to curves generated using Monte Carlo modeling. In this method,

simulations are made of diffusing molecules that can bind in an ellipsoid volume. A large set of curves is generated by varying the parameters that are involved within physiologically relevant ranges. The curves that best fit the experimentally obtained curves are then selected. The parameters used to construct these curves most likely reflect the true binding times of the transcription factors. Hence, this method for the quantification of FRAP experiments allows for the understanding of transcription factors in a quantitative manner.

To analyze single molecule experiments, different methods are required. As mentioned earlier we can determine the position of a single fluorescent protein with an accuracy of ~30 nm when we fit the distribution of light derived from a single molecule with a 2D-Gaussian. However, if we want to track the movement of this molecule over time we are limited by the bleaching and blinking properties of the fluorescent molecule. Since this results in short trajectories for individual molecules, most often the results of many molecules are pooled to obtain reliable data on their mobility. Furthermore, proper tracking of molecules requires some *a priori* knowledge on their mobility. In order to be able to use an unbiased approach, the Particle Image Correlation Spectroscopy (PICS) method was developed. By determining all possible correlations between the location of molecules in consecutive images, a cumulative distribution function (Cdf) of displacements *R* is generated (for details see chapter 2, 3 and (52)). From the cumulative distribution function we can determine, by curve fitting, whether there are multiple fractions with different mobility, the sizes of these fractions α and their respective diffusion coefficients *D*. Equation 3 can be used for curve fitting when three fractions of molecules occur.

$$Cdf(R^2) = 1 - \left(\alpha_1 \exp\left(\frac{R^2}{4D_1 t + 4\sigma^2}\right) - \alpha_2 \exp\left(\frac{R^2}{4D_2 t + 4\sigma^2}\right) - \alpha_3 \exp\left(\frac{R^2}{4\sigma^2}\right)\right)$$

Eq. 3

Using different intervals between images several cumulative distributions can be obtained for the same data. However, it is notable that as the interval increases a bias is created towards slower diffusing particles in settings where the depth of focus is limiting. Because particles that move slower

remain in the observable volume for a longer time than particles that diffuse faster, the α-coefficient is distorted. In chapter 3 of this thesis an analytical solution for is provided.

We can use the Cdf, obtained from the single-molecule data to extract additional dynamic parameters and time scales. Under the framework of a continuous-time Markov chain model, we can obtain the occupation probability distribution (for further explanation see (53). This allows us to get an insight into the probability of the GR to switch between binding and diffusion states as well as the time spent in these states.

1.9 AND ACTION! DYNAMICS OF TRANSCRIPTION FACTORS

In this thesis, advanced microscopy studies on the dynamics and distribution of the GR in living cells are described. Early *in vitro* studies showed slow kinetics of transcription factors. Residence times on the DNA were found to be in the order of minutes to hours, which is in correspondence with the pace of transcription initiation. This static model was contradicted by a study in live cells (54). This study showed that after photobleaching of a small area of the nucleus containing an array of GREs, the recovery of fluorescently labeled GRs to this site and dissipation of photobleached GRs was in the order of seconds (54). A hit-and-run model was proposed, where the GR is only present at the GRE for a short period of time. These immobilizations of the receptor were associated with transcriptional activation (44). This dynamic behavior was confirmed by later studies and, amongst others, it was shown to be dependent on the type of ligand (55). There are indications that the contrast between *in vitro* and live cells experiments portrays an active disassembly of transcription factors from the chromatin in live cells (44,56).

In addition to its DNA binding, the diffusion of the GR in the nucleus has been studied extensively. Diffusion of transcription factors is necessary to find their binding sites as well as move between binding sites. Diffusion of the GR has been found to range around 3 $\mu m^2/s$ (57–60), which is comparable to other transcription factors (49,61–63). It has been proposed that effective search mechanisms are comprised of 3D as well as 1D diffusion (64,65), although 1D diffusion has only been demonstrated *in vitro* and in bacteria

(66–68). Different types of retarded diffusion have been proposed, such as 1D sliding along the DNA, hopping and intersegmental exchange (figure 8). Together, these studies have demonstrated the occurrence of multiple dynamic states for transcription factors like the GR. However, the temporal relations between these states is poorly understood because information on state-to-state transitions is not available. Furthermore, a consistent view describing all states including the biological processes underlying them is still lacking.

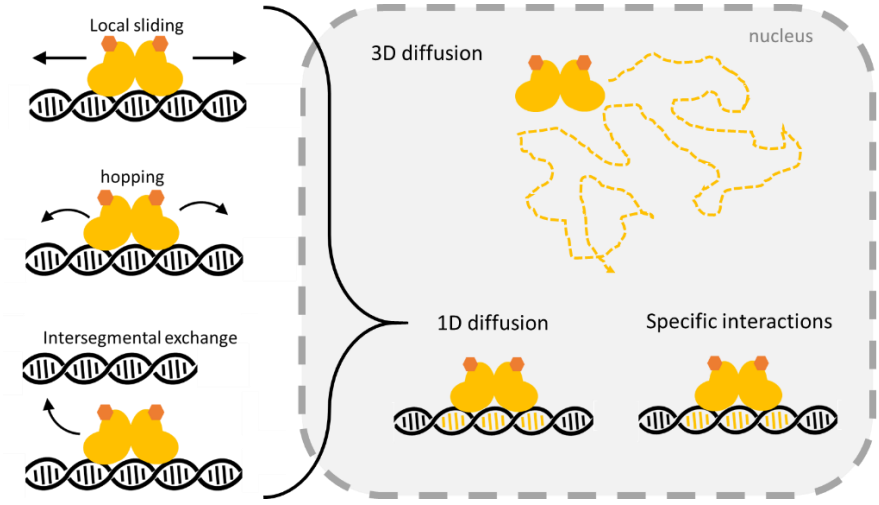

Figure 8. GR dynamics in the nucleus. Modes of 3D diffusion, 1D diffusion and specific binding have been identified. 1D diffusion might be based on non-specific interactions and can include local sliding, hopping and intersegmental exchange.

To salvage the apparent contradiction between the slow process of transcription with the fast binding kinetics of transcription factors, a probabilistic model has been suggested, which is based on stochastic interactions between transcription factors and DNA. In addition, most current models assume thermodynamic equilibrium. Although this makes modeling easier and provides meaningful results, there are certain underlying assumptions that may not always hold true. These include a balance of each reaction such that it takes place equally in both directions. These new directions highlight the need for a quantitative model of

transcription binding that dissects the behavior of individual transcription factors from that of the average population effect.

AIMS

The central aim of this thesis is quantification of the dynamics and distribution of the GR, a model transcription factor, in live cells. We have divided the work in the following objectives:

1. Generate the most complete description of GR dynamics to date
   a. Identification mobile and immobile states of GR using a combination of single molecule measurements and FRAP experiments
   b. Characterizing switching behavior of the GR between states
   c. Analyzing the biological mechanism underlying each states through the use of a series of six DNA-binding mutants
2. Development of novel analysis methods to better quantify GR diffusion
3. Characterize the distribution of GR in the nucleus of live cells
   a. Comparison of this distribution with ER, a closely related nuclear receptor
   b. Analyzing the biological mechanisms underlying GR distribution through the use of GR and ER mutants
4. Development of a novel method to track GR dynamics through the nucleus for arbitrarily long times

1.10 Outline of this thesis

In this thesis, we have developed a framework to understand how the GR is spatially and temporally distributed in the nucleus of live cells, in order to better understand how it regulates transcription. Concomitantly, we have developed several experimental strategies to study these phenomena.

In **chapter 2** the GR is used to show novel mechanisms for DNA target site finding and binding by transcription factors. To this end a combination of single molecule microscopy and FRAP is used and a range of DNA-binding mutants is studied.

In **chapter 3** the analysis of single molecule data is extended to provide a solution for depth of focus loss of diffusive molecules. To this end the probability of losing molecules due to diffusion out of the depth of focus is taken into account in the analysis.

In **chapter 4** the spatial distribution of the GR and ER in the nucleus of live cells is analyzed. It is shown that the number of receptor hotspots and their size in the nucleus is dependent on the type of receptor. However, this is independent of the specific DNA binding properties of the receptor.

In **chapter 5** the potential of gold nanorods as a label for diffusive proteins is investigated. The diffusive behavior of gold nanorods is studied in two cellular compartments, the cytoplasm and nucleus. In addition, gold nanorods are functionalized with a nuclear localization signal resulting in successful translocation of these particles to the nucleus.

REFERENCES

1. Huo S, Jin S, Ma X, Xue X, Yang K, Kumar A, et al. Ultrasmall gold nanoparticles as carriers for nucleus-based gene therapy due to size-dependent nuclear entry. ACS Nano. 2014;8(6):5852–62.

2. Pante N, Kann M. Nuclear Pore Complex Is Able to Transport Macromolecules with Diameters of 39 nm. Mol Biol Cell. 2002;13(2):425–34.

3. Nativo P, Prior IA, Brust M. Uptake and intracellular fate of surface-modified gold nanoparticles. ACS Nano. 2008;2(8):1639–44.

4. Oyelere AK, Chen PC, Huang X, El-Sayed IH, El-Sayed MA. Peptide-conjugated gold nanorods for nuclear targeting. Bioconjug Chem. 2007;18(5):1490–7.

5. Phillips R, Kondev J, Theriot J, Garcia H, Chasan B. Physical Biology of the Cell. Vol. 78, American Journal of Physics. 2010. 1230 p.

6. Gillooly JF, Hein A, Damiani R. Nuclear DNA content varies with cell size across human cell types. Cold Spring Harb Perspect Biol. 2015;7(7):1–27.

7. Laudet V, Hänni C, Coll J, Catzeflis F, Stéhelin D. Evolution of the nuclear receptor gene superfamily. EMBO J. 1992;

8. Zanchi NE, De Siqueira Filho MA, Felitti V, Nicastro H, Lorenzeti FM, Lancha AH. Glucocorticoids: Extensive physiological actions modulated through multiple mechanisms of gene regulation. Vol. 224, Journal of Cellular Physiology. 2010. p. 311–5.

9. Lee SR, Kim HK, Youm JB, Dizon LA, Song IS, Jeong SH, et al. Non-genomic effect of glucocorticoids on cardiovascular system. Vol. 464, Pflügers Archiv : European journal of physiology. 2012. p. 549–59.

10. Ziv L, Muto A, Schoonheim PJ, Meijsing SH, Strasser D, Ingraham HA, et al. An affective disorder in zebrafish with mutation of the glucocorticoid receptor. Mol Psychiatry. 2013;18(6):681–91.

11. Kolber BJ, Roberts MS, Howell MP, Wozniak DF, Sands MS, Muglia LJ. Central amygdala glucocorticoid receptor action promotes fear-associated CRH activation and conditioning. Proc Natl Acad Sci. 2008;105(33):12004–9.

12. Arnett MG, Kolber BJ, Boyle MP, Muglia LJ. Behavioral insights from mouse models of forebrain- and amygdala-specific glucocorticoid receptor genetic disruption. Vol. 336, Molecular and Cellular Endocrinology. 2011. p. 2–5.

13. Atsak P, Guenzel FM, Kantar-Gok D, Zalachoras I, Yargicoglu P, Meijer OC, et al. Glucocorticoids mediate stress-induced impairment of retrieval of stimulus-response memory. Psychoneuroendocrinology. 2016;67:207–15.

14. Kadmiel M, Cidlowski JA. Glucocorticoid receptor signaling in health and disease. Vol. 34, Trends in Pharmacological Sciences. 2013. p. 518–30.

15. Kino T, Charmandari E, Chrousos GP. Glucocorticoid receptor: Implications for rheumatic diseases. Clin Exp Rheumatol. 2011;29(5 SUPPL. 68).

16. Biddie SC, Conway-campbell BL, Lightman SL. Dynamic regulation of glucocorticoid signalling in health and disease. Vol. 51, Rheumatology. 2012. p. 403–12.

17. Schaaf MJM, Cidlowski JA. Molecular mechanisms of glucocorticoid action and resistance. J Steroid Biochem Mol Biol. 2002;83(1–5):37–48.

18. Luisi BF, Xu WX, Otwinowski Z, Freedman LP, Yamamoto KR, Sigler PB. Crystallographic analysis of the interaction of the glucocorticoid receptor with DNA. Nature. 1991;352(6335):497–505.

19. Nordeen SK, Suh BJ, Kühnel B, Hutchison IIICA. Structural Determinants of a Glucocorticoid Receptor Recognition Element. Mol Endocrinol. 1990;4(12):1866–73.

20. Kumar R, Thompson EB. The structure of the nuclear hormone receptors. Steroids. 1999;64(5):310–9.

21. Ruiz M, Lind U, Gåfvels M, Eggertsen G, Carlstedt-Duke J, Nilsson L, et al. Characterization of two novel mutations in the glucocorticoid receptor gene in patients with primary cortisol resistance. Clin Endocrinol (Oxf). 2001;55(3):363–71.

22. Meijsing SH, Pufall MA, So AY, Bates DL, Chen L, Yamamoto KR. DNA Binding Site Sequence Directs Glucocorticoid Receptor Structure and Activity. Science. 2009;324(5925):407–10.

23. Watson LC, Kuchenbecker KM, Schiller BJ, Gross JD, Pufall MA, Yamamoto KR. The glucocorticoid receptor dimer interface allosterically transmits sequence-specific DNA signals. Nat Struct Mol Biol. 2013;20(7):876–83.

24. Li Q, Wrange O. Translational positioning of a nucleosomal glucocorticoid response element modulates glucocorticoid receptor affinity. Genes Dev. 1993;7(12 A):2471–82.

25. Presman DM, Ganguly S, Schiltz RL, Johnson TA, Karpova TS, Hager GL. DNA binding triggers tetramerization of the glucocorticoid receptor in live cells. Proc Natl Acad Sci U S A. 2016;113(29):8236–41.

26. Hudson WH, Youn C, Ortlund EA. The structural basis of direct glucocorticoid-mediated transrepression. Nat Struct Mol Biol. 2013;20(1):53–8.

27. Surjit M, Ganti KP, Mukherji A, Ye T, Hua G, Metzger D, et al. Widespread negative response elements mediate direct repression by agonist-liganded glucocorticoid receptor. Cell. 2011;145(2):224–41.

28. Diamond MI, Miner JN, Yoshinaga SK, Yamamoto KR. Transcription factor interactions: selectors of positive or negative regulation from a single DNA element. Science (80-). 1990;249(4974):1266–72.

29. Beck IME, Berghe W Vanden, Vermeulen L, Yamamoto KR, Haegeman G, De Bosscher K. Crosstalk in inflammation: The interplay of glucocorticoid receptor-based mechanisms and

kinases and phosphatases. Endocrine Reviews. 2009.

30. Ratman D, Vanden Berghe W, Dejager L, Libert C, Tavernier J, Beck IM, et al. How glucocorticoid receptors modulate the activity of other transcription factors: A scope beyond tethering. Mol Cell Endocrinol. 2013;380(1–2):41–54.

31. Weikum ER, de Vera IMS, Nwachukwu JC, Hudson WH, Nettles KW, Kojetin DJ, et al. Tethering not required: the glucocorticoid receptor binds directly to activator protein-1 recognition motifs to repress inflammatory genes. Nucleic Acids Res. 2017;45(14):8596–608.

32. Le PP, Friedman JR, Schug J, Brestelli JE, Parker JB, Bochkis IM, et al. Glucocorticoid receptor-dependent gene regulatory networks. PLoS Genet. 2005;1(2):0159–70.

33. John S, Sabo PJ, Thurman RE, Sung MH, Biddie SC, Johnson TA, et al. Chromatin accessibility pre-determines glucocorticoid receptor binding patterns. Vol. 43, Nature Genetics. 2011. p. 264–8.

34. John S, Sabo PJ, Johnson TA, Sung MH, Biddie SC, Lightman SL, et al. Interaction of the Glucocorticoid Receptor with the Chromatin Landscape. Mol Cell. 2008;29(5):611–24.

35. So AYL, Chaivorapol C, Bolton EC, Li H, Yamamoto KR. Determinants of cell- and gene-specific transcriptional regulation by the glucocorticoid receptor. PLoS Genet. 2007;3(6):0927–38.

36. Steger DJ, Grant GR, Schupp M, Tomaru T, Lefterova MI, Schug J, et al. Propagation of adipogenic signals through an epigenomic transition state. Genes Dev. 2010;24(10):1035–44.

37. Hakim O, Sung MH, Voss TC, Splinter E, John S, Sabo PJ, et al. Diverse gene reprogramming events occur in the same spatial clusters of distal regulatory elements. Genome Res. 2011;

38. Weikum ER, Knuesel MT, Ortlund EA, Yamamoto KR. Glucocorticoid receptor control of transcription: Precision and plasticity via allostery. Vol. 18, Nature Reviews Molecular Cell Biology. 2017. p. 159–74.

39. Matthews L, Johnson J, Berry A, Trebble P, Cookson A, Spiller D, et al. Cell Cycle Phase Regulates Glucocorticoid Receptor Function. Cell Cycle Phase Regul Glucocorticoid Recept Funct PLoS ONE. 2011;6(7).

40. Lu NZ, Cidlowski JA. Glucocorticoid receptor isoforms generate transcription specificity. Vol. 16, Trends in Cell Biology. 2006. p. 301–7.

41. Burd CJ, Ward JM, Crusselle-Davis VJ, Kissling GE, Phadke D, Shah RR, et al. Analysis of chromatin dynamics during glucocorticoid receptor activation. Mol Cell Biol. 2012;32(10):1805–17.

42. Petta I, Dejager L, Ballegeer M, Lievens S, Tavernier J, De Bosscher K, et al. The Interactome of the Glucocorticoid Receptor and Its Influence on the Actions of Glucocorticoids in Combatting Inflammatory and Infectious Diseases. Microbiol Mol Biol Rev. 2016;80(2):495–522.

43. Fletcher TM, Xiao N, Mautino G, Baumann CT, Wolford R, Warren BS, et al. ATP-dependent mobilization of the glucocorticoid receptor during chromatin remodeling. Mol Cell Biol. 2002;22(10):3255–63.

44. Stavreva DA, Muller WG, Hager GL, Smith CL, McNally JG. Rapid glucocorticoid receptor exchange at a promoter is coupled to transcription and regulated by chaperones and proteasomes. Mol Cell Biol. 2004;24(7):2682–97.

45. de Keijzer S, Serge A, van Hemert F, Lommerse PHM, Lamers GEM, Spaink HP, et al. A spatially restricted increase in receptor mobility is involved in directional sensing during Dictyostelium discoideum chemotaxis. J Cell Sci. 2008;

46. Iino R, Koyama I, Kusumi A. Single molecule imaging of green fluorescent proteins in living cells: E-cadherin forms oligomers on the free cell surface. Biophys J. 2001;

47. Harms GS, Cognet L, Lommerse PH, Blab GA, Schmidt T. Autofluorescent proteins in single-molecule research: applications to live cell imaging microscopy. Biophys J. 2001;80(5):2396–408.

48. Lommerse PHM, Blab GA, Cognet L, Harms GS, Snaar-Jagalska BE, Spaink HP, et al. Single-Molecule Imaging of the H-Ras Membrane-Anchor Reveals Domains in the Cytoplasmic Leaflet of the Cell Membrane. Biophys J. 2004;

49. Elf J, Li GW, Xie XS. Probing transcription factor dynamics at the single-molecule level in a living cell. Science (80-). 2007;316(5828):1191–4.

50. Schmidt T, Schütz GJ, Baumgartner W, Gruber HJ, Schindler H. Imaging of single molecule diffusion. Proc Natl Acad Sci U S A. 1996;93(7):2926–9.

51. Carattino A, Keizer VIP, Schaaf MJM, Orrit M. Background Suppression in Imaging Gold Nanorods through Detection of Anti-Stokes Emission. Biophys J. Biophysical Society; 2016;111(11):2492–9.

52. Semrau S, Schmidt T. Particle image correlation spectroscopy (PICS): retrieving nanometer-scale correlations from high-density single-molecule position data. Biophys J. 2007;92(2):613–21.

53. Coppola S, Caracciolo G, Schmidt T. Exact occupation probabilities for intermittent transport and application to image correlation spectroscopy. New J Phys. 2014;16(11):113057.

54. McNally JG, Muller WG, Walker D, Wolford R, Hager GL. The glucocorticoid receptor: rapid exchange with regulatory sites in living cells. Science (80-). 2000;287(5456):1262–5.

55. Schaaf MJ, Lewis-Tuffin LJ, Cidlowski JA. Ligand-selective targeting of the glucocorticoid receptor to nuclear subdomains is associated with decreased receptor mobility. Mol Endocrinol. 2005;19(6):1501–15.

56. Meijsing SH, Elbi C, Luecke HF, Hager GL, Yamamoto KR. The Ligand Binding Domain Controls Glucocorticoid Receptor Dynamics Independent of Ligand Release. Mol Cell Biol. 2007;27(7):2442–51.

57. Groeneweg FL, van Royen ME, Fenz S, Keizer VIP, Geverts B, Prins J, et al. Quantitation of glucocorticoid receptor DNA-binding dynamics by single-molecule microscopy and FRAP. PLoS One. 2014;9(3):e90532.

58. Gebhardt JC, Suter DM, Roy R, Zhao ZW, Chapman AR, Basu S, et al. Single-molecule imaging of transcription factor binding to DNA in live mammalian cells. Nat Methods. 2013;10(5):421–6.

59. Morisaki T, Muller WG, Golob N, Mazza D, McNally JG. Single-molecule analysis of transcription factor binding at transcription sites in live cells. Nat Commun. 2014;5:4456.

60. Paakinaho V, Presman DM, Ball DA, Johnson TA, Schiltz RL, Levitt P, et al. Single-molecule analysis of steroid receptor and cofactor action in living cells. Nat Commun. 2017;8:15896.

61. Mazza D, Abernathy A, Golob N, Morisaki T, McNally JG. A benchmark for chromatin binding measurements in live cells. Nucleic Acids Res. 2012;40(15):e119.

62. Speil J, Baumgart E, Siebrasse JP, Veith R, Vinkemeier U, Kubitscheck U. Activated STAT1 transcription factors conduct distinct saltatory movements in the cell nucleus. Biophys J. 2011;101(11):2592–600.

63. Van Royen ME, van Cappellen WA, Geverts B, Schmidt T, Houtsmuller AB, Schaaf MJ. Androgen receptor complexes probe DNA for recognition sequences by short random interactions. J Cell Sci. 2014;127(Pt 7):1406–16.

64. Normanno D, Dahan M, Darzacq X. Intra-nuclear mobility and target search mechanisms of transcription factors: A single-molecule perspective on gene expression. Biochim Biophys Acta - Gene Regul Mech. 2012;1819(6):482–93.

65. Normanno D, Boudarène L, Dugast-Darzacq C, Chen J, Richter C, Proux F, et al. Probing the target search of DNA-binding proteins in mammalian cells using TetR as model searcher. Nat Commun. 2015;6.

66. Hammar P, Leroy P, Mahmutovic A, Marklund EG, Berg OG, Elf J. The lac Repressor Displays Facilitated Diffusion in Living Cells. Science (80-). American Association for the Advancement of Science; 2012;336(6088):1595–8.

67. Xiong K, Blainey PC. Molecular sled sequences are common in mammalian proteins. Nucleic Acids Res. 2016;44(5):2266–73.

68. Xiong K, Erwin GS, Ansari AZ, Blainey PC. Sliding on DNA: From Peptides to Small Molecules. Angew Chemie - Int Ed. 2016;55(48):15110–4.

2 REPETITIVE SWITCHING BETWEEN DNA BINDING MODES ENABLES TARGET FINDING BY THE GLUCOCORTICOID RECEPTOR

Veer I.P. Keizer, Stefano Coppola, Adriaan B. Houtsmuller, Bart Geverts, Martin E. van Royen, Thomas Schmidt, Marcel J.M. Schaaf

ABSTRACT

Transcription factor mobility is a determining factor in the regulation of gene expression. Here, we have studied the intranuclear dynamics of the glucocorticoid receptor (GR) using fluorescence recovery after photobleaching and single-molecule microscopy. First we have described the dynamic states in which the GR occurs. Subsequently we have analyzed the transitions between these states using a continuous time Markov chain model, and functionally investigated these states by making specific mutations in the DNA-binding domain. This analysis revealed that the GR diffuses freely through the nucleus, and once it leaves this free diffusion state it most often enters a repetitive switching mode. In this mode it alternates between slow diffusion as a result of brief nonspecific DNA binding events, and a state of stable binding to specific DNA target sites. This repetitive switching mechanism results in a compact searching strategy that facilitates finding DNA target sites by the GR.

Journal of Cell Science (under revision)

2.1 INTRODUCTION

Transcription factors regulate gene expression by binding to specific DNA sequences and recruiting other proteins. A well-studied transcription factor is the glucocorticoid receptor (GR), a member of the steroid receptor family, which is activated by glucocorticoid ligands. Upon ligand binding the receptor translocates to the nucleus where it interacts with DNA to initiate or repress transcription. Using biochemical assays, a wealth of knowledge has been obtained on the action of the GR at its DNA binding sites. These DNA binding sites, termed glucocorticoid response elements (GREs), are palindromic sequences typically consisting of two hexamers with a three base pairs spacer (1–3). The GR can also bind to other sequences including negative GREs albeit in a different conformation (4,5). Additionally, the GR can regulate gene expression by influencing the function of other transcription factors, either by binding to composite GREs or through a process called tethering (6).

The development of live cell microscopy techniques using fluorescently tagged proteins enabled studies of the dynamic behavior of GR in the nucleus. The first investigations into the dynamics of the GR involved analysis by fluorescence recovery after photobleaching (FRAP), and in more recent years single-molecule microscopy (SMM) was used to further study the intranuclear dynamics of the GR. These studies revealed binding times in the order of seconds to the GRE (7–10). These transient immobilizations were found to be dependent on ligand activation and DNA binding of the GR and are associated with transcriptional activity (8,9,11,12). More recent studies also revealed immobilizations at the sub-seconds scale (12–14). Similar dynamic behavior was uncovered for other steroid receptors (15–19), as well as other transcription factors (20,21). In addition to these immobilizations, diffusive behavior through the nucleus was observed for the GR (12,13,22,23), and other bacterial and mammalian transcription factors, such as the lac repressor (24), STAT1 (25), p53 (12,26), and the androgen receptor (14). For the GR, STAT-1 and p53, two diffusion states with distinct diffusion coefficients were found (22,25,26).

Together, these studies have demonstrated the occurrence of multiple dynamic states for transcription factors like the GR. However, the temporal relations between these states is poorly understood because information on state-to-state transitions is not available. Furthermore, a consistent view describing all states including the biological processes underlying them is still lacking. In the present study, we have combined FRAP and SMM experiments, which enabled a coherent analysis of GR dynamics over a time scale ranging from milliseconds to seconds. We describe four dynamic states of the GR in detail. In addition, we have developed a continuous time Markov chain model that provided information about the transitions between states of the GR as well as the time spent in each state. Finally, we have employed a series of mutations that influences the DNA-binding capacity to assess the biological processes underlying these states. Our results demonstrate that the GR spends most of its time in a repetitive switching mode, alternating between slow diffusion and immobile states. These periods of repetitive switching are interrupted by periods of fast diffusion. These data provide a comprehensive description of the mechanism by which the GR finds its target sites.

2.2 RESULTS

In all experiments described here, a well-characterized experimental system was used in which a YFP-GR fusion protein, comprising the human GR fused N-terminally to an enhanced yellow fluorescent protein (EYFP), was expressed in COS-1 cells (Figure 1A) (8,9,13). In these studies it was demonstrated that the receptor mobility was dependent on the ligand, and in the present study the high affinity synthetic glucocorticoid fluticasone propionate (FP) was used which induces a maximal effect on the mobility of GR.

First, to study the mobility pattern of the GR in the nucleus of live cells, FRAP experiments were performed. In these measurements, photobleaching of YFP-GRs was performed by application of maximal laser power to a small strip spanning the nucleus. Subsequently, the recovery of the fluorescent signal was quantified over time (Figure 1B) (27). The experimental recovery curves were quantitatively analyzed using Monte Carlo simulations. Three

states were detected: a diffusion state in which 55 ± 2% of all molecules resided, a short immobile state (26 ± 1%) and a long immobile state (19 ± 2%). The short and long immobile states were characterized by short (0.7 ± 0.1 seconds) and long (3.5 ± 0.9 seconds) immobilization times, respectively. The results are summarized in Figure 1C (the diffusion coefficient of the molecules in the diffusion state was obtained from the analysis of the single-molecule microscopy experiments (see below), and was used as a fixed parameter in the simulations).

To obtain a more complete overview of the mobility pattern of the GR, FRAP was complemented with SMM experiments. Where FRAP experiments give information on the seconds time scale, providing more details on the immobile states, SMM measures dynamics at the sub-second timescale, providing additional information on the diffusing fractions. Moreover, cross-validation was possible where the results of the two methods overlapped. Image sequences were taken with a time lag of 6.25 milliseconds (Figure 1D), and the mobility of molecules was analyzed using particle image-correlation spectroscopy (28). In this method, all possible correlations between the location of molecules in consecutive frames are determined. This way, a cumulative distribution function *(Cdf)* of displacements *R* is generated. This function was generated for the interval between subsequent frames, and between frames two or three lag times apart (resulting in 12.5 ms and 18.75 ms lag time respectively).The *Cdf* for YFP-GR using these three different time lags is shown in Figure 1E. The curves were fitted with a three-population model, which fitted the results better than a two-population model and was chosen for two additional reasons. First, analysis of the same data using a different (unbiased) approach based on phasors demonstrated that two diffusing fractions were present. These data will be published elsewhere (Coppola *et al.*, unpublished). Second, in previous studies fitting the data with one diffusing fraction yielded a diffusing fraction of which the diffusion coefficient was dependent on the DNA binding capacity of the receptor (see also (13)). However, we assume that the fastest component of the mobility pattern of GR should be independent of its DNA binding capacity. As will be presented below, when we used a model with two diffusing fractions, the

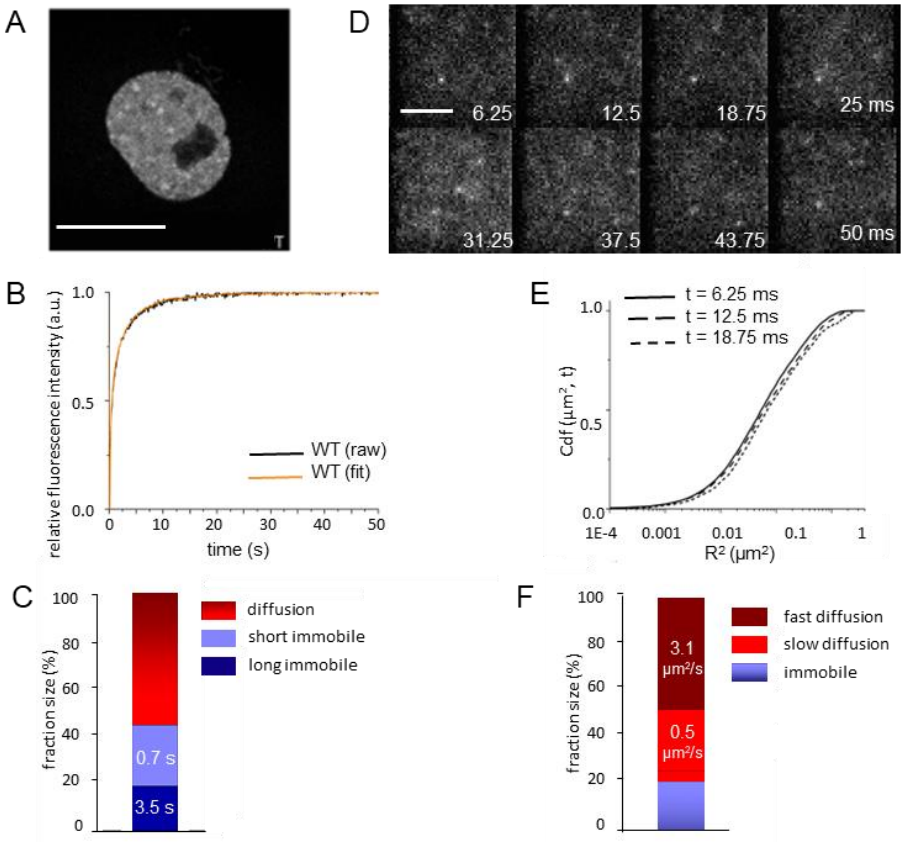

Figure 1. Analysis of WT YFP-GR dynamics using fluorescence recovery after photobleaching (FRAP) and single-molecule microscopy (SMM). (A) Representative confocal microscopy image of COS-1 cells expressing wild type YFP-GR. Two hours post activation with ligand (FP, 5 nM. Scale bar corresponds with 5 µm. (B) FRAP curve of WT YFP-GR. The bleach pulse was given at t= 0 seconds. In each experiment, data points from >30 cells were pooled. The orange line represents the average of the top ten best fits. (C) WT YFP-GR distribution over the diffusion state, the short immobile state and the long immobile state. The time spent in either immobile state is indicated. Data shown are means from five independent experiments. (D) Sequence of eight single molecule images. Scale bar corresponds with 5 µm. (E) Cumulative distribution function of squared displacements for three time lags (6.25, 12.5 and 18.75 ms). Representative distributions shown are based on one independent experiment (>7 cells, per cell, 15 sequences of 8 frames were taken, resulting in >4000 particle localizations per experiment). (F) WT YFP-GR distribution over the fast diffusion state, the slow diffusion state and the immobile state. The diffusion coefficients of the diffusion states are indicated. Data shown are means of 5 independent experiments.

fast diffusing fraction appeared to be independent of the DNA binding capacity.

The results of the fitting showed that 40 ± 7% of YFP-GR molecules occurred in a fast diffusion state, 28 ± 4% in a slow diffusion state and 32 ± 4% in an immobile state. The fast and slow diffusion state were characterized by a fast (3.1 ± 0.4 $\mu m^2/s$) and slow (0.5 ± 0.08 $\mu m^2/s$) diffusion constant, respectively. The results are summarized in Figure 1F. In SMM it is not possible to distinguish the short and long immobilization events found in FRAP (which are in the order of seconds) due to the short time scale of the experiments (in the order of milliseconds).

To determine the average time the receptors reside in a given state and the probabilities of their transition to another state, we developed a continuous time Markov chain (CTMC) model. In this model random times spent in a state are and exponentially distributed, and GRs were allowed to switch between three states (i.e. a fast diffusion, slow diffusion and an immobile state). Model parameters were extracted from fraction sizes and the diffusion coefficients found using SMM and the combined immobilization times from FRAP (see Materials and Methods, Figure S1). Due to the ensemble nature of the data used as input for the model in this study, ranges were determined for all parameters. Within these ranges, the values of all parameters were uniformly distributed.

Using this approach, we found that YFP-GR spent more than 7.5 seconds in the fast diffusion state, whereas the average time spent in the slow diffusion state ranged between 1.2 and 1.4 seconds (Figure 2A). Furthermore, the CTMC model revealed a high transition probability from the fast diffusion state to the slow diffusion state (> 0.80), but a low transition probability to the immobile state (< 0.20) (Figure 2B). From the slow diffusion state, the probability to switch to the immobile state ranged between 0.75 and 0.95 whereas the probability to transit to the fast diffusion state was between 0.05 and 0.25. From the immobile state, the probability of transition to the slow diffusion state was larger than 0.95 and to the fast diffusion state was smaller than 0.05. The transitions and time spent in each state have been summarized in Figure 2C.

From this model a likely transition path emerges that the GR follows in order to reach its target site. The GR showed a remarkably strong preference for transitions from the fast to slow diffusion state, from the slow diffusion state to an immobile state and from an immobile state to the slow diffusion state. To further illustrate the implications of the results of the CTMC model, we employed numerical simulations. In these simulations, the behavior of an individual molecule was described based on the times spent in the immobile, slow diffusion and fast diffusion states and the transition probabilities between these states. A representative diagram showing the simulated behavior of a GR molecule over a period of 200 seconds is presented in Figure 3A.

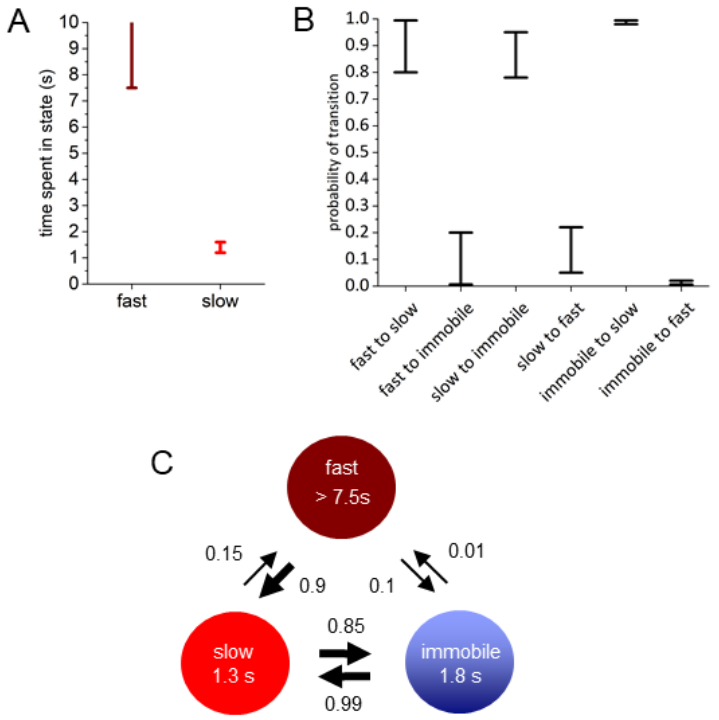

Figure 2. The continuous time Markov chain model applied to SMM data for WT YFP-GR. (A) Time spent in states for WT YFP-GR. The continuous time Markov chain model used here provides ranges of values that are equally likely to represent the true average time spent in this state. (B) Probability of transitions between states for WT YFP-GR. (C) Schematic overview of data presented in A and B, showing probabilities of transition between states (as shown in A; denoted by the arrows) and times spent in the state (as shown in B; reported in the circles).

These results reveal that individual receptors spent a long time in the fast diffusion state, but once it enters the slow diffusion state it will switch repetitively between the slow diffusion and the immobile states before returning to the fast diffusion state. This was visualized by a spatial representation of a numerical simulation in which the behavior of an individual molecule was described based on the times spent in the immobile, slow diffusion and fast diffusion states and the transition probabilities between these states (Figure 3B).

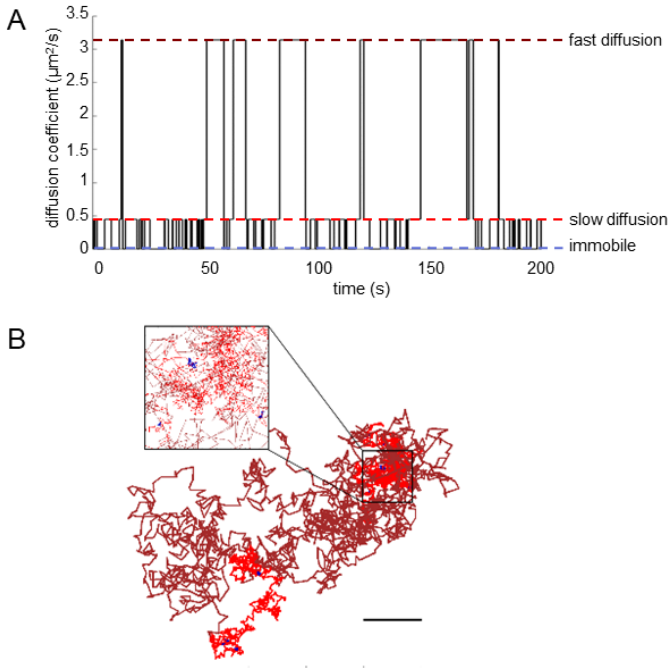

Figure 3. Numerical simulation of the behavior of an individual molecule. The behavior was simulated based on the times spent in the different states and the transition probabilities between these states as shown in Figure 3. (A) Diagram showing transitions between states over time, showing that the GR spends a relatively long periods of time in the fast diffusion state, and once it has left this state, it will repetitively switch between the slow diffusion and immobile state, before returning to the fast diffusion state. (B) Trajectory of the GR moving through the cell nucleus (colors represent different states as described in Figure 3; scale bar represents 2 μm). This trajectory illustrates the compact searching strategy of the GR as a result of repetitive switching. Once the GR has left the free diffusion state (dark red), it is slowed down as a result of nonspecific interactions (light red), which keep it in a restricted area, in which it binds to its specific target sites (blue).

Next, we investigated the role of each of the states in GR function. Here we focused on assessing the DNA binding properties of GR in each of the states by using six mutants of the human GR (K442A, V443A, R447K, R477K and C438Y and ΔDBD) (Figure 4A). In four of these mutants single amino acids were mutated that had been selected based on the crystal structure of the GR DNA-binding-domain (DBD) bound to a GRE (30). Amino acids K442 and V443 were predicted to share hydrogen bonds with nucleobases that are specific to the GRE sequence (30,31). It has been shown that a mutation in K442 reduces the ability of the GR to initiate transcription (32). A naturally occurring mutation of the equivalent amino acid of V443 in the androgen receptor renders this receptor unable to initiate transcription and leads to complete androgen insensitivity in patients (33). Amino acid R447 was predicted to have an interaction with a GRE-specific nucleobase and with components of the backbone of the DNA, and amino acid R477 was predicted to solely have interactions with the backbone of the DNA. Mutation in AR of the equivalent amino acid of R447 was previously shown to make the receptor unable to recognize cognate repsonse elements (34), and to alter AR intranuclear dynamics (14). Mutation of R477 has been demonstrated to render the GR unable to initiate transcription and to result in a shorter recovery time in FRAP experiments (35). Moreover, this mutation naturally occurs in humans leading to primary cortisol resistance (36). A fifth amino acid, C438, was mutated to disrupt the structure of the DBD, since it is one of the four cysteines that create the first zinc finger by non-covalently binding a zinc atom. Finally, a mutant (ΔDBD) was used in which the entire DBD (amino acid 428-490) was deleted (37). Representative confocal images of cells expressing each mutant receptor are presented in Figure S2A.

The effect of each mutation or deletion on *in vitro* DNA binding was determined using an ELISA-based DNA-binding assay. COS-1 cells were transfected with WT or mutant YFP-GR expression vectors. Nuclear extracts were prepared, and the relative binding to a GRE was determined for serial dilutions of these extracts. Subsequently, the DNA binding was plotted against the relative protein concentrations in the nuclear extract, which were determined by measuring YFP fluorescence in the extracts. For WT and mutant YFP-GRs, a one-phase association equation was used to fit the (Figure

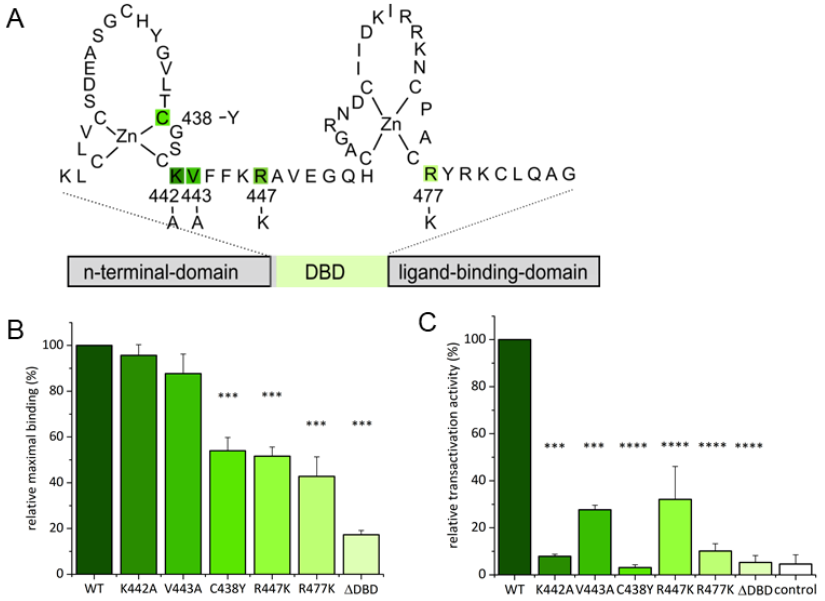

Figure 4. DNA-binding mutants of GR. (A) Schematic diagram of the GR consisting of three domains, the N-terminal domain (amino acid 1-416), the DNA-binding domain (DBD, amino acid 417-490) and the ligand-binding domain (amino acid 491-770). The amino acid sequence for the DBD is given and the mutations used in the present study are indicated. (B) DNA-binding capacity of YFP-GR (WT or mutant) to a GRE *in vitro*. Nuclear extracts were taken from COS-1 cells expressing YFP-GR (WT or mutant) activated with ligand (FP, 5 nM). GR present in these extracts was allowed to bind to a GRE *in vitro* for 1 hour. Subsequently, GR binding was measured using an ELISA-based approach. The maximal binding was determined (Figure S2), and the relative maximal binding is presented for WT and mutant YFP-GR (mean ± s.e.m. of three independent replicates). (C) Transactivation activity of YFP-GR (WT or mutant) in luciferase reporter assay. MMTV-luciferase and CMV-renilla reporter constructs and YFP-GR (WT or mutant) expression vectors were transfected into COS-1 cells and the luciferase activity was measured after FP (5 nM) administration. The relative activity of WT and mutant YFP-GR is shown (mean ± s.e.m. of three independent replicates). As a control, the procedure was performed without cells. Asterisks indicate statistically significant differences from the WT control group (*** $p<0.01$; **** $p<0.001$).

S2B). Subsequently, the maximal DNA binding relative to WT YFP-GR was determined for each mutant (Figure 4B). Mutation of K442 or V443 did not show a significant effect on the relative maximal DNA binding of the GR. Mutation of amino acids R447 and R477 significantly reduced the relative

maximal binding of the GR (52% ± 4% and 43% ± 8%, respectively), as did mutation of C438 (54% ± 6%). The ΔDBD mutant showed the lowest relative maximal binding of the GR to the GRE (17% ± 2%). Taken together these YFP-GRs (WT and mutants) form a range of DNA-binding capacities with WT YFP-GR showing the highest DNA-binding capacity and the YFP-GR ΔDBD mutant showing the lowest DNA-binding capacity.

We next considered the ability of each mutant to initiate transcription. To assess this, a reporter assay was performed in which luciferase gene expression was controlled by a MMTV promoter, containing multiple GREs. In this assay, all mutants showed significantly reduced luciferase activity compared to WT YFP-GR (Figure 4C). The transactivation capacity (relative to WT) of mutants V443A and R447K was 28 ± 2% and 32 ± 14%, respectively, whereas the transcriptional activity of mutants K442, C438Y, R477K and ΔDBD was comparable to a background level (8 ± 1%, 3 ± 1%, 10 ± 3% and 5 ± 3%, respectively). The reduced ability of mutants R447K, R477K, C438Y and ΔDBD to initiate transcription corresponded with their reduced DNA-binding capacity. Interestingly, mutants K442A and V443A were found to be significantly reduced in their ability to activate gene transcription although they showed a negligible reduction in DNA-binding capacity.

Using the DBD mutants we studied the relationship between the mobility pattern of the GR and the DNA-binding capacity. For this purpose, we first performed FRAP experiments on all mutant YFP-GRs (FRAP curves and fits are shown in Figure S3). The percentage of molecules in the diffusion state ranged from 55 ± 2% for WT YFP-GR, which displayed the highest DNA-binding capacity, to 80 ± 4% for the ΔDBD mutant, which has the lowest DNA-binding capacity of all mutants (Figure 5). A correlation analysis was performed which showed that the fraction of YFP-GR molecules in the diffusion state was negatively correlated with the DNA-binding capacity (Figure S4A). The size of the fraction of YFP-GR molecules in the short immobile state was similar between wild type and mutants (approximately 20%) (Figure 5B, Figure S4B), indicating that the occurrence of this state is not dependent on DBD-mediated interactions inside the nucleus. However, slight differences in the time spent in this state were observed (times ranging

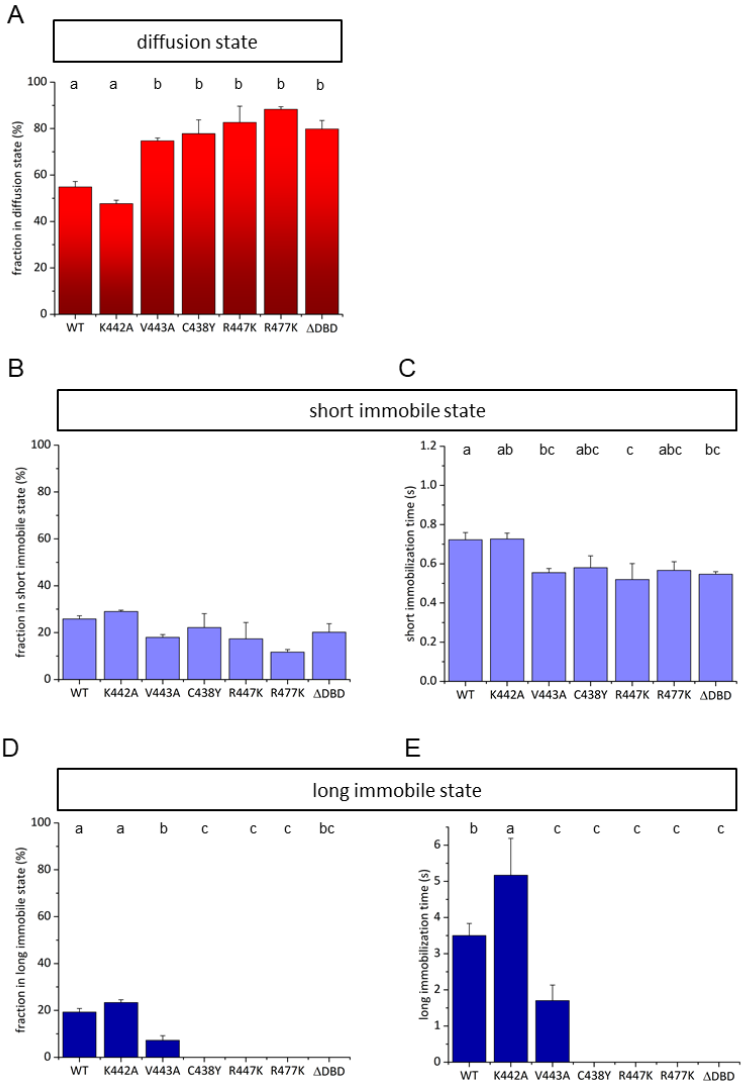

Figure 5. FRAP analysis of WT and mutant YFP-GR dynamics. (A) Size of the fraction of YFP-GRs (WT or mutant) in the diffusion state. (B) Size of the fraction of YFP-GRs (WT or mutant) in the short immobile state. (C) Immobilization time of short immobile fraction of YFP-GRs (WT or mutant). (D) Size of the fraction of YFP-GRs (WT or mutant) in the long immobile state. (E) Immobilization time of long immobile fraction of YFP-GRs (WT or mutant). Data shown are average values ± s.e.m. of three independent replicates (for WT five independent replicates were used). For each condition in each replicate >30 cells were used. Statistical significance between groups ($p<0.01$) is indicated by letters; groups with the same letters belong to a homogenous subset, i.e. are not significantly different.

between ~0.5 and ~0.7 s) (Figure 5C), and these values showed a correlation with the DNA-binding capacity (Figure S4C). Finally, the fraction sizes of YFP-GR molecules in the long immobile state ranged from 19 ± 2% for WT YFP-GR to 23 ± 1% and 7 ± 2% for K442A and V443A respectively, to a complete absence of this fraction in the other mutants with a lower DNA-binding capacity (Figure 5D). This size was positively correlated with the DNA-binding capacity (Figure S4D), as was the immobilization time of this state (Figure 5E, Figure S4E). Apparently, a reduction in the DNA-binding capacity resulted in a complete loss of YFP-GR molecules in the long immobile state, suggesting that this state represents direct DBD-mediated DNA binding.

Subsequently, we studied the effect of the DNA-binding capacity on the intranuclear dynamics by SMM. Firstly, a negative correlation between the size of the fraction of YFP-GR molecules in the fast diffusion state and the DNA-binding capacity was found (Figure S5A), which ranged between ~40% for WT and ~61-64% for mutants ΔDBD, R477, R447, and C438 (Figure 6A). The diffusion coefficient of molecules in this fast diffusion state was not affected by mutations in the DBD (Figure 6B, Figure S5B). Secondly, both the fraction of YFP-GR molecules in the slow diffusion state and the diffusion coefficient of molecules in this state were independent of the DNA-binding capacity (Figure 6C-D, Figure S5C-D).

Finally, the CTMC model was applied to the data acquired on the dynamics of the DBD mutants. No effect of the DNA-binding capacity was observed on the time spent in the fast diffusion state. All mutants had a lower limit for the time spent in this state comparable to WT YFP-GR (7.5 seconds) (Figure 7A). In contrast, the average time spent in the slow diffusion state was affected by the DNA-binding capacity. The mutants showed a lower average time spent in this state (ranging between 0.4 and 0.9 seconds), except for the K442A mutant, which spent a time in the slow diffusion state that was similar to WT YFP-GR (Figure 7B). These results indicate that the time spent in the slow diffusion state is dependent on the DNA-binding capacity of the GR, whereas the time spent in the fast diffusion state is not. Like the WT YFP-GR, all mutant YFP-GRs showed a strong preference for transitions from the fast to the slow diffusion state, from the slow diffusion state to an immobile state

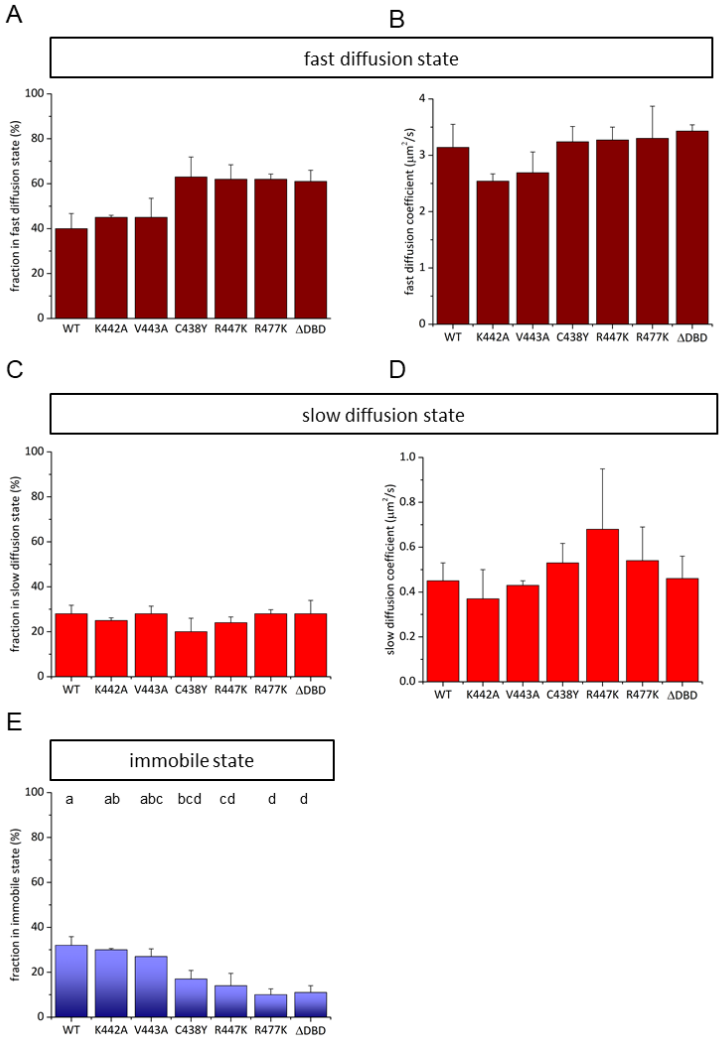

Figure 6. SMM analysis of WT and mutant YFP-GR dynamics. (A) Size of the fraction of YFP-GRs (WT or mutant) in the fast diffusion state. (B) Diffusion coefficient of YFP-GR (WT or mutant) in the fast diffusion state. (C) Size of the fraction of YFP-GRs (WT or mutant) in the slow diffusion state. (D) Diffusion coefficient of YFP-GR (WT or mutant) in the slow diffusion state. (E) Size of the fraction of YFP-GRs (WT or mutant) in the immobile state. Data shown are average values ± s.e.m. of three independent experiments (for WT five independent replicates were used). For each condition in each replicate >7 cells were used. Statistical significance between groups ($p<0.01$) is indicated by letters; groups with the same letters belong to a homogenous subset, i.e. are not significantly different.

and from an immobile state to the slow diffusion state. None of the transitions between states was affected by the DNA-binding capacity (Figure S6A-F).

Thirdly, the size of the fraction of YFP-GR molecules in the immobile state was not influenced by mutation of K442 or V443, but the C438Y, R447K, R477K and ΔDBD mutants showed a significant decrease compared to WT (respectively 17 ± 4%, 14 ± 6%, 10 ± 3%, and 11 ± 3% compared to 32 ± 4%, Figure 6E). This fraction size was positively correlated with the DNA-binding capacity (Figure S5E).

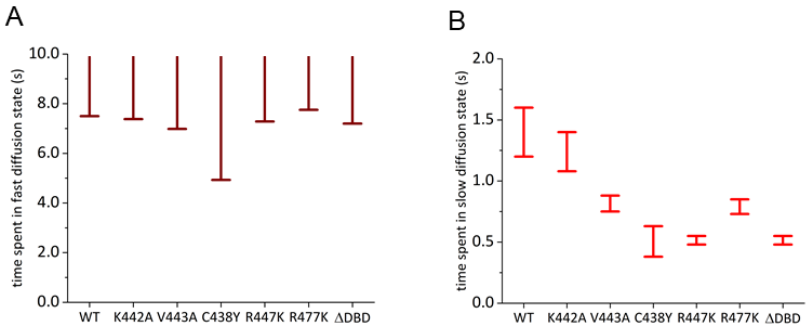

Figure 7. Time spent in different diffusion states for YFP-GR (WT or mutant). The continuous time Markov chain model, applied to the SMM data, provides ranges of values that are equally likely to represent the true average time spent in this state. (A) Time spent in fast diffusion state for YFP-GR (WT or mutant). In this case, the analysis provided only a lower limit for the time spent in the state. (B) Time spent in slow diffusion state for YFP-GR (WT or mutant).

2.3 Discussion

In the present study, we have identified the different states in which the GR occurs in the nucleus, based on its dynamic behavior which was assessed using FRAP and SMM experiments. To determine the biological processes underlying these states, we have used six mutants with reduced DNA-binding capacities. The DNA-binding capacity of these mutants appeared to correlate well with certain mobility parameters, even though this capacity was measured *in vitro*. Additionally, we have developed a CTMC model to determine the time spent in all states and the probability of state-to-state

transitions. By combining the data obtained in these descriptive and functional studies we obtained a comprehensive overview of the dynamics of the GR, which is shown in Figure 8. In this overview all dynamic states in which GR occurs are presented, as well the temporal relations between these states and their function. We present a mechanism for target finding by the GR in which repetitive switching between nonspecific and specific DNA binding plays a central role.

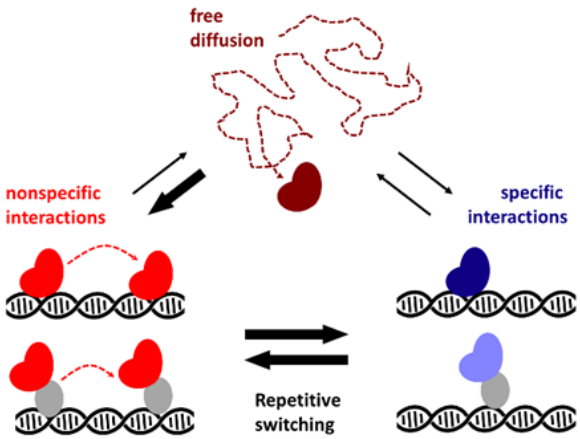

Figure 8. Repetitive switching results in a compact searching strategy. Schematic overview of the intranuclear behavior of the GR, summarizing the results obtained in the present study. Four different states are represented by different colors: a free diffusion state (brown), a state in which GRs interact nonspecifically with DNA (red), and a state in which receptors interact specifically with DNA, either directly (dark blue) or indirectly (light blue). The probability of transition between states is indicated by arrows. The thickness of the arrows represents the likeliness of the transition. After leaving the free diffusion state, GRs most often enter a repetitive switching mode, in which it alternates between specific and nonspecific interactions.

Using the SMM data we identified a fast diffusion state and a slow diffusion state, and using the FRAP results a short immobile state and a long immobile state were revealed. By combining data from FRAP and SMM experiments, four different states were identified based on their dynamic behavior (because of the large difference in kinetics between the slow diffusion and short immobile state, no overlap between these two states is considered).

The fast diffusion state was interpreted as representing freely diffusing GRs, since neither the diffusion coefficient nor the time spent in this state was dependent on the DNA-binding capacity of GR. The diffusion coefficient found for this state (3.1 $\mu m^2/s$) is in the same range as diffusion coefficients that have been reported in other studies for the GR (9.2 $\mu m^2/s$; (22)) and especially of other transcription factors including p53 and STAT1 (3.4 and 3.1 $\mu m^2/s$, respectively; Speil *et al.*, 2011; Mazza *et al.*, 2012). It is likely that these freely diffusing GRs are dimeric or complexed with other proteins (38,39).

The slow diffusion state was characterized by a six-fold lower diffusion coefficient than that of the fast diffusion state (0.5 $\mu m^2/s$). The time spent in this state was largely dependent on the DNA-binding capacity of the receptor, indicating that the diffusion rate of these molecules was affected by interactions with DNA. We suggest that these DNA interactions are non-specific and may include short sections of sliding, hopping and intersegmental exchange (40–43). Non-specific DNA interactions on the time scale of milliseconds have been observed previously in bacteria (24)).

The short immobile state has previously been interpreted as nonspecific DNA binding by us and others (13,14,44), but in the present study its occurrence appeared to be independent of a functional DBD. We therefore suggest that this state represents interactions with DNA that are mediated through the ligand-binding domain or the N-terminal domain. The short immobilization events (which last about 0.6 seconds) could represent tethering events for which direct DNA binding is not necessary and through which the GR is known to regulate the activity of other transcription factors (6,45). Indeed it was recently shown that when AP-1, a known tethering partner for the GR, was knocked out the percentage of GR occurring in the short immobile state was reduced (23).

The long immobile state was entirely dependent on the DNA-binding capacity of the receptor. When the DNA-binding capacity of the receptor was significantly compromised a total absence of molecules in this state was observed. This state was interpreted as representing direct specific DNA-binding by the GR. The long immobilization time (which last about 2.9

seconds) is in the same range as found for the GRs bound to the GREs in live cells (7,12). In the latter study, this population is only present at transcriptionally active sites in the nucleus.

Using the CTMC model, we demonstrate a repetitive switching mechanism for the GR, in which the receptor repeatedly alternates between brief nonspecific DNA interactions and longer immobilizations due to specific DNA binding (Figure 6A). Apparently, a period of the specific DNA binding is most frequently preceded by a period of nonspecific DNA binding, which suggests that the nonspecific DNA binding state facilitates localization of the specific DNA target sites. It has previously been proposed that these nonspecific DNA interactions are necessary to reach a specific site (40–44). During the repetitive switching the GR will remain in a restricted area. As a result, two subsequent specific binding events most often occur at sites that are in close proximity. Thus, repetitive switching is the mechanism through which the searching strategy of transcription factors is compacted. This is visualized by a spatial representation of a numerical simulation in which the behavior of an individual molecule was described based on the times spent in the immobile, slow diffusion and fast diffusion states and the transition probabilities between these states (Figure 3B). Compact search strategies have been proposed before as a way to facilitate target finding (39,42), and here we present repetitive switching as the mechanism through which the GR compacts its target searching.

These periods of repetitive switching are preceded by extended periods of free diffusion through the nucleoplasm. Interestingly, the GR spends on average more than ten seconds in the free diffusion state. With a diffusion coefficient of 3.1 $\mu m^2/s$, this allows it to traverse large areas of the nucleus unhindered. It is therefore highly unlikely that it does not encounter accessible DNA, which strongly suggests that the GR is unable to bind DNA in this state. This could be explained if the GR enters the repetitive switching mode by undergoing a conformational change or complex formation, which enables it to interact with DNA. This may involve multimerization of the receptor (46).

The use of a range of mutants provided a powerful tool to investigate the effect of the DNA-binding capacity on GR dynamics, but it also appeared to be relevant to establish which amino acid/base pair interactions are crucial in GR function. Changes in amino acids R447 and R477 completely abolished the long immobilization times, which suggests that R447 and R477, which are known to interact with the backbone of the DNA, are of great importance for stabilization of DNA binding to GREs. This is in line with previous studies, which showed that mutations in amino acid R477 resulted in increased mobility in FRAP experiments (35).

Mutation of the amino acids K442 and V443 showed little effect on DNA binding *in vitro* or on the immobilization times of the receptor in living cells. However, these mutants are compromised in their ability to activate transcription, showing that DNA binding alone is not sufficient for transcription initiation. These amino acids are known to directly interact with GRE-specific nucleobases (30,31). We therefore suggest that the interactions between K442 and V443 and specific nucleobases might be involved in a conformational modification critical in transcription initiation, alluding to an allosteric modulation of the GR by the DNA through which additional specificity is achieved (3).

In summary, in this study we have described and interpreted the dynamics of the GR, and present a detailed picture of transcription factor behavior in the nucleus. This reveals the mechanism by which a transcription factor reaches its cognate recognition sequence, which involves repetitive switching between a state of non-specific and specific DNA binding.

2.4 Material and Methods

DNA constructs

Five single point mutations were made in the pEYFP-GR plasmid (8), yielding mutants C438Y, K442A, V443A, R447K and R477K. Mutagenesis was carried out using the QuikChange II Site-Directed Mutagenesis Kit (Agilent, Santa Clara, CA). Successful mutation was confirmed by sequence analysis. A sixth mutant, the GR Δ428-490 deletion mutant has been described previously (8). For luciferase assays, two additional plasmids were used: pMMTVluc,

containing the mouse mammary tumor virus (MMTV) promoter adjacent to the firefly luciferase cDNA sequence, and pRL (Promega, Madison, WI) containing the cytomegalovirus (CMV) promoter adjacent to the renilla luciferase cDNA.

CELL CULTURE AND TRANSFECTION

COS-1 originally obtained from American Type Culture Collection (ATCC, Manassas, VA, USA). Monthly checks on Mycoplasma and other bacterial infections were performed. Cells were cultured in Dulbecco's Modified Eagle's Medium (DMEM, ThermoFisher Scientific, Waltman, MA) without phenol red supplemented with 10% fetal calf serum (FCS) at 37°C with 5% CO_2. One day prior to transfection, cells were plated in 6-well plates. When cells were used for imaging, coverslip glasses (ThermoFisher Scientific), Waltman, MA were placed at the bottom of the well prior to plating the cells. Transfection was carried out using FuGENE HD (Promega, Madison, WI), according to the manufacturer's instructions. Briefly, for each well, a mix was made containing 500 ng of DNA and 3 µl of FuGENE in a total volume of 500 µl DMEM. This mix was incubated at room temperature for one hour and added to the cells. Medium was refreshed the following day.

CONFOCAL LASER SCANNING MICROSCOPY

For confocal microscopy, cells were transfected with a pEYFP-GR plasmid encoding the wild type receptor or a mutated version. One day post transfection fluticasone propionate (FP, 5 nM, Sigma Aldrich, Zwijndrecht, Netherlands) was added. Three to six hours after addition of the ligand, coverslips onto which the cells had been plated were placed in a metal ring holder and 1 ml of DMEM without FCS was added. Confocal images of the cells were taken using a Leica SPE confocal microscope equipped with a 488 nm laser and a 100x/1.4NA oil immersion objective (Leica Microsystems, Amsterdam, Netherlands).

DNA-BINDING ASSAY AND LUCIFERASE REPORTER ASSAY

Cells were transfected with the pEYFP-GR plasmid (WT or a mutated version). One day post transfection FP (5 nM) was added. Three hours after addition of the ligand, nuclear extracts were collected using the Nuclear Extraction kit

(Active Motif, La Hulpe, Belgium). More than 5x10^6 cells were used per sample. In order to measure the relative YFP-GR concentrations in the samples, fluorescence intensities of the lysates were determined using a Turner BioSystems Modulus Microplate reader (Promega, Madison, WI). A series of eight 1:2 dilutions of these samples was used to perform a DNA-binding assay using the GR TransAM kit (Active Motif, La Hulpe, Belgium) following the manufacturer's instructions. The sequence of the oligonucleotide used to measure the GR binding was 5' – GGTACAnnnTGTTCT – 3'. DNA binding activity was assessed by measuring absorbance at 450 nm wavelength, corrected for background illumination at 600 nm using the Turner BioSystems Modulus Microplate reader (Promega, Madison, WI). A negative control measurement (without cellular extract) was used to correct the obtained values at both wavelengths. The determined DNA-binding activities were plotted as a function of the relative fluorescence intensities of the lysates, combining data points from the three independent experiments. A one-phase association equation was used to fit the data:

$$y = y_o + (B_{max} - y_0)\,(1 - e^{-ks}) \qquad \text{Eq. 1}$$

Where y_0 is the y-intercept and B_{max} is the plateau value. The determined value for *k* was then used as a constant on the curve of each individual experiment to more accurately determine B_{max}, which represents the maximal binding achieved at the YFP-GR concentration range used in this experiment (Graphpad Software, La Jolla, CA). This maximal binding was normalized to the maximal binding of the WT YFP-GR. The data shown are averages (± s.e.m.) of the three independent experiments. A one-way ANOVA was performed with a Holm-Sidak test to correct for multiple comparisons (OriginLab, Northampton, MA). Statistical significance was accepted at $p<0.01$.

For the luciferase assay, cells were transfected with pEYFP-GR plasmid (WT or a mutated version), the MMTV plasmid and the CMV plasmid simultaneously. Transfected cells were induced with FP (5 nM) for up to 10 hours. Adherent cells were lysed using passive lysis buffer (Promega, Madison, WI) . More than 1x10^6 cells were used per sample.The dual-luciferase reporter assay system was used to detect firefly and Renilla

luciferase activities (Promega, Madison, WI). Luciferase activity was measured using the Turner BioSystems Modulus Microplate reader (Promega, Madison, WI). As a control, the procedure was performed without cells. The data shown are averages (± s.e.m.) of the three independent replicatess. A one-way ANOVA was performed with a Bonferroni test to correct for multiple comparisons (OriginLab, Northampton, MA). Statistical significance was accepted at $p<0.01$.

FLUORESCENCE RECOVERY AFTER PHOTOBLEACHING (FRAP)

Cells were transfected with the plasmid pEYFP-GR (WT or a mutated version). One day after transfection and 3-6 hours prior to imaging, FP (5nM) was administered. The coverslip on which the cells were grown was placed into a metal ring holder and 1 ml of DMEM without fetal calf serum was added. Cells were imaged at 37°C for a maximum of 2 hours using a Zeiss LSM510 META confocal laser scanning microscope with a 40x/1.3NA oil-immersion objective (Carl Zeiss, Breda, Netherlands). Fluorescence recovery after photobleaching (FRAP) experiments were performed as described previously (13,14). Briefly, a narrow strip spanning the entire width of the nucleus was scanned at 514 nm excitation (using an argon laser (30 mW)) with short intervals (100 ms) at low laser power. Fluorescence intensity was recorded using a 560-nm long pass filter. After 40 frames a high intensity (100% laser power) 100 ms bleach pulse was administered and recovery of fluorescence at the bleached strip was monitored for 55 seconds at 100 millisecond intervals. Fluorescence intensities were normalized to baseline intensity and FRAP curves were generated by plotting the fluorescence intensity over time. For each receptor (WT or mutant), minimally 30 cells were imaged in three independent replicates.

To analyze the experimental FRAP curves quantitatively, they were compared to curves generated using Monte Carlo simulations. This method has been described extensively previously and the program is available upon request (27,47). This approach was previously used to determine the mobility pattern of AR and GR (13,14) A 3-population model was used, containing a diffusing population and two populations characterized by distinct immobilization times. A model with two immobile populations fits

the data significantly better than a model with one immobile population. Under certain conditions however, only one immobile population was found, indicating the absence of a bias (14). The computer-simulated curves were subsequently compared to the experimental data by least squares analysis. For this purpose, the diffusion coefficient of the mobile subpopulation obtained from the analysis of the single-molecule microscopy experiments was used as a fixed parameter. This left 4 parameters as variables: the sizes of the short immobile and the long immobile population (both ranging from 0–90%), and the times spent in the short and long immobile state (ranging from 0.1 to 1 seconds and from 1 to 300 seconds, respectively).

The data shown are averages (± s.e.m.) of the three independent experiments. Data were statistically analyzed by restricted maximum likelihood (REML) with a linear mixed model using Genstat (VSNi, Hemel Hempstead, UK). The fixed part of the model were factors (measurement) day and cell-line (control and mutations) while the random part was block (day) and cells within block. Residuals were checked for the equal variance assumption. Comparisons of means/homogenous subsets were based on Fischer's protected least significance difference test. In addition, values for each parameter were plotted as a function of the relative maximal DNA-binding capacity. Regression analysis was performed by ANOVA (OriginLab, Northampton, MA). Statistical significance was accepted at $p<0.01$.

SINGLE-MOLECULE MICROSCOPY

One day after transfection with the pEYFP-GR plasmid (WT or a mutated version), FP (5 nM) was administered to the cells. Between 3 and 6 hours after FP administration, coverslips containing the transfected cells were placed into a metal ring holder and 1 ml DMEM was added. Cells were imaged at 37°C and 5% CO_2 for a maximum of 2 hours using a wide-field fluorescence microscope equipped with a 100x/1.4NA oil-immersion objective (Carl Zeiss, Breda, Netherlands) as described previously (13,14,48). Illumination was performed using a 514 nm argon laser at an intensity of 4 kW/cm^2. Illumination of the sample for 3 ms was controlled through an acousto-optical tunable filter (AA Opto Electronic, Orsay, France). Cells expressing the fluorescent proteins were photobleached until individual

fluorescence signals could be distinguished. Images were recorded on a back-illuminated CCD camera (Princeton, Instruments, Trenton, NJ) before being digitized (0.202 µm/pixel). Three individual experiments were performed. Cells were randomly selected. In each experiment, seven cells were imaged for each mutant. For each cell, fifteen sequences of eight frames were taken. The time lag between subsequent frames was 6.25 ms.

The location of individual molecules was determined by fitting a 2D Gaussian to each signal (custom script available upon request (49,50)). The location of the molecule was defined by the center of this peak determined to an accuracy of 0.16 pixel (32 nm). Individual peaks were excluded based on a threshold for the relative localization error. Subsequently, the mobility was analyzed by combining data from all sequences of eight frames (for each experimental condition, more than 4000 molecule localizations were recorded per individual experiment). Analysis was performed using particle image-correlation spectroscopy (PICS (28)), using up to three successive intervals between frames. In PICS analysis, individual particles are not tracked, but all possible correlations between the location of molecules in consecutive frames are determined. This way, a cumulative distribution function *(Cdf)* of displacements *R* is generated. This function was generated for the interval between subsequent frames, and between frames two or three lag times apart (resulting in 12.5 ms and 18.75 ms lag time respectively). For each time interval, a three-population model was used to fit the data, in order to determine the fraction of molecules α in each of the three populations and their respective diffusion coefficients *(D)*. The model is given by the following equation:

$$Cdf(R^2) = 1 - \left(\alpha_1 \exp\left(\frac{R^2}{4D_1 t + 4\sigma^2}\right) - \alpha_2 \exp\left(\frac{R^2}{4D_2 t + 4\sigma^2}\right) - \alpha_3 \exp\left(\frac{R^2}{4\sigma^2}\right)\right)$$

Eq. 2

The data shown are averages (± s.e.m.) of the three independent experiments. Data were statistically analyzed by restricted maximum likelihood (REML) with a linear mixed model using Genstat (VSNi, Hemel Hempstead, UK). The fixed part of the model were factors (measurement) day and cell-line (control and mutations) while the random part was block

(day) and cells within block. Residuals were checked for the equal variance assumption. Comparisons of means/homogenous-subsets were based on Fischer's protected least significance difference test. In addition, values for each parameter were plotted as a function of the relative maximal DNA-binding capacity. Regression analysis was performed by ANOVA (OriginLab, Northampton, MA). Statistical significance was accepted at $p<0.01$.

CONTINUOUS TIME MARKOV CHAIN MODEL ANALYSIS

The cumulative probability distribution function *(Cdf)*, obtained from the single-molecule data, was used to extract additional dynamic parameters and time scales of motions. Under the framework of a continuous-time Markov chain (CTMC) model, the exact occupation probability distribution was implemented for particles undergoing a three-state intermittent behavior between two diffusion states and one immobile states, as derived from (51).

In brief, the cumulative distribution function *Cdf(R^2)* has the following form:

$$Cdf(R^2) = R\int_0^\infty dk\, J_1(kR)\, e^{-\sigma^2 k^2}\, \mathcal{L}^{-1}\{P(k,s)\} \qquad \text{Eq. 3}$$

where $J(kR)$ is the Bessel function of the first kind (of order 1), σ is the positional accuracy, $\mathcal{L}^{-1}\{P(k,s)\}$ is the inverse Laplace transform of the Fourier-Laplace occupation probability $P(k,s)$. The three-state occupation probability $P(k,s)$ used in the CTMC model is given by:

$$P(k,s) = \frac{1}{2}\sum_{\substack{i=1\\ j=1}}^{3}\Big(1-\varphi_i(k,s)\varphi_j(k,s)\Big)^{-1}\Big(\big(1-\delta_{ij}\big)\,\varphi_i(k,s)\varphi_j(k,s)\frac{\pi_j}{\lambda_i} + \delta_{ij}\varphi_i(k,s)\frac{\pi_i}{\lambda_j}\Big) \qquad \text{Eq. 4}$$

where λ_i represents the average transition rate$\lambda_i = 1/T_i$, where T_i is the average time spent in the state *i*), $\varphi(k,s) = \lambda_i/(s + k^2 D_i + \lambda_i)$ the mobility density of state *i* (with D_i as the diffusion coefficient), and π_i the steady-state probability. In the CTMC framework, these steady-state probabilities are defined from the relation:

$$\pi_1\ \pi_2\ \pi_3 \begin{pmatrix} -\lambda_1 & \lambda_1 p_{12} & \lambda_1 p_{13} \\ \lambda_2 p_{21} & -\lambda_2 & \lambda_2 p_{23} \\ \lambda_3 p_{31} & \lambda_3 p_{32} & -\lambda_3 \end{pmatrix} = \begin{pmatrix} 0 \\ 0 \\ 0 \end{pmatrix} \quad \text{Eq. 5}$$

where p_{ij} is the transition probability from state *i* to state *j* ($j \neq i$), under the conditions $0 < p_{ij} < 1$ and $\sum_{j=1, j\neq i}^{3} p_{ij} = 1\ \forall\ i = 1, 2, 3$. Hence, the steady-state probabilities are dependent on both the transition rates and the transition probabilities (i.e. $\pi_i \equiv \pi_i(\lambda_i, p_{ij})$ under the condition $\pi_1 + \pi_2 + \pi_3 = 1$). In the model it is assumed that after spending the time T in one state, the molecule, must switch to either of the two remaining states. Hence, the probability of transition from the fast diffusion state to an immobile state was obtained as the complementary to 1 of the probability to transition from the fast diffusion state to the slow diffusion state. In the following, the immobile state was labeled as state '3', while the two diffusion states were labeled as '1' and '2'.

It is noteworthy to mention here that the three-state CTMC model introduces three additional free parameters to be estimated (i.e. the transition rates $\lambda_1, \lambda_2, \lambda_3$), with respect to the 3-population model for independent populations presented above. In addition, the non-linear dependency of the steady-state probabilities on the transition probability and rates highly affects the convergence of any fitting routine to an optimal solution. Indeed, a local minimum might give estimates of π_i and λ_i that inserted in the CTMC framework produce unacceptable values for the transition probabilities (i.e. $p_{ij} < 0$ or $p_{ij} > 1$). Therefore, for a robust estimation of the dynamic parameters, we decided to proceed with a multi-step optimization algorithm. First, we noted that for time scales smaller than the switching times, the three-state CTMC model can be well approximated by the three (independent) populations model. This condition was indeed held in our experiments in which the maximum time-lag (18.75 ms) was smaller than e.g. the immobilization times (approximately 1 second) obtained from the FRAP analysis.

We then determined the dynamic parameters by fitting the *Cdf* with the three independent populations model (Figure 1F). After fixing the average time spent in the immobile state $T_3 = 1/\lambda_3$, from Figure S1A), we estimated

the values for T_1 and T_2 that inserted in CTMC framework with $\pi_i \approx \alpha_i$ gave acceptable results for the transition probabilities (i.e. $0 < p_{ij} < 1$) (Figure S1B). For every combination of T_1 and T_2 from the acceptable solutions (the time-steps can be arbitrarily small), we numerically calculated the theoretical *Cdf* for the CTMC model and the squared residuals, with respect to the estimated three independent populations model for the first time-lag t=6.25 ms. All values of the squared residuals below a given threshold corresponded to equally optimal values for T_1 and T_2. This threshold was defined as the residual value $Res(\hat{\imath})$ for which $(Res(\hat{\imath}) - \min(Res))/\max(Res) - \min(Res)) = 5\%$. Therefore, it allowed us to set lower (and potentially upper) bounds for T_1 and T_2. For any optimal $T_1 - T_2$ combination, we could additionally estimate the lower and upper bounds of the transition probabilities from CTMC framework (red solid line, Figure S1C). Although we were seeking for three unknowns from three equations, the non-linearity of CTMC framework prevented us to obtain a single unique solution for every ($\pi_1, \pi_2, \pi_3, T_1, T_2, T_3$) combination. These limitations arise from the ensemble nature of our *Cdf*-based approach (i.e. $\pi_1 + \pi_2 + \pi_3 = 1$ holds without giving us access to the normalization factor that is necessary to uniquely solve the equation for the steady state probabilities).

ACKNOWLEDGEMENTS

The authors would like to thank Derk te Winkel for technical assistance and Paul Keizer (Wageningen University & Research) for help with the statistical analysis of the data.

FUNDING

This work is part of the research programme of the Foundation for Fundamental Research on Matter (FOM), which is part of the Netherlands Organisation for Scientific Research (NWO). Funding for open access charge: Leiden University.

REFERENCES

1. Beato M, Klug J. Steroid hormone receptors: an update. Hum Reprod Updat. 2000;6(3):225–36.

2. Polman JAE, de Kloet ER, Datson NA. Two Populations of Glucocorticoid Receptor-Binding Sites in the Male Rat Hippocampal Genome. Endocrinology. 2013;154(5):1832–44.

3. Meijsing SH, Pufall MA, So AY, Bates DL, Chen L, Yamamoto KR. DNA Binding Site Sequence Directs Glucocorticoid Receptor Structure and Activity. Science. 2009;324(5925):407–10.

4. Hudson WH, Youn C, Ortlund EA. The structural basis of direct glucocorticoid-mediated transrepression. Nat Struct Mol Biol. 2013;20(1):53–8.

5. Surjit M, Ganti KP, Mukherji A, Ye T, Hua G, Metzger D, et al. Widespread negative response elements mediate direct repression by agonist-liganded glucocorticoid receptor. Cell. 2011;145(2):224–41.

6. Ratman D, Vanden Berghe W, Dejager L, Libert C, Tavernier J, Beck IM, et al. How glucocorticoid receptors modulate the activity of other transcription factors: A scope beyond tethering. Mol Cell Endocrinol. 2013;380(1–2):41–54.

7. McNally JG, Muller WG, Walker D, Wolford R, Hager GL. The glucocorticoid receptor: rapid exchange with regulatory sites in living cells. Science (80-). 2000;287(5456):1262–5.

8. Schaaf MJ, Cidlowski JA. Molecular determinants of glucocorticoid receptor mobility in living cells: the importance of ligand affinity. Mol Cell Biol. 2003;23(6):1922–34.

9. Schaaf MJ, Lewis-Tuffin LJ, Cidlowski JA. Ligand-selective targeting of the glucocorticoid receptor to nuclear subdomains is associated with decreased receptor mobility. Mol Endocrinol. 2005;19(6):1501–15.

10. Mueller F, Wach P, McNally JG. Evidence for a Common Mode of Transcription Factor Interaction with Chromatin as Revealed by Improved Quantitative Fluorescence Recovery after Photobleaching. Biophys J. 2008;94(8):3323–39.

11. Stavreva DA, Muller WG, Hager GL, Smith CL, McNally JG. Rapid glucocorticoid receptor exchange at a promoter is coupled to transcription and regulated by chaperones and proteasomes. Mol Cell Biol. 2004;24(7):2682–97.

12. Morisaki T, Muller WG, Golob N, Mazza D, McNally JG. Single-molecule analysis of transcription factor binding at transcription sites in live cells. Nat Commun. 2014;5:4456.

13. Groeneweg FL, van Royen ME, Fenz S, Keizer VIP, Geverts B, Prins J, et al. Quantitation of glucocorticoid receptor DNA-binding dynamics by single-molecule microscopy and FRAP. PLoS One. 2014;9(3):e90532.

14. Van Royen ME, van Cappellen WA, Geverts B, Schmidt T, Houtsmuller AB, Schaaf MJ. Androgen receptor complexes probe DNA for recognition sequences by short random interactions. J Cell Sci. 2014;127(Pt 7):1406–16.

15. Farla P, Hersmus R, Geverts B, Mari PO, Nigg AL, Dubbink HJ, et al. The androgen receptor ligand-binding domain stabilizes DNA binding in living cells. J Struct Biol. 2004;147(1):50–61.

16. Farla P, Hersmus R, Trapman J, Houtsmuller AB. Antiandrogens prevent stable DNA-binding of the androgen receptor. J Cell Sci. 2005;118(Pt 18):4187–98.

17. van Royen ME, Cunha SM, Brink MC, Mattern KA, Nigg AL, Dubbink HJ, et al. Compartmentalization of androgen receptor protein-protein interactions in living cells. J Cell Biol. 2007;177(1):63–72.

18. Stenoien DL, Patel K, Mancini MG, Dutertre M, Smith CL, O'Malley BW, et al. FRAP reveals that mobility of oestrogen receptor-alpha is ligand- and proteasome-dependent. Nat Cell Biol. 2001;3(1):15–23.

19. Marcelli M, Stenoien DL, Szafran AT, Simeoni S, Agoulnik IU, Weigel NL, et al. Quantifying effects of ligands on androgen receptor nuclear translocation, intranuclear dynamics, and solubility. J Cell Biochem. 2006;98(4):770–88.

20. Dundr M, Hoffmann-Rohrer U, Hu Q, Grummt I, Rothblum LI, Phair RD, et al. A kinetic framework for a mammalian RNA polymerase in vivo. Science (80-). 2002;298(5598):1623–6.

21. Gorski SA, Snyder SK, John S, Grummt I, Misteli T. Modulation of RNA polymerase assembly dynamics in transcriptional regulation. Mol Cell. 2008;30(4):486–97.

22. Gebhardt JC, Suter DM, Roy R, Zhao ZW, Chapman AR, Basu S, et al. Single-molecule imaging of transcription factor binding to DNA in live mammalian cells. Nat Methods. 2013;10(5):421–6.

23. Paakinaho V, Presman DM, Ball DA, Johnson TA, Schiltz RL, Levitt P, et al. Single-molecule analysis of steroid receptor and cofactor action in living cells. Nat Commun. 2017;8:15896.

24. Elf J, Li GW, Xie XS. Probing transcription factor dynamics at the single-molecule level in a living cell. Science (80-). 2007;316(5828):1191–4.

25. Speil J, Baumgart E, Siebrasse JP, Veith R, Vinkemeier U, Kubitscheck U. Activated STAT1 transcription factors conduct distinct saltatory movements in the cell nucleus. Biophys J. 2011;101(11):2592–600.

26. Mazza D, Abernathy A, Golob N, Morisaki T, McNally JG. A benchmark for chromatin binding measurements in live cells. Nucleic Acids Res. 2012;40(15):e119.

27. van Royen ME, Farla P, Mattern KA, Geverts B, Trapman J, Houtsmuller AB. Fluorescence recovery after photobleaching (FRAP) to study nuclear protein

dynamics in living cells. Methods Mol Biol. 2009;464:363–85.

28. Semrau S, Schmidt T. Particle image correlation spectroscopy (PICS): retrieving nanometer-scale correlations from high-density single-molecule position data. Biophys J. 2007;92(2):613–21.

29. Coppola S, Keizer VIP, Schaaf MJM, Schmidt TS. A TOOL-ZERO TO DETECT AND QUANTIFY STOCHASTIC PROCESSES IN LIVE CELLS. Prep.

30. Luisi BF, Xu WX, Otwinowski Z, Freedman LP, Yamamoto KR, Sigler PB. Crystallographic analysis of the interaction of the glucocorticoid receptor with DNA. Nature. 1991;352(6335):497–505.

31. Nordeen SK, Suh BJ, Kühnel B, Hutchison IIICA. Structural Determinants of a Glucocorticoid Receptor Recognition Element. Mol Endocrinol. 1990;4(12):1866–73.

32. Meyer T, Starr DB, Carlstedt-Duke J. The rat glucocorticoid receptor mutant K461A differentiates between two different mechanisms of transrepression. J Biol Chem. 1997;272(34):21090–5.

33. Lobaccaro JM, Poujol N, Chiche L, Lumbroso S, Brown TR, Sultan C. Molecular modeling and in vitro investigations of the human androgen receptor DNA-binding domain: application for the study of two mutations. Mol Cell Endocrinol. 1996;116(2):137–47.

34. Shaffer PL, Jivan A, Dollins DE, Claessens F, Gewirth DT. Structural basis of androgen receptor binding to selective androgen response elements. Proc Natl Acad Sci U S A. 2004;

35. Kino T, Liou S-H, Charmandari E, Chrousos GP. Glucocorticoid Receptor Mutants Demonstrate Increased Motility Inside the Nucleus of Living Cells: Time of Fluorescence Recovery After Photobleaching (FRAP) Is an Integrated Measure of Receptor Function. Mol Med. 2004;10(7–12):80–8.

36. Ruiz M, Lind U, Gåfvels M, Eggertsen G, Carlstedt-Duke J, Nilsson L, et al. Characterization of two novel mutations in the glucocorticoid receptor gene in patients with primary cortisol resistance. Clin Endocrinol (Oxf). 2001;55(3):363–71.

37. Hollenberg SM, Giguere V, Segui P, Evans RM. Colocalization of DNA-binding and transcriptional activation functions in the human glucocorticoid receptor. Cell. 1987;49(1):39–46.

38. Presman DM, Ogara MF, Stortz M, Alvarez LD, Pooley JR, Schiltz RL, et al. Live cell imaging unveils multiple domain requirements for in vivo dimerization of the glucocorticoid receptor. PLoS Biol. 2014;12(3):e1001813.

39. Hager GL, McNally JG, Misteli T. Transcription Dynamics. Mol Cell. 2009;35(6):741–53.

40. van Royen ME, Zotter A, Ibrahim SM, Geverts B, Houtsmuller AB. Nuclear proteins:

finding and binding target sites in chromatin. Chromosom Res. 2011;19(1):83–98.

41. Normanno D, Dahan M, Darzacq X. Intra-nuclear mobility and target search mechanisms of transcription factors: A single-molecule perspective on gene expression. Biochim Biophys Acta - Gene Regul Mech. 2012;1819(6):482–93.

42. Izeddin I, Récamier V, Bosanac L, Cissé II, Boudarene L, Dugast-Darzacq C, et al. Single-molecule tracking in live cells reveals distinct target-search strategies of transcription factors in the nucleus. Elife. 2014;3:e02230.

43. Hammar P, Leroy P, Mahmutovic A, Marklund EG, Berg OG, Elf J. The lac Repressor Displays Facilitated Diffusion in Living Cells. Science (80-) [Internet]. American Association for the Advancement of Science; 2012;336(6088):1595–8. Available from: http://science.sciencemag.org/content/336/6088/1595

44. Chen J, Zhang Z, Li L, Chen BC, Revyakin A, Hajj B, et al. Single-molecule dynamics of enhanceosome assembly in embryonic stem cells. Cell. 2014;156(6):1274–85.

45. Kassel O, Herrlich P. Crosstalk between the glucocorticoid receptor and other transcription factors: Molecular aspects. Mol Cell Endocrinol. 2007;275(1–2):13–29.

46. Presman DM, Ganguly S, Schiltz RL, Johnson TA, Karpova TS, Hager GL. DNA binding triggers tetramerization of the glucocorticoid receptor in live cells. Proc Natl Acad Sci U S A. 2016;113(29):8236–41.

47. Geverts B, van Royen ME, Houtsmuller AB. Analysis of biomolecular dynamics by FRAP and computer simulation. Methods Mol Biol. 2015;1251:109–33.

48. Harkes R, Keizer VIP, Schaaf MJ, Schmidt T. Depth-of-Focus Correction in Single-Molecule Data Allows Analysis of 3D Diffusion of the Glucocorticoid Receptor in the Nucleus. PLoS One. 2015;10(11):e0141080.

49. Harms GS, Cognet L, Lommerse PH, Blab GA, Schmidt T. Autofluorescent proteins in single-molecule research: applications to live cell imaging microscopy. Biophys J. 2001;80(5):2396–408.

50. Schmidt T, Schütz GJ, Baumgartner W, Gruber HJ, Schindler H. Imaging of single molecule diffusion. Proc Natl Acad Sci U S A. 1996;93(7):2926–9.

51. Coppola S, Caracciolo G, Schmidt T. Exact occupation probabilities for intermittent transport and application to image correlation spectroscopy. New J Phys [Internet]. 2014;16(11):113057. Available from: http://stacks.iop.org/1367-2630/16/i=11/a=113057

2.5 SUPPLEMENTAL FIGURES

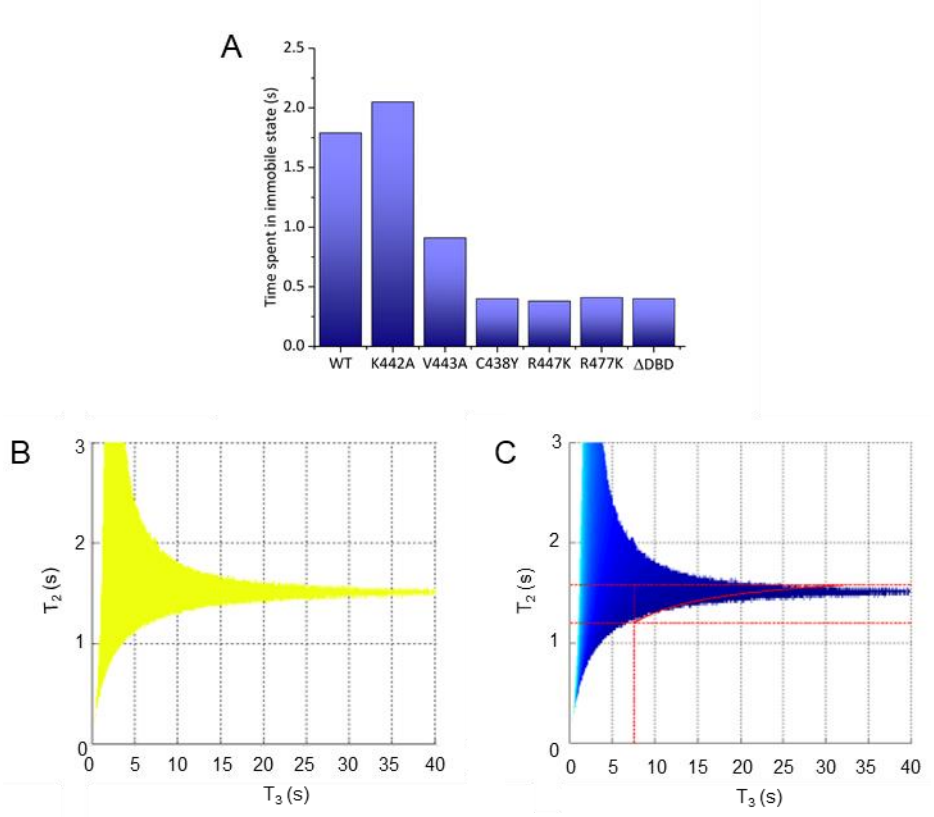

Supplemental figure 1. The Continuous Time Markov Chain Model. (A) Time spent in the immobile state for YFP-GR (WT or mutant). A weighted average was taken of the time spent in either the short or the long immobile state as obtained from FRAP experiments (shown in Figures 6C and 6E respectively). Data shown were taken as input parameters in the continuous time Markov chain model. (B) Acceptable solution for time spent in state. The time spent in the slow diffusion state is plotted against the time spent in the fast diffusion state. Not all time combinations give acceptable solutions for the probabilities. Therefore the possible solutions for the time spent in the state are constrained. They are depicted in yellow. (C) Thresholding the surface of acceptable solutions for the time spent in the state. A threshold was set on the acceptable solutions for the time spent in the state based on the residuals. The size of the residuals are indicated by the color gradient. The threshold (indicated by the red curve) was set at 5% of the of the maximum. All solutions below this threshold are equally likely to be a valid combination of solutions and give rise to the ranges (intercept of the dotted red lines with the axis) depicted in Figures 2 and 7.

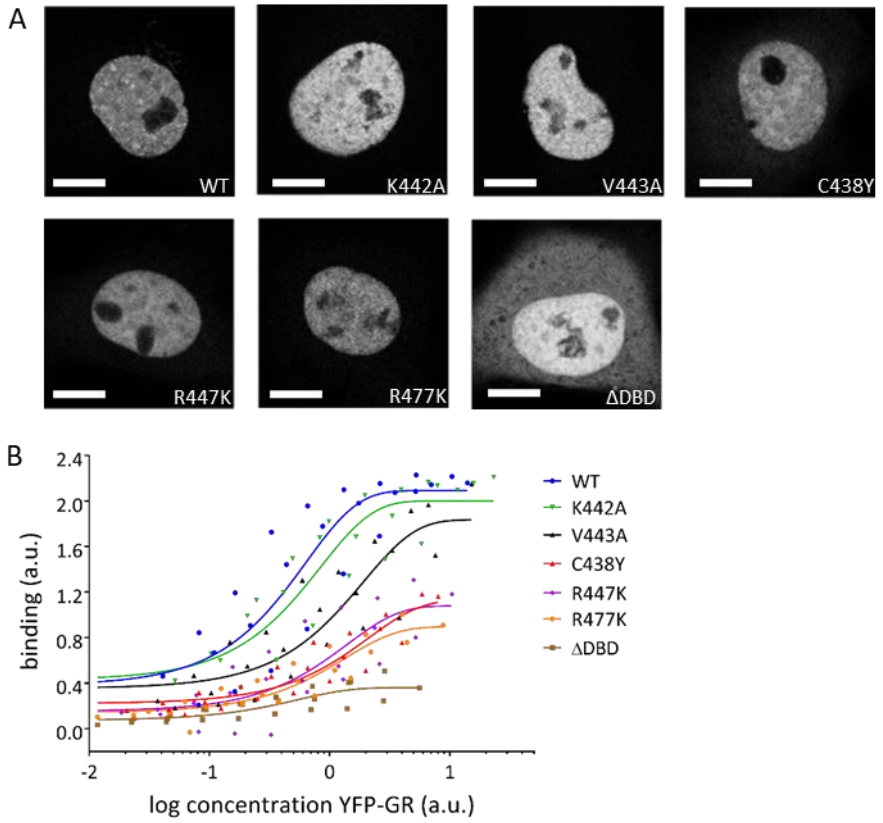

Supplemental figure 2. DNA-binding assay**.** (A) Representative confocal microscopy images of COS-1 cells expressing YFP-GR (WT or mutant). Two hours post activation with ligand (FP, 5 nM), all YFP-GRs showed nuclear translocation. The partial translocation of the ΔDBD mutant has been described previously (Schaaf and Cidlowski, 2003). (B) Nuclear extracts were taken from COS-1 cells expressing YFP-GR (WT or mutant) activated with ligand (FP, 5 nM). Extracts were used at eight different (1:2) dilutions. GR present in these dilutions was permitted to bind to a GRE in vitro for one hour. Subsequently, the amount of bound GR was measured using an ELISA-based approach, and the binding was plotted against the GR concentration (determined based on fluorescence in nuclear extracts). Data from three individual experiments were pooled and were fit using a one-phase association equation.

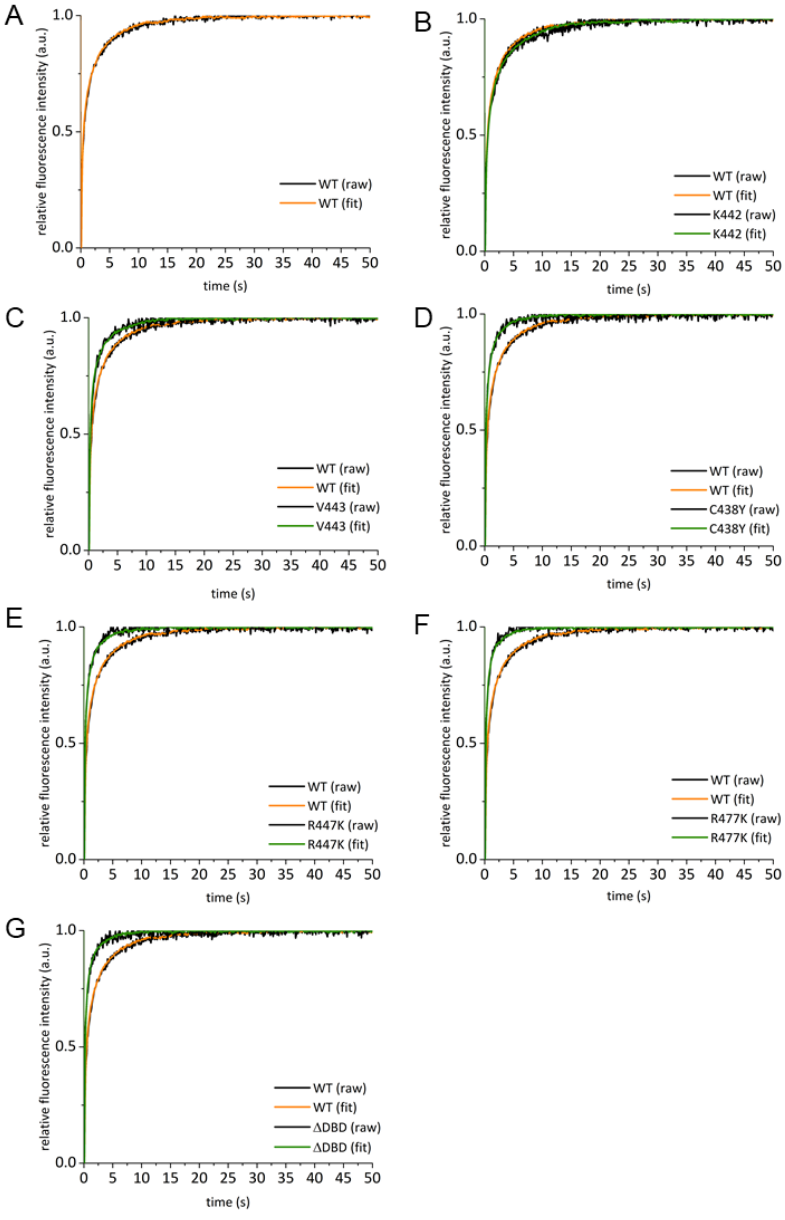

Supplemental figure 3. FRAP analysis of YFP-GR (WT and mutants). (A-F) FRAP curves comparing each mutant to WT YFP-GR individually. The bleach pulse was given at t=0 seconds. Data points from >30 cells were pooled for each condition in each experiment. The orange and green line represent the average of the top ten best fit for WT and mutant YFP-GR respectively.

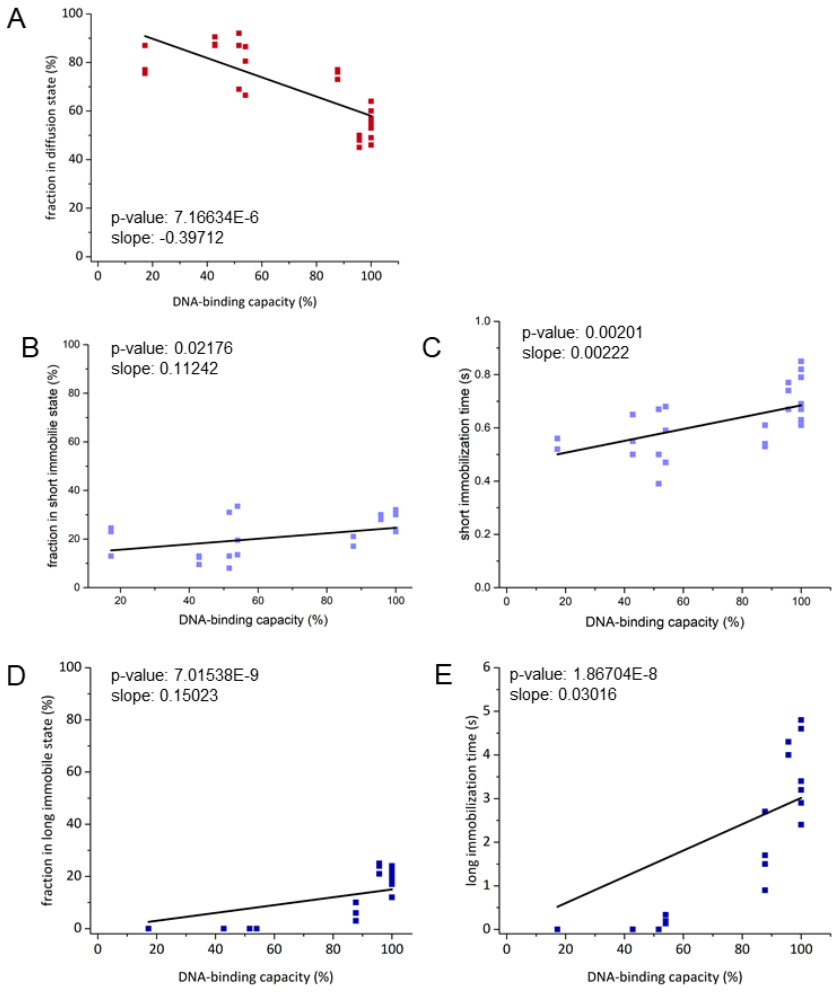

Supplemental figure 4. Correlation between the DNA-binding capacity and parameters obtained in FRAP experiments. Parameters determined in the FRAP experiments (shown in Figure 5) are plotted against DNA-binding capacity (shown in Figure 4B) for each YFP-GR construct (WT or mutant). Individual points represent data from individual experiments (>30 cells per experiment). Regression analysis was performed by ANOVA and the regression line is depicted by the black line. P-values and slopes are indicated. (A) Size of the fraction of YFP-GRs in the diffusion state plotted against the DNA-binding capacity. (B) Size of the fraction of YFP-GRs in the short immobile state plotted against the DNA-binding capacity. (C) Immobilization time of the short immobile state plotted against the DNA-binding capacity (D) size of the fraction of YFP-GRs in the long immobile state plotted against the DNA-binding capacity. (E) Immobilization time of the long immobile state plotted against the DNA-binding capacity.

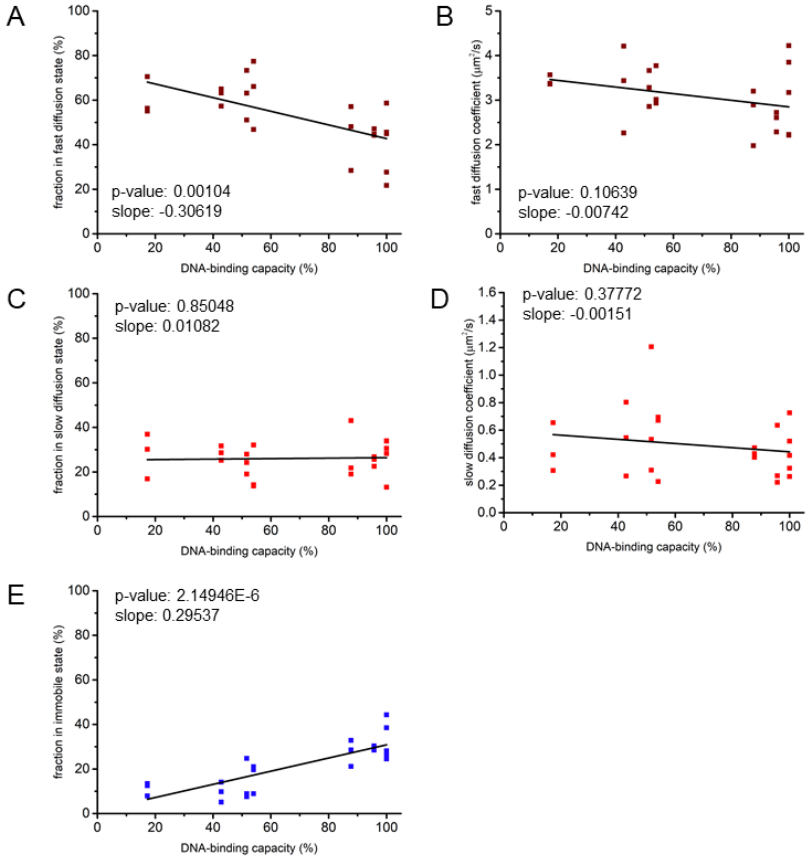

Supplemental figure 5. Correlation between the DNA-binding capacity and parameters obtained from SMM experiments. Parameters determined in the SMM experiments (shown in Figure 6) are plotted against DNA-binding capacity (shown in Figure 4B) for each YFP-GR construct (WT or mutant). Individual points represent individual experiments (>7 cells, per cell, 15 sequences of 8 frames were taken, resulting in >4000 particle localizations per experiment). Regression analysis was performed by ANOVA and the regression line is depicted by the black line. P-values and slopes are indicated. (A) Size of the fraction of YFP-GRs in the fast diffusion state plotted against the DNA-binding capacity. (B) Diffusion coefficient of the fast diffusing state plotted against the DNA-binding capacity. (C) Size of the fraction of YFP-GRs in the slow diffusion state against the DNA-binding capacity. (D) Diffusion coefficient of the slow diffusion state plotted against the DNA-binding capacity. (E) Size of the fraction of YFP-GRs in the immobile state plotted against the DNA-binding capacity.

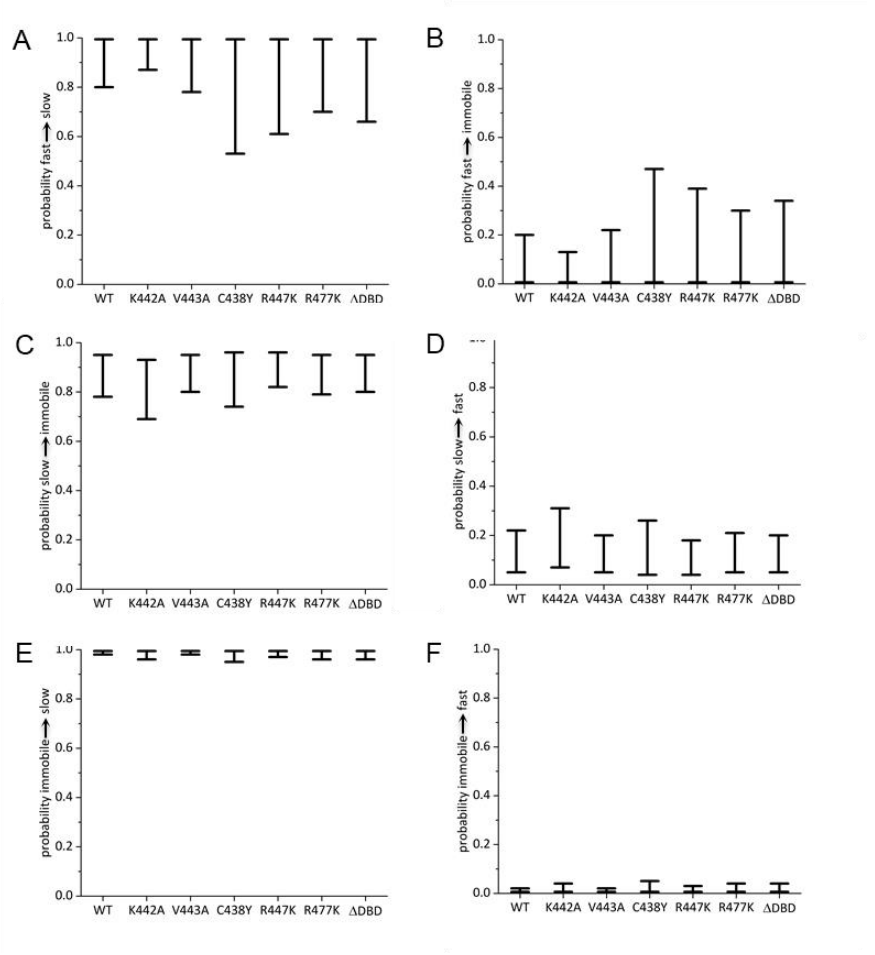

Supplemental figure 6. Probabilities of transitions between states determined using the CTMC model. All values indicated by the presented ranges are equally likely to represent the true average transition probability. Analysis based in SMM data obtained from three individual experiments (>7 cells, per cell, 15 sequences of 8 frames were taken, resulting in >4000 particle localizations per experiment) and the combined immobilization times obtained from FRAP data (three individual experiments (>30 cells per experiment). (A) Probability of the transition from the fast diffusion state to the slow diffusion state. (B) Probability of the transition from the immobile state to the fast diffusion state. (C) Probability of the transition from the slow diffusion state to the immobile state. The probabilities shown in D-F were obtained as the complementary to one of the probabilities in A-C. (D) Probability of the transition from the fast diffusion state to the immobile state. (E) Probability of the transition from the immobile state to the slow diffusion state. (F) Probability of the transition from the slow diffusion state to the fast diffusion state.

3 Depth-of-Focus Correction in Single-Molecule Data Allows Analysis of 3D Diffusion of the Glucocorticoid Receptor in the Nucleus

Rolf Harkes*, Veer I. P. Keizer*, Marcel J. M. Schaaf, Thomas Schmidt

Abstract

Single-molecule imaging of proteins in a 2D environment like membranes has been frequently used to extract diffusive properties of multiple fractions of receptors. In a 3D environment the apparent fractions however change with observation time due to the movements of molecules out of the depth-of-field of the microscope. Here we developed a mathematical framework that allowed us to correct for the change in fraction size due to the limited detection volume in 3D single-molecule imaging. We applied our findings on the mobility of activated glucocorticoid receptors in the cell nucleus, and found a freely diffusing fraction of 0.49±0.02. Our analysis further showed that interchange between this mobile fraction and an immobile fraction does not occur on time scales shorter than 150 ms.

PlosOne, 2015

*Authors contributed equally

3.1 INTRODUCTION

Since the initial camera-based observation of the diffusion of individual molecules in artificial membranes (1), single-molecule imaging technology has yielded a plethora of novel insights into the behavior of proteins and other membrane constituents *in vitro* (2–4), in live cells (5–11) and *in vivo* (12). Single-molecule microscopy has been of great importance to quantify the diffusive properties of membrane constituents. Diffusive properties consequently report faithfully about the local structural properties of the membrane, the activation state of signaling pathways (13), transport of membrane components (14), or cellular regulation processes (15,16). For a homogeneous system in equilibrium, one would predict that the ensemble-averaged mobility is hence governed by multiple populations, each reflecting a distinct molecular state of its components. Indeed, experimental verifications of this prediction have ubiquitously been found. Whether particle-averaged mean-squared displacement analysis (17), molecular step-width distributions (18) or molecular squared-displacement distributions (19) were analyzed, multiple populations have always been found in the analysis of receptor mobility in cells.

Given that single-molecule imaging permits to follow processes in time, there have been many attempts to find transitions between states i.e. transitions in diffusive behavior. Those should show up as change in the fraction size of different mobility when changing the time of observation. Using gold (14) or quantum-dot labeling (20) of individual components, or by labeling larger structure like liposomes (21) long time scales could be covered and switching behavior has been observed. Spurred by the success of single-molecule imaging in membrane biology and biophysics, in recent years the technology has been further developed to permit single-molecule observations of proteins in the 3D environment inside live eukaryotic cells (18,22,23). In those experiments individual proteins were imaged over time, their position analyzed in 3D to sub-wavelength accuracy (24), and subsequently the mobility analyzed by step-length analysis. Similar to the membrane constituents, mobility of cytosolic proteins appeared inhomogeneous and fractions of different mobility were identified. Various research groups (18,22,23) realized that, unlike when imaging on the 2D membrane surface,

the apparent fraction size of the various components depends on observation time. This is due to movements of molecules out of the depth-of-field of the observation volume: fast molecules will disappear faster compared to slow molecules (figure 1). Given typical values of 1 µm for the depth-of-field of both wide-field (18,23) or selective-plane (22) illumination and typical diffusion constants of cytosolic proteins of 10 $\mu m^2/s$, the residency time of a molecule within the observation volumes reduces to less than 50 ms. Hence, in those earlier reports fraction sizes for short time-lags of 6.5 ms and 20 ms, respectively, were reported to avoid any 3D artifacts (18,22,23).

Here we present a mathematical framework that can correct for the change in fraction size due to the limited detection volume in 3D single-molecule imaging. We applied our findings to data on the mobility of activated glucocorticoid receptors (GR) in the nucleus of monkey kidney (COS-1) cells. Our analysis showed that fraction sizes remain constant in the time-lag range from 6.5 ms to 150 ms, thus showing that switching between fractions occurs on longer time scales.

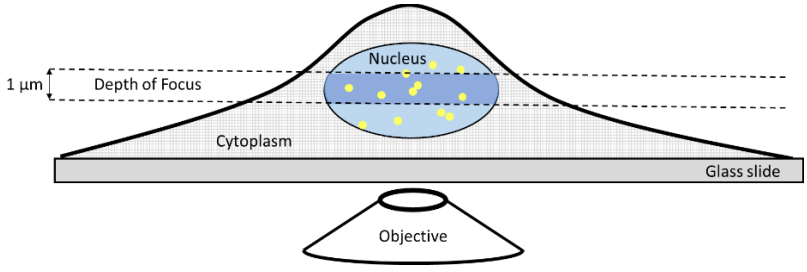

Figure 1. Imaging of diffusing fluorophores inside the nucleus. Since the depth of focus (DOF = 750 nm) is shallow, molecules can diffuse in and out of the observation volume. This will deplete the relative contribution of the fast diffusing fraction to the analysis.

3.2 Results

Here, we present an analytical solution for correction of fraction size in 3D diffusion with limited detection volume. Since the width of the point-spread-function (PSF) increases with increasing distance to the focal plane, the signal from an out-of-focus object will be spread out over a larger region of the

detector and the signal to noise ratio will decrease concomitantly. Therefore, the detectability of a molecule is limited to a small distance from the focus defining the depth of field (DOF). The DOF was measured to be 750 nm (figure 2). With respect to detailed mobility analysis that includes various fractions, the limited DOF will result in a bias towards the slowest fraction. Fast diffusing molecules will have a higher chance of diffusing out of the DOF than slow diffusing molecules. Therefore, they will have a smaller contribution to the cumulative distance distribution.

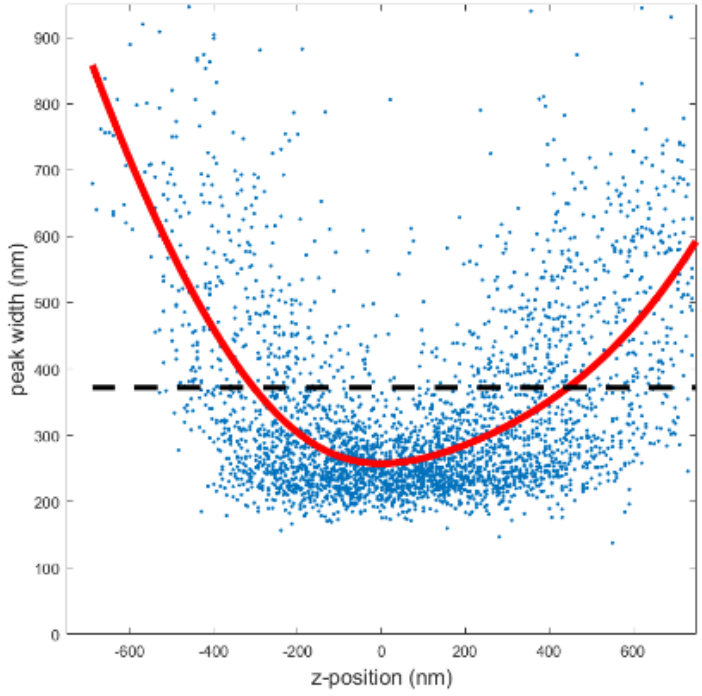

Figure 2. Calibration of the depth of field (DOF). eYFP was coated on a glass slide and the objective was moved by a piezo scanner. The resulting peak-widths were fitted as previously described [25]. The data were subsequently fit to equation 1 yielding the signal width at focus, σ 0 = 263 nm and the DOF = 750 nm. All data characterized by a width larger than $\sqrt{2}$ × 263 nm = 372 nm (dashed line) were discarded from further analysis.

In what follows we derive an analytical solution for a system that consist of two fractions of diffusing objects characterized by diffusion constants D_1 and

D_2, and fractions α and 1-α, respectively. The description can easily be expanded to include more fractions. For a molecule that is localized at axial position $z_0$the probability density for its axial location z after a time t, with a diffusion constant of D is given by:

$$pdf(z, z_0, D, t) = \frac{1}{\sqrt{4\pi D t}} e^{-\frac{(z-z_0)^2}{4Dt}} \quad \text{Eq. 1}$$

Hence, the probability to stay within the DOF of length L is given by:

$$\int_0^L \frac{1}{\sqrt{4*\pi*D*t}} e^{-\frac{(z-z_0)^2}{4Dt}} dz = \frac{1}{2}\left(erf\left(\frac{z_0}{\sqrt{4*D*t}}\right) + erf\left(\frac{L-z_0}{\sqrt{4*D*t}}\right)\right) \quad \text{Eq. 2}$$

With erf being the error function. Further integration over the start position z_0 from 0 to L results in the average probability to stay within the DOF:

$$P(L, D, t) = \text{erf}\left(\frac{L}{\sqrt{4*D*t}}\right) + \frac{\sqrt{4*D*t}}{L\sqrt{\pi}}\left(e^{-\frac{L^2}{4*D*t}} - 1\right) \quad \text{Eq. 3}$$

Which finally leads to:

$$P = erf(f) + \frac{1}{f\sqrt{\pi}}\left(e^{-f^2} - 1\right), f = \frac{L}{\sqrt{4*D*t}} \quad \text{Eq. 4}$$

Equation 4 describes the probability for a molecule that started inside the DOF to still reside within DOF after time t. Figure 3 shows the functional form for a realistic DOF of 750 nm and imaging time from 6.4 to 100 ms. The probability strongly depends on D, reducing even for short imaging times of 6.4 ms from P(0.1 µm^2/s) = 0.96 to P(2 µm^2/s) = 0.83, the range of diffusion constants typically reported. Following equation 4 this effect becomes even more pronounced for longer imaging times.

In what follows we describe how equation 4 is used to calculate the actual fraction size from imaging data in the case of multi-modal inhomogeneous diffusion data. By PICS analysis D_i, and the apparent fraction size, a_i, are obtained. Together with equation 6 the real fraction sizes, β_i, are obtained:

$$\beta_i = \frac{x_i}{\sum_i x_i}, x_i = \alpha_i P_i \quad \text{Eq. 5}$$

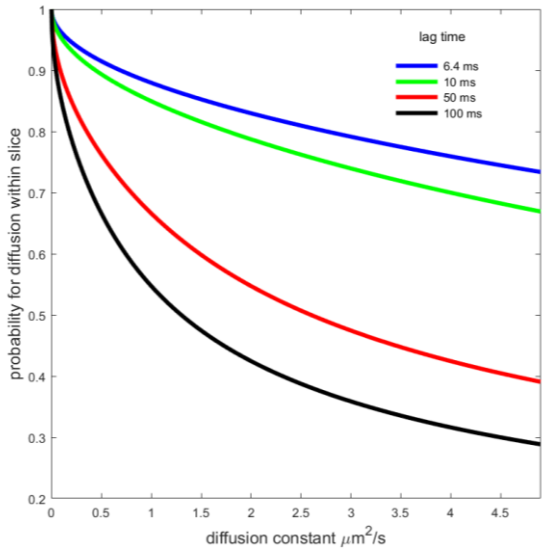

Figure 3. Result of equation 4 for DOF = 750 nm and four different time lags, t. For a diffusion constant of D = 2 µm²/s the probability to reside inside the DOF after t = 10 ms is 0.79, whereas for D = 0.1 mm²/s the probability is 0.97.

As required, both real and apparent fraction sizes are normalized quantities . For a two-component system equation 5 simplifies to:

$$\beta = \frac{\alpha P_2}{(1-\alpha)P_1 + \alpha P_2} \qquad \text{Eq. 6}$$

Where β refers to the faction with diffusion constant D_2, and 1-β the fraction with diffusion constant D_1.

Subsequently, we validated the correction by simulations. To prove the correction method Monte-Carlo simulations were performed. 3000 molecules were split in two equal fractions, β = 1-β = 0.5. The fractions were characterized by diffusion constants of D_1 = 2 pix²/frame and D_2 = 0.05 pix²/frame, respectively. Those values were chosen based on values typically found for diffusion of proteins in mammalian cells, and in particular are equivalent to the values for the bound and unbound fraction of the glucocorticoid receptor in the nucleus (2 and 0.5 µm²/s) reported earlier [23]. The objects used in the simulation were free to diffuse for 100 frames in a

cube of 100×100×100 pixels. Circular boundary conditions were applied. In order to set a DOF, only molecules within a slice of 5 pixel width (i.e. 1 µm) at the center of the cube were considered.

Particle image correlation spectroscopy (PICS) utilizes the distance distribution of the diffusing particles. To analyze the simulation the distances originating from fast diffusing objects were summed and divided by the total number of distances found. The observed fractions were extracted for time lags of 1 to 10 frames. Figure 4 shows the result of this analysis (blue data). The apparent fraction size of the fast fraction decreased from 0.46 ± 0.01 at the first time lag to 0.36 ± 0.01 for the tenth time lag. Subsequently, equation 6 was used to correct the data and calculate the real fraction size. Figure 4, shows that our analysis faithfully follows the prediction and the real fraction size remains constant at β = 0.500 ± 0.007 over the whole range of time lags (green data).

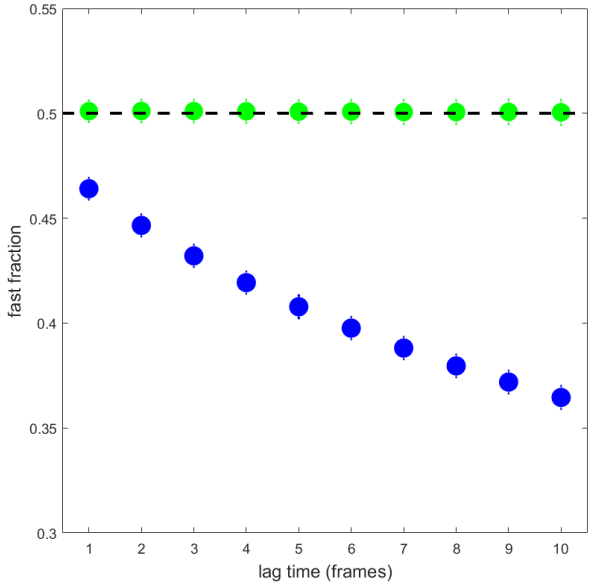

Figure 4. Simulation result that shows depletion of the fast fraction for increasing time lags. The time lag is given by the number of frames between detections. In blue the uncorrected result, in green the result after correction with equation 6.

Next, the correction was validated using experimental data. To further prove our correction method we applied the model for the correction of experimentally acquired life-cell data. The diffusion of the glucocorticoid receptor (GR) in live cells is a well-documented example for mobility of multiple fractions in a 3D environment. The GR is a member of the steroid receptor family (25–27). It mediates the effects of natural as well as synthetic glucocorticoids like dexamethasone and prednisolone, which are drugs known for their anti-inflammatory activity that is beneficial to treat diseases like asthma and rheumatoid arthrosis (25). Upon activation by glucocorticoids the receptor translocates from the cytoplasm to the nucleus. There it acts as a transcription factor. It binds to specific target sequences in the DNA to activate gene transcription. The targeted search mechanism along DNA that activate or repress gene activation by hormone receptors like the GR has long been studied in theory and experiment (28). The GR displays long immobilization times (2.3 s). The immobilized fraction probably reflects receptors bound to DNA in order to activate transcription. In addition, the GR is found to also have short immobilization times (0.7 s) (29). Most likely the short immobilization times represents a search mechanism that includes non-specific DNA binding (27). Finally, approximately half of the GR population shows fast free 3D diffusion (29).

Here we followed the wide-field single-molecule imaging strategy of Groeneweg et al. (29) to analyze the diffusion properties of activated GR and extended our analysis up to 150 ms time-lags. Obviously, our current approach does not discriminate between the short (0.7 s) and long (2.3 s) immobilization times of the receptor due to the short time scale of the experiments. Hence, only two fractions were distinguished, an immobile and a freely diffusing fraction.

Below briefly stated are the steps taken to obtain data on GR mobility, which are also depicted in figure 5. COS-1 cells were transfected with a plasmid encoding a YFP-labeled version of the GR. The functionality of the plasmid has been tested previously (29). Cells were stimulated with 1 µM of dexamethasone which leads to efficient activation and translocation of the GR to the nucleus. Subsequently, individual YFP-GRs were followed using

single-molecule microscopy in which a mid-slice of 750 nm thickness of the nucleus was imaged (figure 5A; see the DOF subsection in materials & methods). Individual GRs appeared as diffraction-limited images of a signal of 203 ± 90 counts when illuminated for 3 ms at an intensity of 2 kW/cm^2 of 514 nm light (figure 5B). This signal allowed us to track the receptors at a lateral accuracy of 34 nm. The axial position was lost as the camera imaged the 2D projection of the 3D slice in the nucleus.

Subsequently, PICS analysis was used to analyze the mobility of the GR (figure 5C). In PICS the cumulative squared-distance distributions (cdf) in subsequent frames is calculated from position data (figure 5D). The drop of the cdf at short squared-distances reflects the mobility of the molecules [26]. For diffusion the drop follows an exponential (19). As has been reported by us earlier (29), the drop is faithfully described by a bi-exponential, which reflects the bi-modal behavior of the receptor: a freely diffusing receptor and a bound receptor. PICS analysis was performed for time lags between 6.25 and 150 ms. For each time lag the diffusion constant and apparent fraction size of the two components was determined. The diffusion constants were found to be 0.67 ± 0.1 and 0.043 ± 0.004 μm^2/s for the fast and immobile fraction, respectively. Our data are in excellent agreement to our earlier findings (29), and the prediction for a free diffusion process. It should be noted that the immobile fraction found in single-molecule experiments consist of two sub-fractions which can be distinguished only at time-lags beyond 1 s as accessible by fluorescence recovery after photobleaching (FRAP) experiments. In FRAP it was found that those two fractions reflect two binding modes of the receptor to DNA, are equal in size, and are characterized by immobilization times of 0.7 and 2.3s, respectively.

As previously observed the apparent fraction of the fast fraction α dropped from 0.46 ± 0.02 at 6.5 ms to 0.37 ± 0.02 at 150 ms (figure 6, blue data). After correction to the real fraction size, as given by equation 8, it is obvious that the size of the two fractions does not change in the time frame between 6.5 and 150 ms (figure 6, green data). The real fraction size is constant and amounts to β = 0.49 ± 0.02.

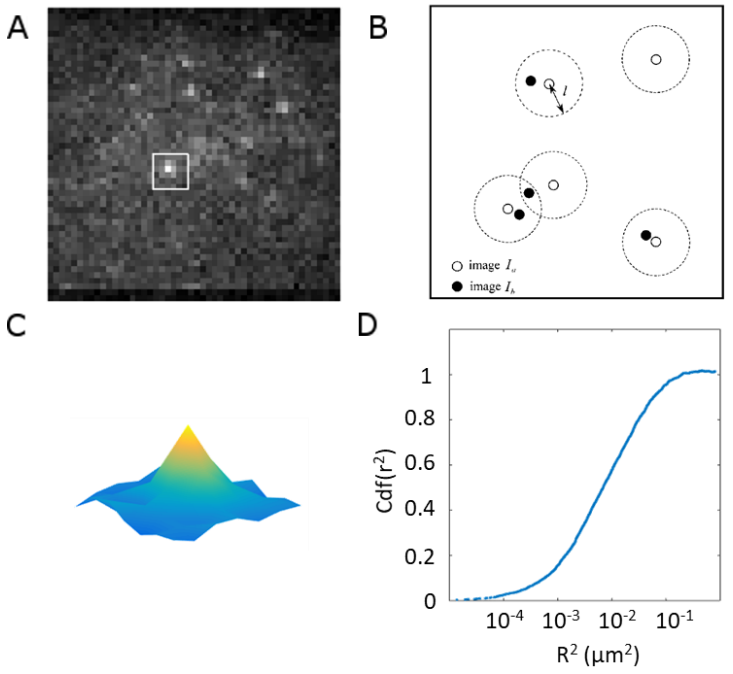

Figure 5. Single-molecule imaging and PICS analysis. A. Signal of individual eYFP-GR molecules on an emCCD camera. B. The signal of an individual molecule is fitted to a Gaussian yielding the position, the width and the strength of the signal. C. Distance calculation between molecules in subsequent frames. D. Cumulative distribution function (cdf) of distances of molecules in subsequent frames correlated by diffusion.

Even though the different mobility modes for various transcription factors have been repeatedly reported, it has remained challenging to address the timescales on which switching between the modes occurs (22,23,29–32). The observed drop in fraction size in the uncorrected data could have been misinterpreted as an indication of switching behavior. However, since in the corrected data the fraction size does not change with increasing time lag, we conclude that switching between the two modes does not occur within the time frame of 150 ms.

.

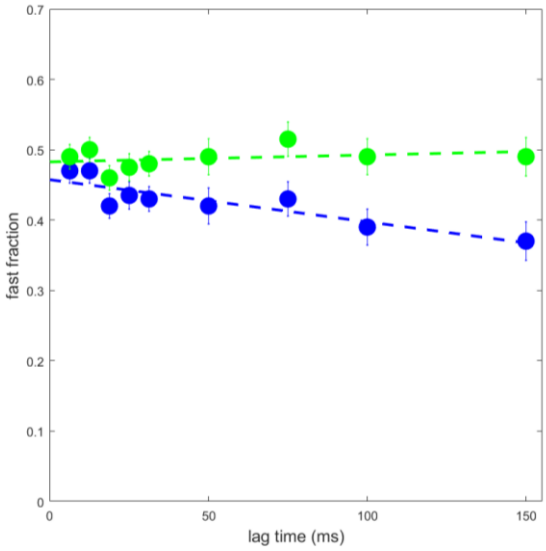

Figure 6. PICS analysis of glucocorticoid receptor at different time lags. In blue the uncorrected result. A decrease of the fast fraction is observed. In green the result corrected by equation 8 taking into account the DOF. The fast fraction stays constant for time lags at least up to 150 ms. Dashed lines are linear fits to the data. Error-bars represent the standard deviation

3.3 Discussion

We showed that a depletion of fast mobile fractions is observed when multiple diffusive fractions are analyzed using imaging methods that have limited axial reach. We developed a mathematical framework to correct for the experimental limitations that allowed us to calculate the real fraction sizes. Results have been validated by simulation and applied to experimental data of the activated glucocorticoid receptor in the cell nucleus. These results show that the reduction of the fast fraction with time lag, observed for the uncorrected data, is faithfully rectified by using the novel correction method. The corrected data indicate that the size of the freely diffusing fraction of dexamethasone-activated glucocorticoid receptors in the cell nucleus is 0.49 ± 0.02. Since the corrected data show that this fraction size is constant for at least 150 ms we conclude that the receptor does not switch between this freely diffusing and an immobile (DNA-bound) state on this time scale. Thus, our theoretical framework not only allows the determination of correct fraction sizes, but provides information on potential time scale for exchange between various fractions.

3.4 Materials and Methods

Cell culture

To measure the diffusive properties of GR-eYFP COS-1 cells (acquired from ATCC) were cultured on coverslip glasses and transfected using X-tremeGENE (Sigma-Aldrich Chemie N.V., Zwijndrecht, Netherlands, 500 ng DNA / 10 cm^2). According to the manufacturers protocol. Three to six hours prior to measurement 1 µM dexamethasone (final concentration, Sigma-Aldrich Chemie N.V. Zwijndrecht, Netherlands) was added to the cells. Measurements were carried out at 37°C.

Single-molecule imaging

Imaging of individual GR-eYFP was performed as described earlier (23). In brief 1200, frames per cell were taken on an inverted wide-field fluorescence microscope (Axiovert 100TV, Zeiss, Breda, the Netherlands) using a 100x/1.4NA oil-immersion objective (Zeiss, Breda, the Netherlands). A region of interest of 50x50 pixels was selected (pixel size of 202 nm in the image plane). Cells were illuminated with 514 nm by a DPSL laser at an intensity of 2 kW/cm^2 (Coherent Sapphire, Coherent Europe, Utrecht, Netherlands). The exposure time was kept constant at 3 ms and the time lag between two images varied between 6.25 and 75 ms by means of an acusto-optical tunable filter (AA optoelectronics, Ede, Netherlands). 45 cells were measured with 6.25 ms time lag between frames. 20 cells were measured with 25 ms lag time between frames. 16 cells were measured with 50 ms between frames. 16 cells were measured with 75 ms between frames.

The fluorescence signal from individual eYFP molecules was captured on an emCCD (Princeton Instruments, Trenton, NJ) using a combination of filters (DCLP530, HQ570/80 (Chroma Technology, Brattleboro, VT) and OG530-3 (Schott, Mainz, Germany). In order to obtain short acquisition times between frames of 6.25 ms the camera was run in kinetics-mode that permitted to capture eight consecutive frames on the camera chip before being digitized. Subsequently, signals were fitted with a two-dimensional Gaussian using a custom algorithm in Matlab (33). The position of the molecules was obtained from the fitting parameters to an average accuracy of 34 ± 9 nm. The 2D

distance between localizations could therefore be obtained with an accuracy of 68 nm.

PARTICLE IMAGE CORRELATION SPECTROSCOPY (PICS) ANALYSIS

At high densities a tracking algorithm mixes trajectories. The previously described method of particle image-correlation spectroscopy (PICS) circumvents this problem and is often used to analyze membrane diffusion (34). In PICS the cumulative distribution function (cdf) of squared distances between frames separated at a given time-lag is calculated from the position data. The drop of the cdf at short distances reflects the mobility of molecules (34). For a mobility characterized by diffusion the drop follows an exponential [19]. As has been reported earlier by us (29), the drop is faithfully described by a bi-exponential, which reflects the bi-modal behavior of the receptor: a freely diffusing receptor and an immobile, bound receptor. For each measurement, multiple time-lags are obtained by correlating not only subsequent frames but also further frames. However, due to photo bleaching the gap between frames can- not be increased indefinitely. Hence, the 6.25 ms dataset was analyzed up to five steps (6.25–31.25 ms), the 25 ms dataset was analyzed up to 4 steps (25–100 ms), the 50 and 75 ms datasets were analyzed up to 2 steps (50–150 ms).

DEPTH OF FIELD CALIBRATION

The depth of field (DOF) is defined by the axial offset of a point-object from the focal plane at which the width is increased by a factor $\sqrt{2}$.

$$\sigma(z) = \sigma_0\sqrt{1 + (\frac{z}{DOF})^2} \qquad \text{Eq. 7}$$

Equation 7 shows how the width, σ, of the PSF changes with the axial distance z from the focal plane. σ_0 is the width at the focal plane. Combining Equation 7 with the expression for the width at focus one obtains an equation for DOF, which only includes σ_0 and the wavelength of light, λ (35):

$$DOF = 2\,\frac{\pi * \sigma_0^2}{\lambda} \qquad \text{Eq. 8}$$

To experimentally obtain the DOF, eYFP molecules were coated on a glass slide. The sample was imaged for different axial positions of the objective by means of a piezo-actuator (PiFoc, PI). The fluorescent signal of single eYFP molecules was subsequently fitted (1). From the fit, the peak-width was obtained. The relation between axial position and peak-width was subsequently fitted as given by equation 7 (33). From this experiment the width at focus of σ_0 = 263 nm and the DOF = 750 nm, as defined by the axial position at which the width increases by $\sqrt{2}$ was determined (figure 2). The experimentally determined DOF is in agreement with that predicted from equation 8 of 790 nm, given the experimental value for σ_0 and the emission wavelength of eYFP (550 nm). In all further analysis localizations originating from fluorescent signal of width larger than $\sqrt{2} \times 263$ nm = 372 nm were discarded.

REFERENCES

1. Schmidt T, Schütz GJ, Baumgartner W, Gruber HJ, Schindler H. Imaging of single molecule diffusion. Proc Natl Acad Sci U S A. 1996;93(7):2926–9.

2. Funatsu T, Harada Y, Tokunaga M, Saito K, Yanagida T. Imaging of single fluorescent molecules and individual ATP turnovers by single myosin molecules in aqueous solution. Nature. 1995;

3. Wennmalm S, Edman L, Rigler R. Conformational fluctuations in single DNA molecules. Proc Natl Acad Sci U S A. 1997;

4. Lu HP. Single-Molecule Enzymatic Dynamics. Science (80-). 1998;

5. Lill Y, Martinez KL, Lill MA, Meyer BH, Vogel H, Hecht B. Kinetics of the initial steps of G protein-coupled receptor-mediated cellular signaling revealed by single-molecule imaging. ChemPhysChem. 2005;

6. Schütz GJ, Kada G, Pastushenko VP, Schindler H, Ahmed S, Brown D, et al. Properties of lipid microdomains in a muscle cell membrane visualized by single molecule microscopy. EMBO J. 2000;

7. Sako Y, Minoghchi S, Yanagida T. Single-molecule imaging of EGFR signalling on the surface of living cells. Nat Cell Biol. 2000;

8. Lenne PF, Wawrezinieck L, Conchonaud F, Wurtz O, Boned A, Guo XJ, et al. Dynamic molecular confinement in the plasma membrane by microdomains and the cytoskeleton meshwork. EMBO J. 2006;

9. Courty S, Luccardini C, Bellaiche Y, Cappello G, Dahan M. Tracking individual kinesin motors in living cells using single quantum-dot imaging. Nano Lett. 2006;

10. Giannone G, Hosy E, Levet F, Constals A, Schulze K, Sobolevsky AI, et al. Dynamic superresolution imaging of endogenous proteins on living cells at ultra-high density. Biophys J. 2010;

11. Pinaud F, Michalet X, Iyer G, Margeat E, Moore HP, Weiss S. Dynamic partitioning of a glycosyl-phosphatidylinositol-anchored protein in glycosphingolipid-rich microdomains imaged by single-quantum dot tracking. Traffic. 2009;

12. Schaaf MJM, Koopmans WJA, Meckel T, Van Noort J, Snaar-Jagalska BE, Schmidt TS, et al. Single-molecule microscopy reveals membrane microdomain organization of cells in a living vertebrate. Biophys J. 2009;

13. Lommerse PHM. Single-molecule diffusion measurements of H-Ras at the plasma membrane of live cells reveal microdomain localization upon activation. J Cell Sci. 2005;

14. Kusumi A, Sako Y, Yamamoto M. Confined lateral diffusion of membrane receptors as studied by single particle tracking (nanovid microscopy). Effects of calcium-

induced differentiation in cultured epithelial cells. Biophys J. 1993;

15. Ueda M, Sako Y, Tanaka T, Devreotes P, Yanagida T. Single-molecule analysis of chemotactic signaling in Dictyostelium cells. Science (80-). 2001;

16. de Keijzer S, Serge A, van Hemert F, Lommerse PHM, Lamers GEM, Spaink HP, et al. A spatially restricted increase in receptor mobility is involved in directional sensing during Dictyostelium discoideum chemotaxis. J Cell Sci. 2008;

17. Dietrich C, Yang B, Fujiwara T, Kusumi A, Jacobson K. Relationship of lipid rafts to transient confinement zones detected by single particle tracking. Biophys J. 2002;

18. Kues T, Peters R, Kubitscheck U. Visualization and tracking of single protein molecules in the cell nucleus. Biophys J. 2001;

19. Schütz GJ, Schindler H, Schmidt T. Single-molecule microscopy on model membranes reveals anomalous diffusion. Biophys J. 1997;

20. Cambi A, Lidke DS, Arndt-Jovin DJ, Figdor CG, Jovin TM. Ligand-conjugated quantum dots monitor antigen uptake and processing by dendritic cells. Nano Lett. 2007;

21. Coppola S, Estrada LC, Digman MA, Pozzi D, Cardarelli F, Gratton E, et al. Intracellular trafficking of cationic liposome–DNA complexes in living cells. Soft Matter. 2012;8(30):7919–27.

22. Gebhardt JC, Suter DM, Roy R, Zhao ZW, Chapman AR, Basu S, et al. Single-molecule imaging of transcription factor binding to DNA in live mammalian cells. Nat Methods. 2013;10(5):421–6.

23. Van Royen ME, van Cappellen WA, Geverts B, Schmidt T, Houtsmuller AB, Schaaf MJ. Androgen receptor complexes probe DNA for recognition sequences by short random interactions. J Cell Sci. 2014;127(Pt 7):1406–16.

24. Holtzer L, Meckel T, Schmidt T. Nanometric three-dimensional tracking of individual quantum dots in cells. Appl Phys Lett. 2012;

25. Biddie SC, Conway-campbell BL, Lightman SL. Dynamic regulation of glucocorticoid signalling in health and disease. Vol. 51, Rheumatology. 2012. p. 403–12.

26. Beato M, Klug J. Steroid hormone receptors: an update. Hum Reprod Updat. 2000;6(3):225–36.

27. Hager GL, McNally JG, Misteli T. Transcription Dynamics. Mol Cell. 2009;35(6):741–53.

28. McGhee JD, von Hippel PH. Theoretical aspects of DNA-protein interactions: Co-operative and non-co-operative binding of large ligands to a one-dimensional homogeneous lattice. J Mol Biol. 1974;

29. Groeneweg FL, van Royen ME, Fenz S, Keizer VI, Geverts B, Prins J, et al. Quantitation

of glucocorticoid receptor DNA-binding dynamics by single-molecule microscopy and FRAP. PLoS One. 2014;9(3):e90532.

30. Becker M, Baumann C, John S, Walker DA, Vigneron M, McNally JG, et al. Dynamic behavior of transcription factors on a natural promoter in living cells. EMBO Reports. 2002.

31. Morisaki T, Muller WG, Golob N, Mazza D, McNally JG. Single-molecule analysis of transcription factor binding at transcription sites in live cells. Nat Commun. 2014;5:4456.

32. Mazza D, Abernathy A, Golob N, Morisaki T, McNally JG. A benchmark for chromatin binding measurements in live cells. Nucleic Acids Res. 2012;40(15):e119.

33. Huang B, Wang W, Bates M, Zhuang X. Three-dimensional super-resolution imaging by stochastic optical reconstruction microscopy. Science (80-). 2008;

34. Semrau S, Schmidt T. Particle image correlation spectroscopy (PICS): retrieving nanometer-scale correlations from high-density single-molecule position data. Biophys J. 2007;92(2):613–21.

35. Demtröder W. Laser Spectroscopy. Spectroscopy. 2008.

4 DIFFERENCES IN GLUCOCORTICOID RECEPTOR AND ESTROGEN RECEPTOR INTRANUCLEAR DISTRIBUTION

Veer I.P. Keizer, Stefano Coppola, Thomas Schmidt, Marcel J.M. Schaaf

ABSTRACT

Although the clustering of transcription factors in nuclear foci in the nucleus is a frequently observed phenomenon, these foci have been described poorly thus far. Here, we have quantitatively characterized foci of the glucocorticoid receptor (GR) and the estrogen receptor (ER). These two transcription factors are closely related members of the nuclear receptor superfamily and are involved in essential processes in all eukaryotes. We compared their distribution and found that the GR clusters in fewer foci that are larger than the foci in which the ER is clustered. In contrast, the intensity of the foci, which corresponds with the number of transcription factors within a focal domain, was similar for both receptors. The ER and GR recognize different DNA binding motifs. We exploited the close homology of the two receptors in their DNA-binding-domain, to create mutants that exchanged recognition of the binding motif. Using these mutants, we found that there is no effect of targeting to specific DNA binding motifs (HRE) on the characteristics of nuclear. Therefore, we suggest that interaction with DNA through the DNA binding domain may be required for the formation of foci, but that the actual formation of receptor-specific foci depends on other receptor domains interacting with nuclear factors causing clustering of the receptor.

4.1 INTRODUCTION

In eukaryotic cells, the nucleus contains the DNA, which is organized by folding into nucleosomes and higher order structures along each chromosome. The nucleus is a highly organized organelle and contains several specific nuclear bodies, of which the nucleolus is the most evident. Proteins that are known to interact with the DNA, such as transcription factors, appear to be organized in a specific manner. Transcription factors function as regulators of gene expression. To this end, they bind to specific DNA target sites and recruit cofactors to activate or repress genes. When studying transcription factors in the nucleus of a cell, either by immunocytochemistry or expression of green fluorescent protein (GFP)-tagged proteins, it has often been noted that their distribution is not homogeneous, but that they are organized in foci within the nucleus. These foci appear to be relevant to transcription as they colocalized active transcription and inhibition of transcription by α-amanitin prevented the formation of dioxin receptor foci (1). In contrast, for another transcription factor, the glucocorticoid receptor (GR) only a partial colocalization with pre-mRNA and RNA polymerase II was found (2,3). For GR it was shown that the existence of these foci depends on DNA binding, dimerization and ligand binding (4–6). Together, these data show that although several determinants of these foci have been identified, the underlying biological mechanism and their exact function is still unclear.

In the present study, we have compared the intranuclear distribution of the GR with that of the estrogen receptor (ER). GR and ER are both steroid receptors, of which the activating ligand is a steroid hormone, and they belong to the superfamily of nuclear receptors. Interestingly, both receptors appear homogenously distributed in the absence of ligand, but form characteristic subdomains upon activation by a ligand. DNA binding of these receptors is mediated through direct interactions with the DNA of amino acids in the proximal box (p-box) of the DNA-binding-domain (DBD). Interestingly, the p-box of the ER differs from the DBD of the GR by only three amino acids, which specify the binding to their DNA target sequences, glucocorticoid-response elements (GREs) or estrogen-response elements (EREs). Previous work has shown that exchanging these three amino acids in

the ER for the corresponding amino acids in the GR, changes the binding preference of the ER to GR DNA targets (7,8). Here we have used the ER and GR as model transcription factors to study the molecular mechanisms underlying the formation of transcription factor foci in the nucleus. We have investigated the intranuclear distribution of ER and GR (GFP-tagged and by immunocytochemistry on endogenous receptors) to see if they have similar distributions in the nucleus. In addition, we have used mutations in the p-box of Gr and ER to change their specific DNA binding preference to see if specific binding to EREs or GREs is related to the appearance of nuclear foci.

Quantification of the nuclear distribution of transcription factors using images taken by fluorescence microscopy as previously been addressed by measuring the coefficient of variation (CV) (5,6). The CV is obtained by drawing the longest straight line through the image of a nucleus and measuring the variation of the fluorescence intensities along that line. When there are many foci, there is a lot of variation on this line and the CV is high. When the distribution of the transcription factor is more homogeneous, the CV value is lower. Using this method, both Schaaf et al. (5) and Presman et al. (6) show this value to be dependent on ligand binding to the GR. Although this method describes inhomogeneity well, it does not allow for the characterization of the foci themselves. Previously, thresholding methods have been utilized, but they did not allow for relevant variation in the expression levels of the protein (3,4). Here we have studied the number of foci, their size and relative fluorescence intensity for ER and GR. We use spinning disk confocal microscopy coupled with an extensive thresholding approach to identify foci. We show that the size number and fluorescence intensity of these subdomains is different for GR and ER. In addition, we have studied whether the effect of specific DNA binding can account for the differences between these receptors by exchanging the p-box between the two receptors. We show that the difference in distribution is not dependent on binding to specific DNA target sites.

4.2 RESULTS

In the present study, we have performed a quantitative study of GR and ER distributions iin the nucleus of live cells and find determinants of

inhomogeneity in their distribution. To this end, U2OS cell were stably transfected with a construct encoding either a GFP-GR or a GFP-ER fusion protein. Single clones were selected for low expression of the protein to avoid overexpression artefacts. Expression levels were comparable to or slightly higher than endogenous expression in different cell lines (supplemental figure 1). A confocal microscopy image of a representative nucleus after activation with the ligand is shown for each of the selected cell lines in figure 1 (A-F).

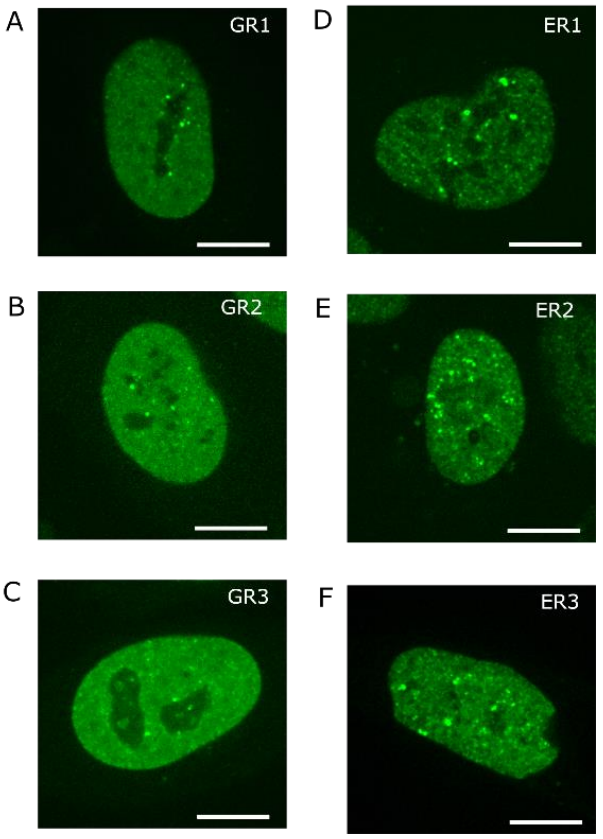

Figure 1. Nuclear distribution of GFP-GR and GFP-ER in U2OS cells (scale bars correspond with 5 µm). A-C. Representative confocal images of U2OS stably expressing GFP-GR clones 1-3. Two hours post activation with ligand (FP, 5 nM). D-F. Representative confocal images of U2OS stably expressing GFP-ER clones 1-3. Two hours post activation with ligand (estradiol, 50 nM).

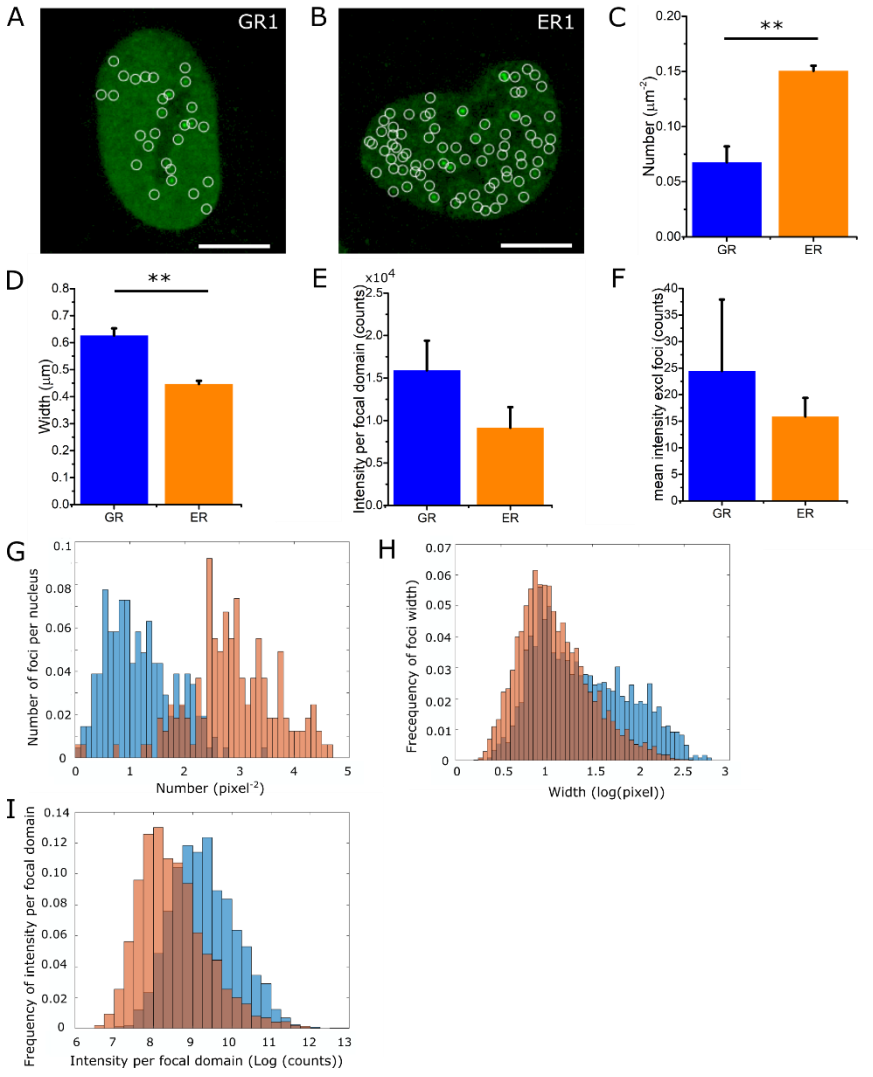

Figure 2. Analysis of GFP-GR and GFP-ER distribution in the nucleus. A-B. Representative confocal image of GFP-GR (A) and GFP-ER (B) distribution in the nucleus. Foci identified after analysis are circled in white (scale bar corresponds with 5 µm). C. Number of GFP-GR and GFP-ER foci per area. D. Width of GFP-GR and GFP-ER foci. E. Integrated intensity per focal domain for GFP-GR and GFP-ER. F. Mean intensity in the nucleus excluding foci for GFP-GR and GFP-ER. G. Histogram of number of foci per nucleus for GFP-GR (blue) and GFP-ER (orange) expressing cells. H. Histogram showing the distribution of the width of GFP-GR (blue) and GFP-ER foci (orange). I. Histogram showing the distribution of integrated intensity per focal domain of GFP-GR (blue) and GFP-ER foci (orange). N=3. Statistical significance tested by two sample t-test. ** refers to a p-value <0.01.

To characterize the nuclear distribution of both receptors in these images, an algorithm for the identification of areas with an increased concentration of receptors ('foci') was developed. In brief, after identification of the individual nuclear area through a customized watershedding procedure, a triangular thresholding was applied. A 3D Gaussian curve was then fitted in areas that remained after thresholding. This procedure was carried out for all cell lines. As an example, an image showing the foci that were identified in a cell expressing GFP-GR and GFP-ER is shown in figure 2 (A and B respectively). In U2OS cells stably expressing GFP-GR at a low expression level (GR1), the number of foci was 0.065 μm^{-2} ± 0.011 μm^{-2}. Given the average surface area a U2OS nucleus at the center of (289 μm^2 (9)), this is equivalent to an average of ~19 foci in one of our confocal microscopy images of a nucleus. In cells expressing GFP-ER (ER1), the number of foci per nuclear area was significantly higher (figure 2C). With 0.16 foci μm^{-2}, a cell expressing GFP-ER showed on average ~46 foci. In addition, the width of the foci was determined. In cells expressing GFP-GR the average width of the foci was 0.60 µm ± 0.023 µm (figure 2D). The width of the foci was found to be significantly smaller in cells expressing GFP-ER: 0.47 µm ± 0.018 µm. The integrated fluorescence intensity of the foci was not significantly different between foci in the GFP-ER and GFP-GR expressing cells (figure 2E). In addition, there was no significant difference in the average fluorescence intensity measured outside the foci (figure 2F). Subsequently, we made histograms for both GR and ER showing the distribution of the number of foci per cell, the distribution of the width and the integrated intensity of the individual focal domains. All histograms showed a unimodal distribution. This reveals that within the cell population there are no subpopulations of cells with different characteristics and that only one population of foci can be distinguished within these cells (figure 2G-I).

The different clonal cell lines generated for each receptor (GR1, GR2, GR3 and ER1, ER2 and ER3) showed differences in the expression level of GFP-GR or GFP-ER (supplemental figure 2A). However, there was no difference in the number of foci or the width of the foci between the cell lines expressing GFP-GR (supplemental figure 2B-C). This was also true for the cell lines expressing

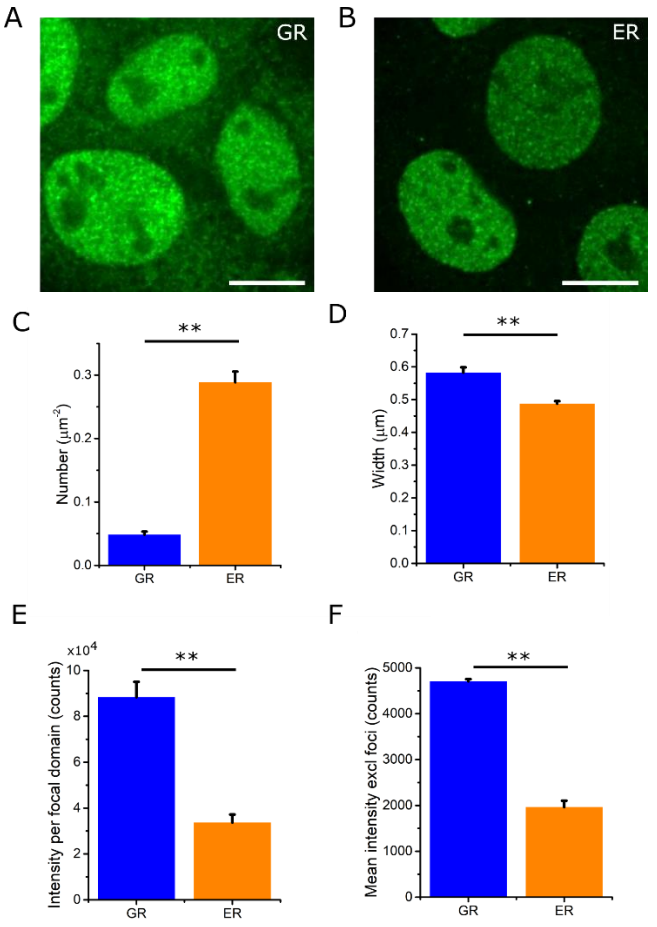

Figure 3. Characterization of endogenous glucocorticoid receptor and estrogen receptor foci in MCF7 cells. A-B. Representative confocal image of GR (A) and ER (B) distribution in the nucleus (scale bars correspond with 5 µm). Immunostaining was performed using antibodies against the relevant receptor. C. Number of GR and ER foci per area. D. Width of GR and ER foci. E. Integrated intensity per focal domain for GR and ER. F Mean intensity in the nucleus excluding foci for GR and ER. N=3. Statistical significance tested by two sample t-test. ** refers to a p-value <0.01.

GFP-ER, and it indicates that these parameters are independent of the expression levels of the receptors. Differences were found in the intensity per focal domain and the mean intensity outside the foci (supplemental figure 2D-E) which demonstrates that these parameters are dependent on the expression level of the receptors.

One GR (GR1) and one ER (ER1) cell line were chosen to study the effect of the expression level in more detail. The number of foci, their width and integrated intensity were plotted against the mean fluorescence intensity of the nucleus in which the focal domain was detected. For GFP-GR the number and width of the foci did not correlate with the mean intensity of the nucleus, verifying that these parameters were not affected by the expression level (supplemental figure 3A-B). For GFP-ER foci the width, but not the number of foci was correlated with the mean intensity of the nucleus (supplemental figure 3E-F). For both GFP-GR and GFP-ER the intensity per focal domain correlated with the mean intensity of the nucleus (supplemental figure 3C,G). This is expected as the focal domains contribute to the mean intensity of the nucleus. For GFP-GR and GFP-ER foci, the mean intensity outside the foci did not correlate with the mean intensity of nucleus (supplemental figure 3D-H), indicating that the intensity inside the focal domains was the biggest contributor to the mean intensity of the nucleus. The intensity per focal domain did not correlate with the mean intensity outside the nucleus (data not shown).

To investigate possible effects of the imaging procedure, the exposure time was varied between 10 and 100 milliseconds and the effect on the different parameters was determined. The mean intensity increased with increasing exposure time (supplemental figure 4A). The exposure time had no effect on the number of foci of either GFP-GR or GFP-ER (supplemental figure 4B), but there was an effect of exposure time on the width of GFP-ER foci and not the GFP-GR foci (figure 4C). The mean intensity inside the foci increased as the exposure time was increased for GFP-GR and GFP-ER foci, but this effect was not significant for GFP-GR (supplemental figure 4D). The intensity outside the focal domain also increased with increasing exposure time for GFP-ER foci, but this effect was not significant for GFP-ER foci (supplemental figure 4E).

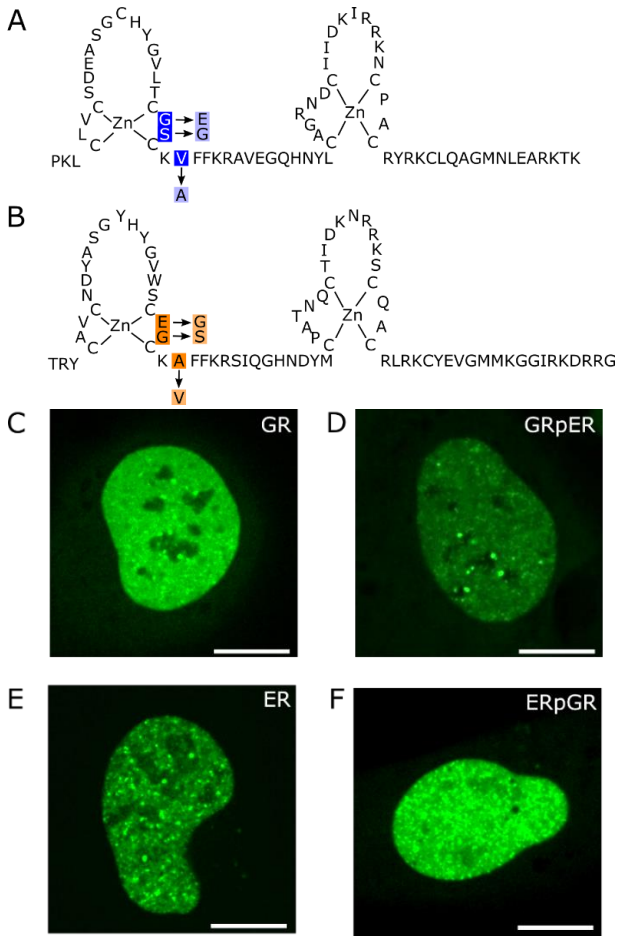

Figure 4. Analysis of WT and mutant steroid receptor distribution in the nucleus (scale bars correspond with 5 µm). A. Amino acid sequence of the GR DNA-binding-domain. The amino acids indicated in dark blue were mutated to the amino acids indicated in light blue to obtain a GR with the p-box of the ER (GRpER). B. Amino acid sequence of the ER DNA-binding-domain. The amino acids indicated in dark orange were mutated to the amino acids indicated in light orange to obtain a ER with the p-box of the GR (ERpGR). C. Representative confocal image of U2OS transiently expressing GFP-GR. Distribution of the receptor in the nucleus two hours post activation with the ligand (FP, 5 nM). D. Representative confocal image of U2OS transiently expressing GFP-GRpER. Distribution of the receptor in the nucleus two hours post activation with ligand (FP, 5 nM). E. Representative confocal image of U2OS transiently expressing GFP-ER. Distribution of the receptor in the nucleus two hours post activation with ligand (estradiol, 50 nM). F. Representative confocal image of U2OS transiently expressing GFP-ERpGR. Distribution of the receptor in the nucleus after activation with ligand (estradiol, 50 nM).

Next, we studied the distribution of endogenously expressed GR and ER. Since this requires immunostaining of fixed cells, we first investigated the effect of fixation. For this purpose, stably transfected U2OS cells were imaged prior to fixation and 30 minutes after fixation. For this purpose, MCF7 cells were fixed after activation of the receptor with the appropriate ligand, and an immunostaining was performed for either the GR or the ER. A representative confocal image of GR and ER distribution in the nucleus is shown in figure 3A and 3B respectively. The differences between ER and GR distribution as observed in U2OS cells for the number and width of the foci were also observed for the endogenous receptors in the MCF7 cells (figure 3C-D). Opposite to the results in U2OS cells, the integrated focal domain intensity and mean intensity outside the foci were higher for the GR than for the ER (figure 3E-F). Since we showed that these parameters correlate with the expression level, this is most likely due to higher expression levels. Alternatively, the efficiency of the immunostaining could be different between the GR and ER immunocytochemistry.

Subsequently, we have investigated the effect of specific DNA binding on the nuclear distribution of ER and GR. In figure 4A, a schematic of the DBD of GR is given including the three amino acids in the p-box that specify the binding of the receptor to a GRE or an ERE (indicated in dark blue). We have mutated these amino acids in the GR to correspond to those in the ER (light blue). In this manner a GR with the p-box of the ER was created, which hereafter is termed GRpER. The reciprocal, the ER with a p-box that corresponds with a GR was also constructed (ERpGR, figure 4B).

These constructs or the wildtype (WT) receptor were transiently transfected into U2OS cells. Activation of the receptor was carried out using the ligand recognized by the original receptor. Representative confocal images of cells expressing these receptors are shown in figure 4C-F. As observed previously in the stable cell lines, the wild type GFP-ER foci were significantly more numerous than the GFP-GR foci (figure 5A). However, there was no significant difference between GFP-GR and GFP-GRpER or between GFP-ER and GFP-ERpGR.

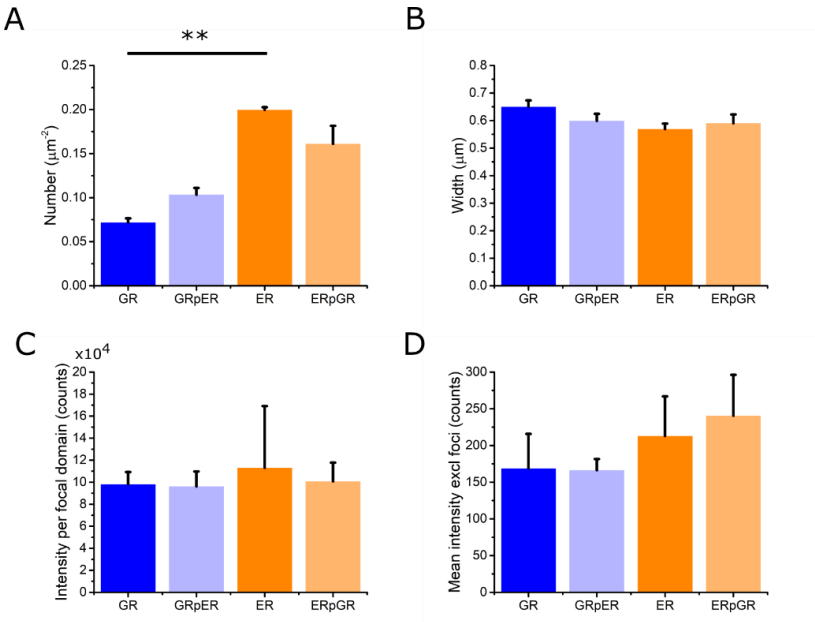

Figure 5. Analysis of WT and mutant steroid receptor distribution in the nucleus. A. Number of GFP-GR and GFP-ER foci (WT or mutated) per area. B. Width of GFP-GR and GFP-ER foci (WT or mutated). C. Integrated per focal domain for GFP-GR and GFP-ER (WT or mutated). D. Mean intensity in the nucleus excluding foci for GFP-GR and GFP-ER (WT or mutated). F. Total intensity in foci normalized for the mean intensity of the nucleus for GFP-GR and GFP-ER (WT or mutated). G. Mean intensity per nucleus for GFP-GR and GFP-ER expressing cells. N=3. Statistical significance tested by two sample t-test. ** refers to a p-value <0.01.

The significant difference between the width of the GFP-GR and GFP-ER foci, observed using the stable U2OS cell lines, was lost in this experiment in which transient transfections were used (figure 5B). There was no significant difference between the GFP-GR and GFP-GRpER or the GFP-ER and GFP-ERpGR when their width, integrated intensity per focal domain, or the mean intensity outside the foci was analyzed (figure 5C-D). These data indicate that specific DNA binding, driven by the p-box in the DBD, does not determine the formation of foci in the nucleus.

4.3 DISCUSSION

In this study, we have quantified the distribution of the ER and GR into focal domains inside the nucleus. Our data show that GR is localized in a smaller number of foci with a larger width. GR and ER foci contain a similar number of receptors. When expression levels increase, more receptors reside in the foci, but their size and number remains unchanged. The foci do not represent specific DNA binding.

The nuclear distribution of a fluorescently tagged GR and ER was measured in stably transfected U2OS cell lines. Stable cell lines with low expression, comparable to endogenous GR expression were selected. The number of foci for the ER was significantly higher than for the GR and the width of the ER foci was significantly smaller. In contrast, the total fluorescence intensity of each focal domain was not significantly different between ER and GR foci. This indicates that although the average size of the GR focal domain is bigger, there are not significantly more receptors present than in an ER focal domain. In addition, the fluorescence intensity in the nucleus outside the foci was comparable for both receptors, indicating that the number of molecules outside foci is similar for ER and GR and that the fraction of receptors that is present inside the foci is larger for ER. Therefore, we can conclude that ER is present in the nucleus in more foci than the GR and that these foci are smaller than the ER foci. Differences between two related receptors were previously also observed for another transcription factor sp1 and sp3 (10).

Several control experiments were performed to ensure the validity of the parameters we determined to describe the foci. In the experiments in which we varied the exposure time, we found that the exposure time did not correlate with the number or width of the foci for GFP-GR. For GFP-ER foci we found an effect on the number of foci. The exposure time did correlate positively with the intensity inside the focal domains. In experiments in which we studied the effect of the expression level, we found that there was no correlation between the mean fluorescence intensity of the nucleus (which is a measure for the expression level), and the number of foci or their width. Thus, with increasing expression levels no new foci appeared that previously remained undetected. However, the average fluorescence intensity of the

foci increased with increasing expression levels. This indicates that the foci contain more molecules but do not cover a larger area when more receptors are available in the nucleus. Apparently, within a restricted number of areas within the nucleus that cover a limited size, there is a seemingly unlimited number of docking sites for ER and GR.

By exchanging the three amino acids that specify binding to GREs or EREs, the GRpER mutant and ERpGR mutant were created. Interestingly, no significant effect was observed between the mutants and their original WT receptor. This strongly suggests that the distribution of receptors into nuclear foci does not directly represent binding to specific DNA binding sites. However, it was previously shown that organization of the GR into foci is dependent on the presence of a functional DBD (5). It is possible that DNA binding is a prerequisite for the formation of foci, but that the N-terminal-domain or ligand-binding-domain mediate crucial interactions with other factors that instigate the formation of foci, of which the size and number differs between receptors. Alternatively, these foci represent receptor specific degradation sites. It has been shown that the glucocorticoid receptor interacting protein 1 colocalizes with a subunit of the proteasome in discrete nuclear foci (11). Interestingly, it has also been shown that subunits of the proteasome colocalize with the receptor at the DNA and possibly assist dissociation of the receptor from the DNA (12).

In conclusion, there are large differences between ER and GR foci inside the nucleus, which are not a result of binding to different DNA target sites. Although DNA binding may be required for the formation of foci, we suggest that other factors interacting in a receptor-specific manner with domains outside the DBD determine the number and size of steroid receptor foci in the nucleus.

4.4 Material and Methods

DNA plasmids

The pEGFP-GR and pmCherry-GR plasmid were constructed by exchanging the EYFP coding sequence in the original pEYFP-GR-C1 plasmid for a EGFP or mCherry sequence using NheI and BsrGI restriction sites (original pEYFP-GR plasmid described in (13)). A pEGFP-ER plasmid with the exact same linker sequence between the GFP and ER as between the GFP and GR in pEGFP-GR was constructed through PCR of the human ERalpha coding sequence using primers containing XhoI and BamHI restriction sites. A pmCherry-ER plasmid was constructed by exchanging the EGFP sequence in the pEGFP-ER plasmid for a mCherry using the NheI and XhoI sites. The pEGFP-GRpER and the pEGFP-ERpGR plasmid were generated by site-directed mutagenesis using the QuikChange II Site-Directed Mutagenesis Kit (Agilent, Santa Clara, CA). Successful mutation was confirmed by sequence analysis.

Cell culture and generation of stable cell lines

U2OS and A549 cells were cultured in Dulbecco's Modified Eagle's Medium (DMEM, ThermoFisher Scientific, Waltman, MA) without phenol red supplemented with 10% fetal calf serum (FCS) at 37°C with 5% CO_2. Transfection was carried out using polyethylenimine (PEI) at a 3:1 ratio PEI to DNA. DNA and PEI were diluted separately in media without FCS. The PEI mixture was added to the DNA mixture and vortexed briefly. This mix was incubated at room temperature for 20 minutes. Medium was refreshed the following day. For the generation of stable cell lines, transfection was carried out using at least $1x10^6$ cells. After one day selection medium containing 700 µg/ml G418 was applied to the cells. After approximately ten days cells were seeded thinly in a 100 mm petri dish. Single clones were selected and transferred to a 12 well plate.

Western blot

Cells were induced with the relevant ligand for two hours and samples were extracted on ice using RIPA buffer. After collection of the cells by scraping, the sample was sonicated and centrifuged. The supernatant was transferred to a new tube. Laemli buffer was added and the sample was incubated for 10 minutes at 95°C. The sample was run on a 4-15% gradient precast gel (Bio-

Rad, Veenendaal, Netherlands). The gproteins were blotted onto a nitrocellulose membrane using the turbo transfer system (Bio-Rad, Veenendaal, Netherlands). Blocking was performed for one hour using 5% milk powder in PBS-Tween. A primary rabbit antibody against the GR and a primary rabbit antibody against actin were incubated overnight (1:500 and 1:1000 respectively, Abcam, Cambridge, UK). A secondary peroxidase-conjugated anti-rabbit antibody was used in combination with the Clarity Western ECL blotting substrate to visualize the protein band (Bio-Rad, Veenendaal, Netherlands). Quantification was performed using ImageJ by calculating the integrated intensity within a predetermined region around all bands.

SPINNING DISC CONFOCAL MICROSCOPY

One day prior to transfection, cells were plated in 6-well plates (Sarstedt, Etten-Leur, Netherlands), containing coverglasses (ThermoFisher Scientific, Waltman, MA). One day after transfection, cells were induced with the relevant ligand (5 nM fluticasone proprionate (FP, Sigma Aldrich, Zwijndrecht, The Netherlands) or 50 nM estradiol (Sigma Aldrich, Zwijndrecht, The Netherlands)). Three to six hours after addition of the ligand, the coverglass on which the cells had been plated was placed in a metal ring holder and 1 ml Fluobrite medium (ThermoFisher Scientific, Waltman, MA) was added. Cells were imaged at 37°C and 5% CO_2 using a spinning disk confocal microscope equipped with a 100x/1.4 NA oil-immersion objective (Carl Zeiss, Breda, Netherlands). For cells expressing GFP conjugated constructs, illumination was performed using a 488 nm argon laser at an intensity of 2.5 kW/cm^2. For cells expressing mCherry conjugated constructs, illumination was performed using a 561 nm argon laser at an intensity of 2.5 kW/cm^2. Illumination of the sample for 50 ms was controlled through an acousto-optical tunable filter (AA Opto Electronic, Orsay, France). Images were recorded on a back-illuminated CCD camera (Princeton, Instruments, Trenton, NJ) with 0.138 µm/pixel. Three individual experiments were performed in which at least each 30 cells were imaged per condition.

IMAGE ANALYSIS

To identify foci and quantify their characteristics Matlab (Mathworks, Eindhoven, the Netherlands) was utilized and a script was developed. The nucleus of each cell was identified automatically using marker-controlled watershed segmentation. In brief, foreground objects were marked through opening-by-reconstruction and closing-by-reconstruction. Regional maxima were identified and subsequently the edges were cleaned. Regions with an area smaller than 3000 pixels were excluded to avoid inclusion of artefacts present in the image. The area of each nucleus was measured and stored separately as a mask. This mask was applied to the original image. Subsequently, possible positions of individual foci were obtained by thresholding the grey scale image using the triangle method (14). This allowed for thresholding that takes into account the fluorescence intensities outside the foci since these can differ within an image and across images. At the identified positions, a Gaussian was fitted to the original image. The fitted foci were removed from the image and the process was iterated to identify foci in close proximity of each other. Foci with a relative fitting error larger than 0.3 were discarded.

REFERENCES

1. Elbi C, Misteli T, Hager GL. Recruitment of dioxin receptor to active transcription sites. Mol Biol Cell. 2002;

2. van Steensel B, Jenster G, Damm K, Brinkmann AO, van Driel R. Domains of the human androgen receptor and glucocorticoid receptor involved in binding to the nuclear matrix. J Cell Biochem. 1995;

3. van Steensel B, Brink M, van der Meulen K, van Binnendijk EP, Wansink DG, de Jong L, et al. Localization of the glucocorticoid receptor in discrete clusters in the cell nucleus. J Cell Sci. 1995;

4. Stortz M, Presman DM, Bruno L, Annibale P, Dansey M V., Burton G, et al. Mapping the Dynamics of the Glucocorticoid Receptor within the Nuclear Landscape. Sci Rep. 2017;

5. Schaaf MJ, Lewis-Tuffin LJ, Cidlowski JA. Ligand-selective targeting of the glucocorticoid receptor to nuclear subdomains is associated with decreased receptor mobility. Mol Endocrinol. 2005;19(6):1501–15.

6. Presman DM, Alvarez LD, Levi V, Eduardo S, Digman MA, Martí MA, et al. Insights on glucocorticoid receptor activity modulation through the binding of rigid steroids. PLoS One. 2010;

7. Voss TC, Schiltz RL, Sung MH, Yen PM, Stamatoyannopoulos JA, Biddie SC, et al. Dynamic exchange at regulatory elements during chromatin remodeling underlies assisted loading mechanism. Cell. 2011;

8. Mader S, Kumar V, De Verneuil H, Chambon P. Three amino acids of the oestrogen receptor are essential to its ability to distinguish an oestrogen from a glucocorticoid-responsive element. Nature. 1989;

9. Koch B, Sanchez S, Schmidt CK, Swiersy A, Jackson SP, Schmidt OG. Confinement and Deformation of Single Cells and Their Nuclei Inside Size-Adapted Microtubes. Adv Healthc Mater. 2014;

10. He S, Sun J-M, Li L, Davie JR. Differential Intranuclear Organization of Transcription Factors SP1 and SP3. Mol Biol Cell. 2005;

11. Baumann CT, Ma H, Wolford R, Reyes JC, Maruvada P, Lim C, et al. The glucocorticoid receptor interacting protein 1 (GRIP1) localizes in discrete nuclear foci that associate with ND10 bodies and are enriched in components of the 26S proteasome. Mol Endocrinol. 2001;

12. Stavreva DA, Muller WG, Hager GL, Smith CL, McNally JG. Rapid glucocorticoid receptor exchange at a promoter is coupled to transcription and regulated by chaperones and proteasomes. Mol Cell Biol. 2004;24(7):2682–97.

13. Schaaf MJ, Cidlowski JA. Molecular determinants of glucocorticoid receptor mobility

in living cells: the importance of ligand affinity. Mol Cell Biol. 2003;23(6):1922–34.

14. Zack GW, Rogers WE, Latt SA. Automatic measurement of sister chromatid exchange frequency. J Histochem Cytochem. 1977;

4.5 SUPPLEMENTAL FIGURES

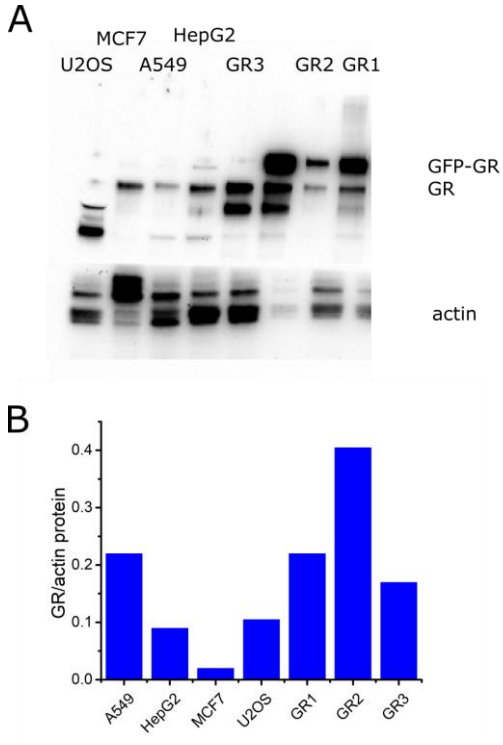

Supplemental figure 1. Expression of endogenous GR and stable expression of GFP-GR in different cell lines. Cells were immunostained using an antibody against the GR. Quantification of western blot results through optical density measurement of protein bands in the blot and normalization to actin. GR1-3 correspond with the three cell lines that stably express GFP-GR.

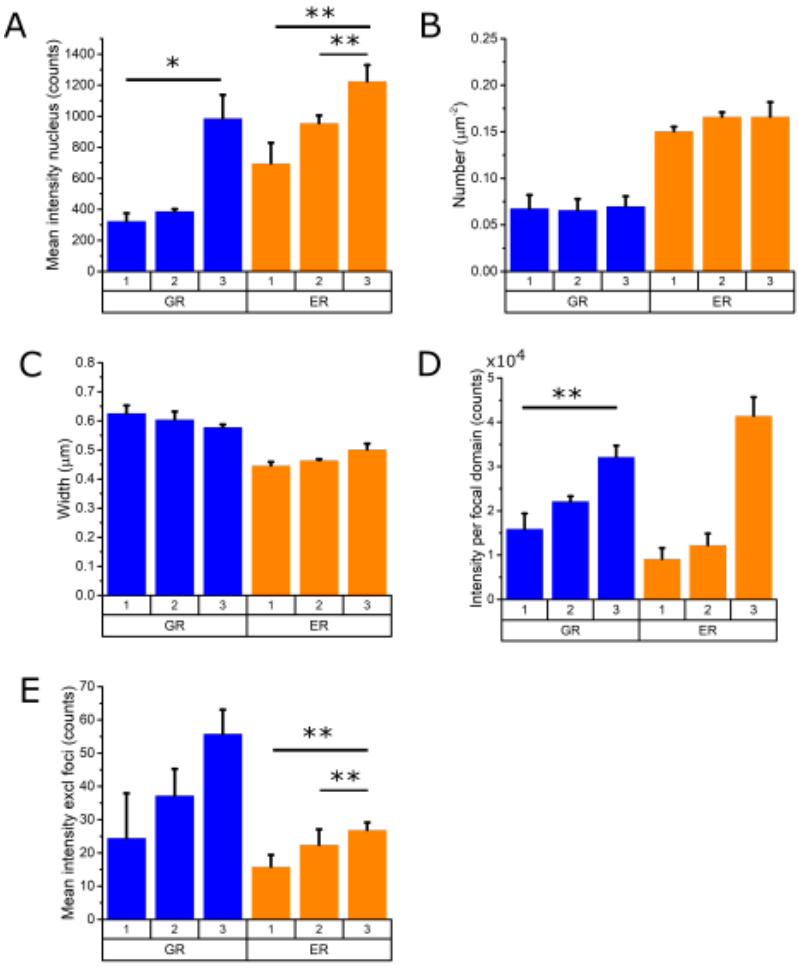

Supplemental figure 2. Homogeneity amongst single clone cell lines. A. Mean intensity per nucleus of U2OS cells expressing GFP-GR or GFP-ER in three single clone cell lines. B. Number of GFP-GR and GFP-ER foci per area in three different single clone cell lines. C. Width of GFP-GR and GFP-ER foci in three different single clone cell lines. D. Integrated intensity per focal domain of GFP-GR and GFP-ER foci in three different single clone cell lines. E. Mean intensity in the nucleus excluding GFP-GR and GFP-ER foci for three different single clone cell lines.

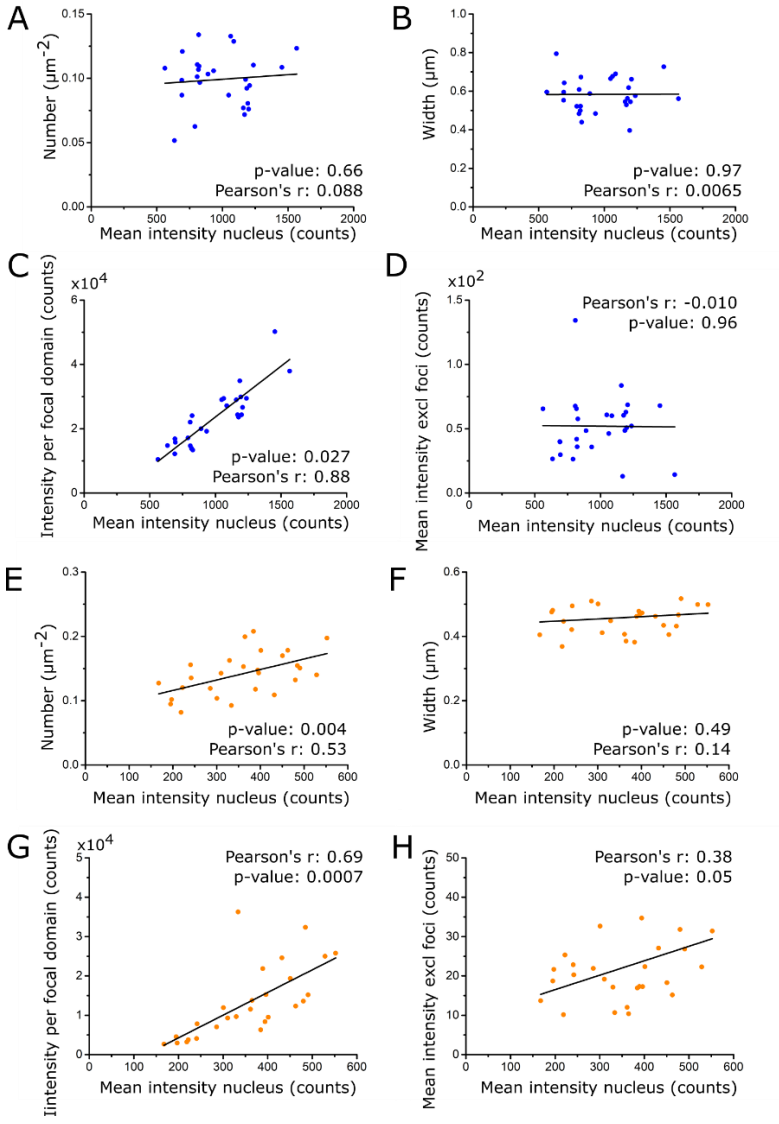

Supplemental figure 3. The effect of expression levels on different parameters. Pearson's correlation coefficient is given as a measure of correlation between the mean intensity per nucleus excluding foci and the specific parameter. No correlation was significant based on regression analysis. A. The effect of the mean intensity per nucleus excluding foci on the number of GFP-GR foci identified per area. B. The effect of the mean intensity per nucleus excluding foci on the width of GFP-GR foci. C. The effect of the mean intensity per nucleus excluding foci on integrated intensity per focal domain for GFP-GR foci. D. The effect of the mean intensity per nucleus excluding foci on the number of GFP-ER foci identified per area. E.

The effect of the mean intensity per nucleus on the width of GFP-ER foci. F. The effect of the mean intensity per nucleus excluding foci on integrated intensity per focal domain of GFP-ER foci.

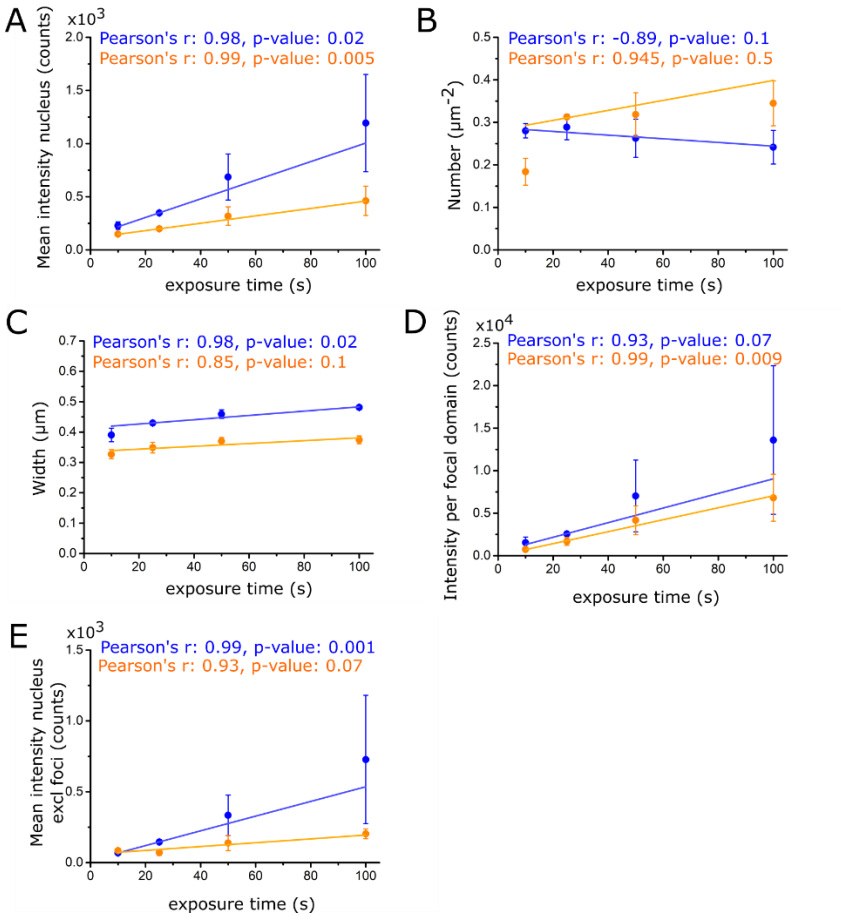

Supplemental figure 4. The effect of exposure time on different parameters for GFP-GR (blue) and GFP-ER (orange) foci. Exposure times of 10, 25, 50 and 100 ms were used. Pearson's correlation coefficient is given as a measure of correlation between the mean intensity per nucleus excluding foci and the specific parameter. N=3. Significance was calculated based on regression analysis (p-value). A. The effect of exposure time on the GFP-GR or GFP-ER foci intensity normalized for the mean intensity of the nucleus. B. The effect of exposure time on the mean intensity in the nucleus of cells expressing GFP-GR or GFP-ER. B. The effect of exposure time on the number of GFP-GR and GFP-ER foci per area. C. The effect of exposure time on the width of GFP-GR and GFP-ER foci. D. The effect of exposure time on integrated intensity per focal domain of GFP-GR and GFP-ER foci. E. The effect of exposure time on the mean intensity excluding GFP-GR or GFP-ER foci.

5 CHARACTERIZATION AND FUNCTIONALIZATION OF GOLD NANORODS IN LIVE CELLS

V.I.P. Keizer, S. Carozza, J. Capoulade, N. L. Mora, A. Boyle, D.,A. Kross, J. van Noort, M.J.M. Schaaf

ABSTRACT

GNRs are particles that are attractive for labeling of proteins in live cells. To optimize conditions for the tagging of proteins with GNRs, it is necessary to establish their behavior in cells and the effectiveness of conjugation of proteins to the nanorods. Here we have used a method to inject PEGylated GNRs in either the nucleus or cytoplasm of cultured cells. Subsequently, we have characterized their dynamic behavior inside the cells. To this end, we have used a homebuilt two-photon microscope to get the accuracy and speed required. Moreover, we have conjugated a nuclear localization signal peptide to the GNRs to show the functionality of a protein tag. We observed entry of GNRs with a nuclear localization signal into the nucleus. Their ability to enter the nucleus indicates that the GNRs are small enough to be transported into the nucleus, are located outside vesicles, and are non-toxic.

5.1 INTRODUCTION

Gold nanorods (GNRs) are nanoparticles that show great promise for a wide variety of applications in medical therapies and biological research. In photothermal therapy against cancer as well as targeted drug delivery they have shown to be effective (1,2). In addition, these particles are attractive tags to use as a label for proteins in live cells, enabling localization and tracking of these proteins. Currently, organic dyes and autofluoresecent proteins like Green Fluorescent Protein (GFP) are typically used in biolological research to label proteins, but these fluorophores generally exhibit low photostability due to bleaching or blinking, and the low amplitude of their signal prevents detection with high precision in a noisy environment like a living cell. In contrast, the plasmon resonance generated when exciting a GNR is photostable and can be observed for infinitely long times. In addition, the brightness of GNRs is up to 60x times higher than that of an average fluorophore. Gold nanoparticles can be fabricated in a number of geometries, of which the spherical or rod like geometry are the most commonly used. Compared to gold nanospheres, the rod like structure of nanorods is beneficial because the higher aspect ratio corresponds with a higher optimal excitation wavelength. This higher wavelength light causes less damage and lower levels of autofluorescent background signals in living cells. To assess the promise of GNRs as a label for proteins in live cells, characterization of their dynamic behavior in cells is essential. Free diffusion of GNRs through a cell is a prerequisite to function as an inert label for proteins, and to establish the nature of the intracellular diffusive behavior of GNRs, quantification of their dynamics is especially important. In addition, the functionality of the conjugated proteins has to be determined.

The diffusion of GNRs in live cells is largely determined by cellular uptake into vesicles, which is largely influenced by the method of delivery (3,4). Of all delivery techniques, incubation is the most commonly used technique to deliver nanoparticles to cells. Larger particles and particles with an excessive charge cannot pass the plasma membrane of a cell, but they can be taken up via endocytosis, and most GNRs that have been studied were taken up via clathrin-mediated endocytosis (5). Endocytosis of gold nanoparticles has been shown to be dependent on the size and shape of the rods. For example,

Chithrani and coworkers have found 50 nm gold nanospheres to have the highest uptake rate, whereas particles of another size or shape were taken up much less efficiently (6). In addition, uptake is largely dependent on surface charge and surface coating (7,8). Subsequent to the uptake through endocytosis, gold nanoparticles are targeted to the endosomal-lysosome pathway where they accumulate (9,10).In recent years a major emphasis has been on the coating of GNRs with peptides that facilitate endosomal escape, since the sequestration of GNRs into vesicles prevents free diffusion. Positively charged peptides, called cell penetrating peptides, have been proposed to mediate uptake via another route than endocytosis and promotes the escape from vesicles (10).

Alternatively, electroporation can be used to deliver nanoparticles to cells, and gold nanoparticles with a diameter up to 20 nm have successfully been delivered to cells by this method (11). Their intracellular fate was not investigated in this study, but it was reported that for quantum dots that they form aggregates after delivery by electroporation (4). Particles can also be delivered to cells by direc injection into the cells, either in the cytoplasm or the nucleus. Injection of nanoparticles without uptake into vesicles was shown in mammalian adherent cells (4,12). The injection of GNRs was demonstrated to be nontoxic to zebrafish embryo development (13–15). In some cells, lethality has been observed, probably due to the increase in volume and puncturing of the plasma membrane. In addition, the technique is single cell based and therefore low throughput.

To utilize GNRs to label proteins in a useful way, the conjugated protein must remain functional. In this study, the conjugation of a Nuclear Localization Signal (NLS) peptide to GNRs was assessed. This peptide sequence serves as a signal to transport a protein from the cytoplasm to the nucleus via an active transport mechanism by members of the importin family through the nuclear pore complex. Previously, localization studies of gold nanoparticles have shown passive diffusion from the cytoplasm to the nucleus of particles with a diameter up to 10 nm, but particles of 16 nm were unable to translocate to the nucleus (16). This is consistent with size of the opening of the nuclear pore complex, which allows particles between 10 and 40 nm to be

transported across the nuclear membrane. There are many types of NLS sequences, but in general they contain multiple lysine or arginine residues. These positively charged amino acids can be spaced differently according to the type of NLS sequence. With the aid of an NLS signal particles with sizes up to 40 nm in diameter have been reported to enter the nucleus of different cell types (10,17,18).

In the present study, we have used GNRs that were coated with polyethylene glycol (PEG) to reduce cytotoxicity. Diffusion of these GNRs was characterized in the cytoplasm and the nucleus. Free diffusion was observed in both milieus and led us to investigate the functionalization of these particles. The brush of PEG molecules coating the surface of the GNRs contains methylated ends that are pointing outwards. These PEG molecules can be exchanged for PEG molecules that have amino termini. These reactive groups can then be fused to linker peptides, such as sulfo-SMCC, through which many types of bonds are conceivable. An NLS peptide was conjugated to the GNRs and this NLS peptide appeared to be functional as GNRs translocated from the cytoplasm to the nucleus. This demonstrated the ability of our GNRs to be transported through the nuclear pore complex. Finally, extrusion of GNRs out of the cells was observed for GNRs in the cytoplasm, whereas the number of GNRs in the nucleus remained stable over time.

5.2 RESULTS

In order to study the behavior of GNRs in live cells, we use of GNRs with an average size of 60.5 ± 6.2 nm by 22.8 ± 4.5 nm. The size of the rods was measured using TEM images of GNRs seeded on a grid. A representative image is shown in figure 1A. To reduce cytotoxicity, GNRs were coated with a PEG layer. The UVvis-spectrum of the GNRs before and after PEGylation is shown in figure 1B. GNRs were injected in either the cytoplasm or the nucleus of live Hela cells. Cells were then imaged using a two-photon microscopy setup with a tunable wavelength laser. Using this setup homogeneous illumination of one plane was achieved by combining a diffractive optical element that creates 100 spots with a rotating mirror. A schematic of the setup is shown in figure 1C). A representative transmission

image (A) and a two-photon excitation image (B) of a cell injected in both the nucleus and cytoplasm are shown in figure 2. A z-stack encompassing the volume of the nucleus was taken for each cell and a z,y-projection is shown in figure 2C. By overlaying the transmission image (A) and two-photon image (B) GNRs could be assigned to cellular compartments. Furthermore, the position of each gold nanorod was determined by fitting the signal with a 3D Gaussian fit and the position was tracked over time, which allowed us to study the diffusion of GNRs in live cells. Traces of GNRs projected on top of the transmission image are shown in figure 2E.

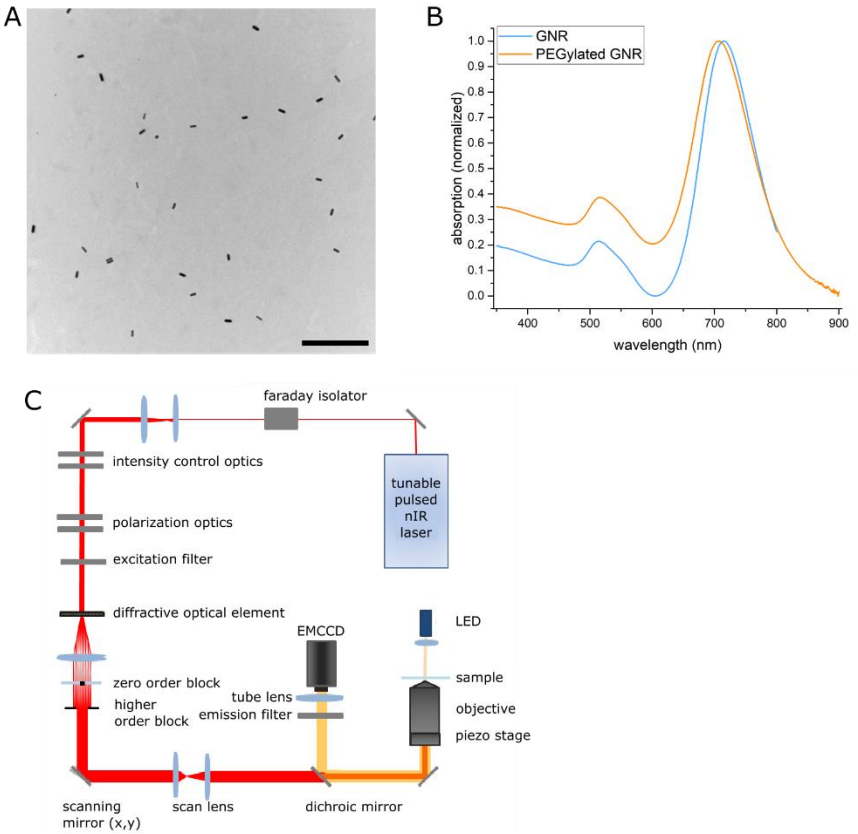

Figure 1. Details for GNRs, PEGylation of GNRs and the microscope. A. Transmission Electron Microscope (TEM, JEOL JEM 1010) image of GNRs (60.5 ± 6.2 nm by 22.8 ± 4.5 nm) on a grid. Scale bar corresponds with 500 nm. B. UVvis-spectrum of CTAB coated GNRs and PEGylated GNRs. C. Schematic representation of the two-photon microscope.

To study the characteristic behavior of GNRs in either the nucleus or the cytoplasm, we took advantage of the unique opportunity that the injection method provided to study the behavior in these two different compartments of the cell separately. Mobility of the GNRs in either compartment was categorized into immobile, confined diffusion or free diffusion. In the nucleus, 13% of the GNRs were immobile, 45% showed confined diffusion and 42% diffused freely (figure 3A). In the cytoplasm, 16% of the GNRs were immobile, 35% was confined and 49% could diffuse freely (figure 3A). The diffusion coefficient of the freely diffusing GNRs in both the cytoplasm and nucleus was around 0.01 $\mu m^2/s$ (figure 3B) and was determined based on the MSD histograms of the traces (for further details see the materials and methods section. The histograms of the MSDs are shown in Supplemental figure 3A and B). The diffusion coefficient was lower than the maximal theoretical diffusion coefficient based on FCS measurements (see Supplemental figure 1C). The confinement radius of GNRs displaying confined diffusion was 0.65 µm (figure 3C). Together these results show that almost half of the GNRs were freely diffusing in both the cytoplasm and the nucleus, and that their diffusion coefficient was lower than expected. Interestingly, no difference in the mobility of GNRs was observed between the nuclear and cytoplasmic compartment.

To assess the possibilities of conjugating GNRs with functional proteins, an NLS was attached to PEGylated GNRs using a sulfo-SMCC linker peptide. A shift in the UV-vis spectrum, shown in Supplemental figure 4A, indicated successful functionalization of the rods first with sulfo-SMCC and subsequently with the NLS peptide. The nuclear localization signal used here consisted of the following amino acid sequence: GPKKKRKVGGC (SV40 large T NLS). To demonstrate that the nuclear localization signal was functional, the NLS peptide was attached to carboxyfluorescein and injected into the cytoplasm. In Supplemental figure 3B nuclear translocation of these constructs occurs, wheeras carboxyfluorescein without an NLS is homogeneously distributed over the cell. Throughout the following experiments, the GNRs only functionalized with sulfo-SMCC were used as a control.

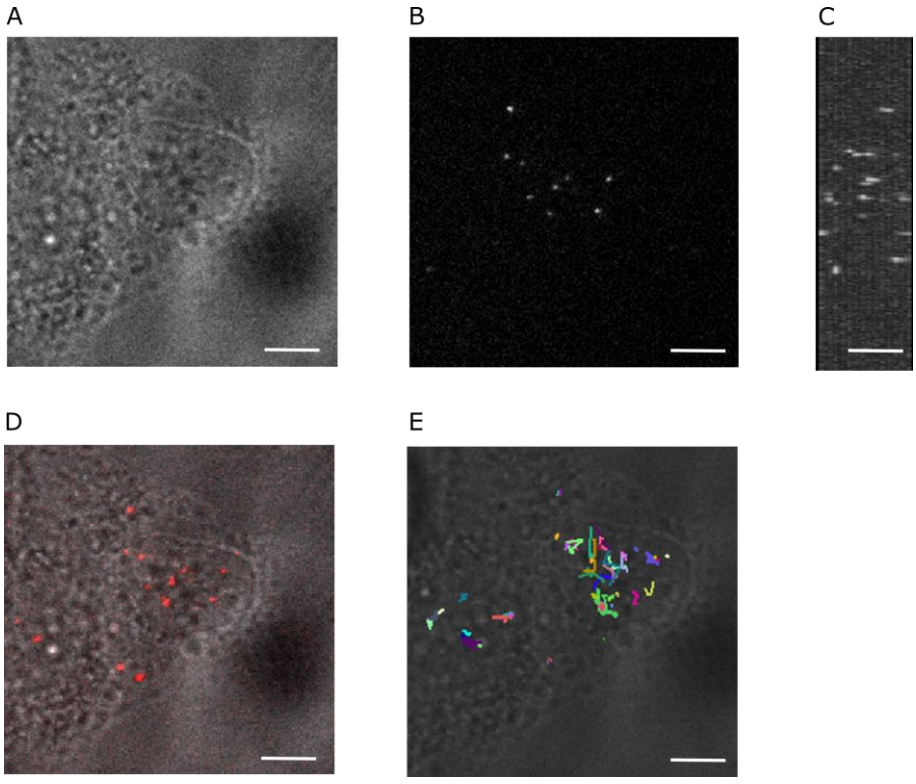

Figure 2. Image acquisition and trace reconstruction. A. Transmission image of a cell microinjected in the nucleus and cytoplasm. B. Two-photon image of a cell microinjected in the nucleus and cytoplasm (3D projection of a single z-stack). C. A z-y projection of the two-photon image of a cell microinjected in the nucleus and cytoplasm. D. An overlay of transmission image (A) and two-photon image (B). The scale bar corresponds with 5 µm. The two-photon signal is depicted in red. E. Overlay of transmission image (A) and GNR traces of cell microinjected in the nucleus and cytoplasm. Each color represents a different trace. The scale bars correspond with 10 µm in all figures, except in C.

Subsequently, NLS-GNRs were injected into live cells. Prior to injection, the nuclei of the cells were stained with Hoechst dye. Cells were imaged at three time points: 0.5, 1.5 and 24 hours post injection. Representative images of each time point are shown in figure 4 A-C. NLS-GNRs were found in the cytoplasm, around or in the nuclear membrane and in the nucleus at all time points. In contrast, control GNRs were found only in the cytoplasm and around or in the nuclear membrane (figure 4 D-F). To quantify this

observation, nuclear localization was determined by overlap with Hoechst staining in each z-stack. Each cell was compartmentalized into three compartments: the nucleus, the nuclear membrane and the cytoplasm. The number of GNRs in each compartment was quantified. On average 8% of NLS-GNRs were found in the nucleus at 0.5 hours after injection (figure 5A), and the higher than the percentage of control GNRs (0.5 %, figure 5A).

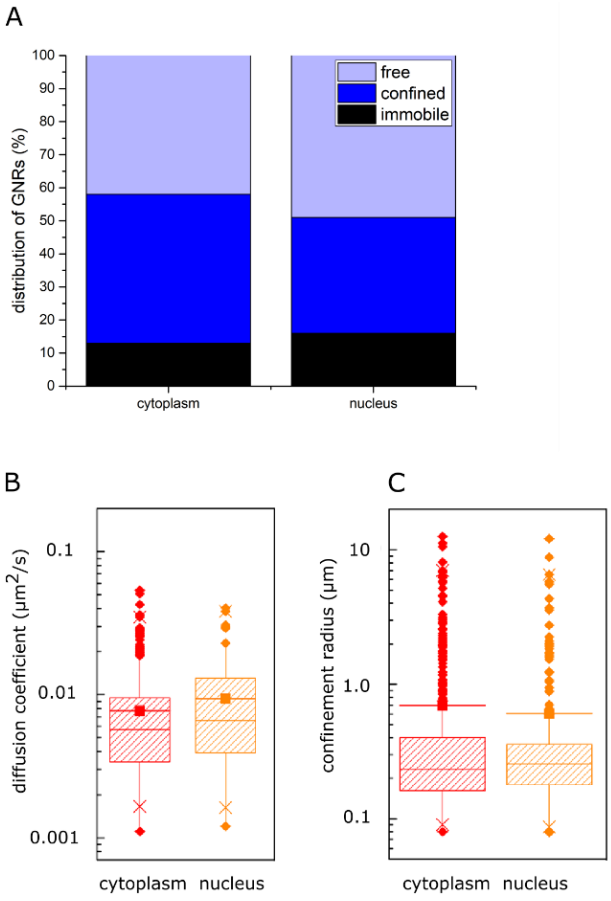

Figure 3. Mobility of GNRs in nucleus and cytoplasm. A. Distribution of GNRs according to mobility pattern (i.e. immobile, confined diffusion, free diffusion). B. Diffusion coefficient of GNRs in cytoplasm or nucleus. C. Confinement radius for GNRs in cytoplasm or nucleus.

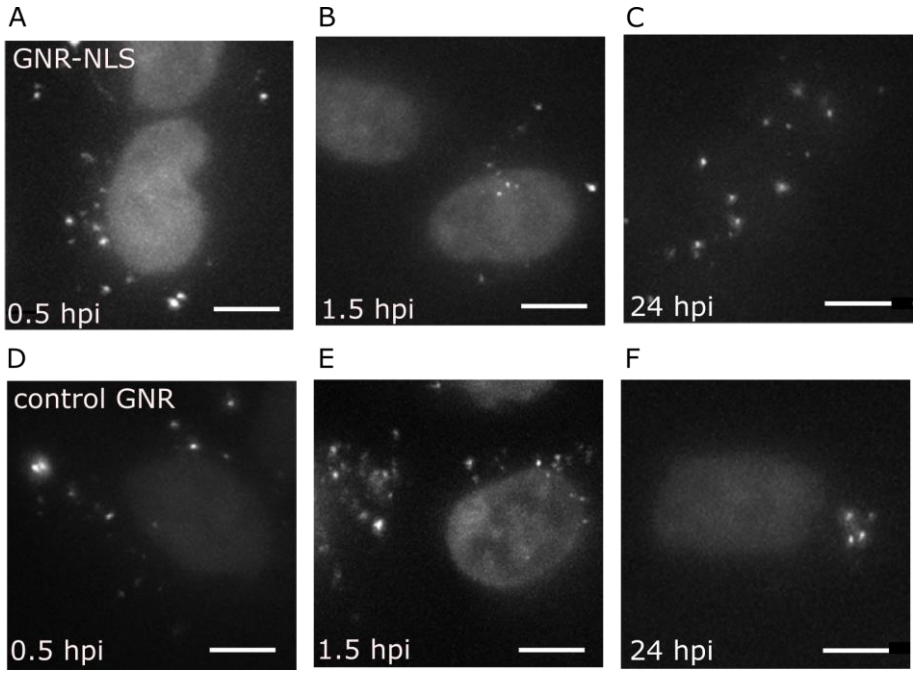

Figure 4. Representative two photon images of GNRs functionalized with a sulfo-SMCC peptide and subsequently with a NLS peptide (NLS-GNR) or GNRs functionalized with a sulfo-SMMC peptide only (control GNR) microinjected in the cytoplasm of HeLa cells over time. Nuclei were stained with Hoechst. A. NLS-GNR at 0.5 hours post injection. B. NLS-GNR at 1.5 hours post injection. C. NLS-GNR at 24 hours post injection. The scale bar corresponds with 10 µm. D. Control GNR at 0.5 hours post injection. E. Control GNR at 1.5 hours post injection. E. Control GNR at 24 hours post injection. The scale bars correspond with 10 µm.

Control GNRs do not appear in the nucleus at later time points either (figure 4B). In both NLS-GNR injected cells as well as control GNR injected cells, GNRs were found in or around the nuclear membrane (figure 5C). For the GNRs associated with the nuclear membrane no significant differences were observed between groups or time points. No significant difference between the number of NLS- and control GNRs located in the cytoplasm was observed at any time point. On average five to seven GNRs were found in the cytoplasm for both NLS-GNR injected cells as well as control GNR injected cells at 0.5 hours post injection (figure 5D). For both NLS- and control injected GNRs, a significant decrease in the number of cytoplasmic GNRs was

observed over time. As there is no effect of time on either the membrane or the nuclear population of GNRs, these GNRs did not move to another compartment of the cell. The percentage of NLS-GNR or control GNR for each compartment and at each time point is shown in 6A. These percentages also reflect the reduction of GNRs in the cytoplasm over time. It is important to note that at later time points the percentages depend on small numbers.

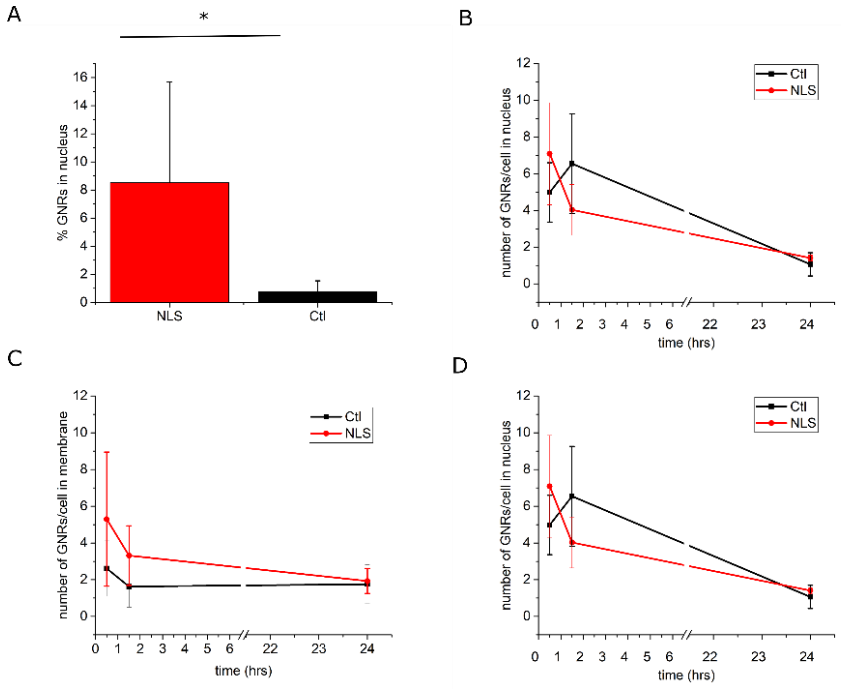

Figure 5. Quantification of NLS-GNR and control GNR over time in nucleus, membrane and cytoplasm. A. Percentage of NLS-GNR (NLS, red) or control GNR (Ctl, black) in the nucleus per cell at 0.5 hours post injection. Significance was tested using a ttest (* $p<0.05$). B. Number of NLS-GNR (NLS, red) and control GNR (Ctl, black) per cell in the nucleus over time. As a reference, the total NLS-GNR (NLS total) and control GNR (Ctl total) are plotted over time in a lighter color. C. Number of NLS-GNR (NLS, red) and control GNR (Ctl, black) per cell in or close to the nuclear membrane over time. As a reference, the total NLS-GNR (NLS total) and control GNR (Ctl total) are plotted over time in a lighter color. D. Number of NLS-GNR (NLS, red) and control GNR (Ctl, black) per cell in the cytoplasm over time. As a reference, the total NLS-GNR (NLS total) and control GNR (Ctl total) are plotted over time in a lighter color.

Cells containing GNRs were shown to be viable for at least 120 hours in the case of NLS-GNRs (Supplemental figure 2D-H) and 48 hours in the case of control GNRs (Supplemental figure 2I-L). No cells containing control GNRs could be found at 120 hours. The mobility of NLS-GNRs or control GNRs in the cytoplasm was similar (distribution, diffusion coefficient and confinement radius are shown in figure 5B-D). No significant differences were observed between both groups and the PEGylated GNRs (see figure 6B-D).

To control for the effect of functionalization, on each coverslip, around 20 cells were injected and the number of positive cells was calculated as the number of cells that could be positively identified to contain nanorods during imaging. The number of positive cells was significantly higher in NLS-GNRs (Supplemental figure 3A, two-way ANOVA comparing NLS-GNR and control GNRs over time) than in samples injected with control GNRs (Supplemental figure 3B) with a significant interaction between time and functionalization. Not only the number of positive cells, but also the number of GNRs per cell was significantly higher in the samples injected with NLS-GNRs (Supplemental figure 3C, two-way ANOVA comparing NLS-GNR and control GNRs over time) compared to control GNRs (Supplemental figure 3D). To account for the variation in the number of GNRs per compartment between individual cells we investigated the factors underlying the wide distributions for the number of GNRs per cell between samples injected with similarly functionalized rods, different types of samples were compared. First, to compare the reproducibility of the injection itself, two sets of injections on different coverslips were done on the same day (Supplemental figure 3 C-D, sample 3 and 4). Neither NLS-GNR or control GNRs showed a significant difference in the number of GNRs per cell between the two samples. Second, the reproducibility of the functionalization procedure was investigated. GNRs were functionalized with the sulfo-SMCC and NLS peptide just prior to each experiment. The number of GNRs per cell on two independent functionalizations are compared (Supplemental figure 3 D-E, sample 2 compared with sample 3 or 4).

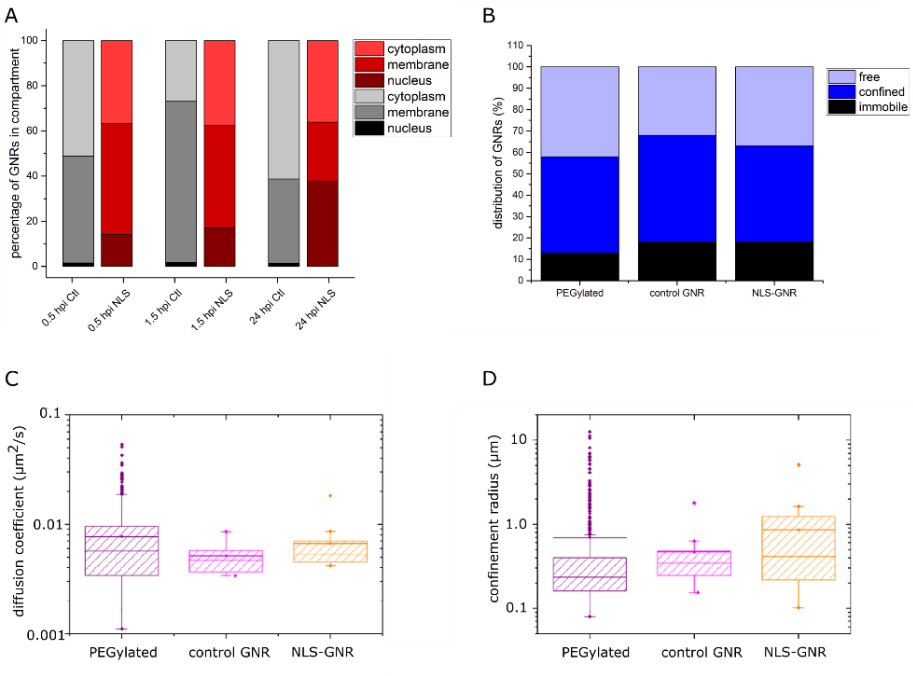

Figure 6. A. Percentage of NLS-GNR (NLS, red) or control GNR (Ctl, black) in each compartment of the cell; in the nucleus (nucleus), in or close to the nuclear membrane (membrane) or in the cytoplasm (cytoplasm), at each imaging time point. B. Distribution of NLS- or control GNRs according to mobility pattern (i.e. immobile, confined diffusion or free diffusion) in the cytoplasm. C Diffusion coefficient of NLS- or control GNRs in the cytoplasm. D. Confinement radius for NLS- or control GNRs in the cytoplasm. PEGylated GNRs were imaged at 0.5 hours post injection and are therefore compared to control and NLS-GNR at 0.5 hours post injection.

Third, the effect of GNR sedimentation over time was investigated. GNRs were left to sediment for one month, but were sonicated prior to functionalization. A big reduction in the number of GNRs per cell after sedimentation is shown (Supplemental figure 3C- comparison sample 1 and 2). This was congruent with a shift in the UVvis-spectrum (Supplemental figure 3E-F). Together these results show that the injection have a small effect on the number of GNRs per cell, the functionalization introduces a modest variation, but it is mostly the sedimentation of GNRs over time that reduces the number of GNRs successfully injected in the cells. The number of GNRs located in the nucleus for each cell was linearly correlated with the

total number of GNRs in that cell (Supplemental figure 5A), showing that a similar percentage of GNRs translocates to the nucleus in all cells. However, there was a group of non-responding cells showing no nuclear translocation.

5.3 DISCUSSION

In the present study, we have developed a method to study GNRs in live cells. Here, we have used nanorods had a characteristic size of 63 x 23 nm and a PEG layer of 8.1 nm. Using a two-photon microscope we obtained images of GNRss with high resolution and speed. GNRs injected either in the nucleus or the cytoplasm showed diffusive behavior characteristic of free diffusion or confined diffusion. There were no significant differences between the nucleus and the cytoplasm in any of the observed parameters. Upon functionalization of GNRs with an NLS, GNRs injected into the cytoplasm translocated to the nucleus.

Approximately 45% of the intracellular rods diffused freely, and there were no significant differences in the mobility between rods injected into the nucleus and into the cytoplasm. The similar diffusion coefficients observed in the nucleus and cytoplasm are in accordance with the comparable viscosity reported for both compartments (19). The intracellular viscosity is up to 3.2 times higher than water (20), which yields a theoretical diffusion coefficient of 2-10 $\mu m^2/s$ for particles of a size similar to that of our GNRs. This diffusion coefficient is 2 to 3 orders of magnitude higher than the diffusion coefficient we obtained in this study (0.01 $\mu m^2/s$) although there was a large variation in the diffusion coefficients obtained. In a similar study, GNRs of a comparable size were found to be actively transported at a velocity of 0.023 $\mu m/s$ and had a diffusion coefficient of 0.00042 $\mu m^2/s$ (21).

Recently, the concept of phase separation in living cells has been revisited (22). This phenomenon of the formation of droplets without barriers, induced by crowding, could explain local changes in viscosity and would result in a large distribution of diffusion coefficients. Furthermore, the presence of obstacles (chromatin for example in the nucleus or the endoplasmic reticulum in the cytoplasm) and short non-specific interactions between the PEG brush and the cellular environment were not taken into

account in the theoretically postulated diffusion coefficient, but might have a profound effect on the diffusion coefficient in live cells. Of all GNRs 42% was confined within a confinement radius of 0.65 nm on average, but a wide range of confinement radii, from about 100 nm to 1 µm was observed. This is within the range of the expected size of a lysosomal vesicle (~0.5 µm), but might also be related to the obstacles GNRs effectively encounter in the cells or the phenomenon of phase separation. Only 10-15% he GNRs was completely immobile. This was similar for both the nucleus and the cytoplasm and could be due to sticking of the rods to stationary objects in either the nucleus or the cytoplasm. In the cytoplasm this could also project uptake in vesicles. In the nucleus this might represent trapping of the nanorods in chromatin dense regions. Functionalization of GNRs with the sulfo-SMCC or the NLS did not influence the mobility of the rods. Previously it was hypothesized that addition of positively charged peptides, such as cell-penetrating peptides enhanced lysosomal escape and could increase the number of diffusing particles. Here, we did not observe such an effect, suggesting that the number of GNRs present in lysosomes is low.

In addition to the mobility, we investigated the functionality of a peptide conjugated to the GNRs. Attaching an NLS to GNRs through a linker peptide resulted in nuclear translocation of 8% of the nanorods, which did not occur for GNRs only functionalized with the linker peptide. The NLS conjugated to these GNRs was therefore considered to be functional, although the percentage of translocated GNRs was low. Previously the inefficiency of nuclear translocation was hypothesized to be due to reduced diffusion of larger particles towards the nucleus. Interestingly, in this study nuclear translocation was already observed at the earliest measurable time point using our experimental setup (30 minutes after injection). The percentage of GNRs in the nucleus did not increase over time, suggesting that nuclear translocation is already completed after 30 minutes and the diffusion towards the nucleus is not a limiting factor. The timing is consistent with a study concerning gold nanospheres that looked at nuclear localization after one hour (17)

It is likely that the size of these GNRs itself is the limiting factor precluding nuclear translocation. Most likely, these rods can only traverse the nuclear pore along their longitudinal axis. This is supported by the number of GNRs that are found at the nuclear membrane, which appears to be slightly higher for NLS-conjugated GNRs at earlier time points as compared to control nanorods. A reduction in the size of the GNRs might lead to a higher translocation. Indeed the percentage of nuclear translocation (35%) of gold nanospheres was found to be size-dependent (17). Interestingly, in our study the number of GNRs in the cytoplasm and to a lesser extent at the nuclear membrane decreased over time, whereas the number in the nucleus remained stable over time. These data suggest that the nanorods were exocytosed from the cytoplasm. Exocytosis of particles in the cytoplasm was previously been reported by others (7,23).

In all experiments carried out in this study using GNRs conjugated with a NLS, nuclear translocation was observed. However, the magnitude of the response differed between samples and led us to investigate some of the causes for the heterogeneity in our results. Firstly, cells injected with GNRs cojugated with an NLS showed intracellular GNRs more often than cells injected with nanorods conjugated with only the sulfo-SMCC linker. It is possible that the sulfo-SMCC linker peptide caused aggregation of the GNRs during the injection process and therefore blocked the GNRs from entering the cells. Alternatively, cells with a low number of GNRs may have already exocytosed the control GNRs from the cytoplasm before 30 minutes after injection (when imaging started), hence appearing as negative cells. GNRs functionalized with an NLS are translocated to the nucleus before they can be exocytosed. Secondly, the number of GNRs injected per cell was variable. The largest variation appeared after batches of GNRs were left to sediment over time even with though the samples were sonicated prior to use. This was also reflected in a shift in the UVvis-spectrum. Sedimentation leads to aggregation and therefore an underestimation of the concentration of single particles which can be successfully injected in the cells. Together these results show that this method for the delivery of GNRs could be optimized further and must always be carefully controlled. Based on these results it is highly advisable to prepare GNRs fresh and remove any sedimentation

before use. A good quality control for this was shown to be the UVvis-spectrum in which a shift can be detected that indicates changes in the GNRs.

In conclusion, in this study we have taken a first step towards the quantitative study of the behavior of GNRs in live cells. Owing to their photostability and brightness GNRs are promising for the use as probes. Easy conjugating of GNRs to cellular components would allow tracking of these components for arbitrary long times. For this application it is important that GNRs can diffuse freely in the cellular milieu. In this study we show free diffusion of 42% of all GNRs in both the cytoplasm and the nucleus. However, the diffusion coefficient observed for these particles was very low (0.01 $\mu m^2/s$) compared to the expected diffusion coefficient. Possibly interactions and stickiness with cellular components affects their diffusive behavior. This severely limits their use as probes in live cells. Changes in coating of the particles might be beneficial in this respect. In addition, a seduction in their size, with conservation of the aspect ratio, might also lead to an increase in diffusion coefficient. A diffusion coefficient that is more similar to that of the protein might improve their feasibility for this purpose. Although promising, the low diffusion coefficient is currently limiting the application of GNRs in live cell applications. Injection of GNRs in either the nucleus or the cytoplasm was followed by free diffusion for 42% of the rods inside living cells, and no differences between the mobility of GNRs in the nucleus or the cytoplasm were found. This suggest that their mobility is mainly determined by characteristics of the population of injected GNRs and the viscocity of the intarcellular environment Conjugation of an NLS to the GNRs resulted in translocation of a small percentage of injected GNRs to the nucleus, demonstrating that proteins conjugated to the GNRs can retain their functionality, enabling studies on proteins labeled with GNRs in living cells.

5.4 Materials and Methods

GNR synthesis and PEGylation

Gold nanorods were grown through the following steps. To make the seed solution 5 ml, $HAuCl_4$ (1.25 mM) in water was added to a CTAB solution (0.2 M in H_2O). This was followed by 600 µl $NaBH_4$ which acted as a reducing agent and the resulting yellow/brown solution was vortexed for 2 min. and left to

stand for 1 h. Subsequently, 95 ml $HAuCl_4$ (2.5 mM) was added to the same volume of 0.2 M CTAB, leading to a yellow solution. $AgNO_3$ (3.8 ml, 4mM) was added and this resulted in the solution changing color to yellow/orange. Ascorbic acid (1.33 ml, 78.8 mM) was subsequently added to reduce the gold and as a result the solution became colorless. Finally, 228 µl of the seed solution was added to nucleate growth of the GNRs. The solution became purple over the course of approximately 30 minutes. After approximately 12 hours growth, the GNRs were centrifuged, the supernatant was removed to remove the excess CTAB. The GNRs were resuspended in deionized water and stored. To coat the GNRs with polyethylyne glycol (PEG) the GNRS, bifunctional α-mercapto-ω-amino PEG_{5000} hydrochloride was added to the GNRs in a 500,000x excess to ensure full surface coverage. The GNR-PEG solution was left to stir at room temperature overnight before the GNRs were centrifuged. The supernatant was removed and the GNRs were resuspended in a phosphate buffered saline solution (PBS).

SULFO-SMCC CONJUGATION

The heterobifunctional cross-linker sulfo-SMCC (0.1 mg) was dissolved in 200 µl water and added to a solution of PEGylated GNRs (0.1 nM, 5 ml) in PBS. The solution was left to stir for 30 minutes before centrifugation and removal of the supernatant. The GNRs were subsequently resuspended in 4 ml PBS.

NLS SYNTHESIS AND CONJUGATION

The nuclear localization signal (NLS) peptide was synthesized on a Rink-amide resin using standard fmoc-chemistry, by a microwave-assisted Liberty I automated peptide synthesizer. Couplings were performed using HCTU as the coupling agent and DIPEA as the base. After synthesis, the peptide was acetylated at the N-terminus using a solution of acetic anhydride (5%), and pyridine (6%) in DMF. This was left to react for one hour before the peptide was cleaved from the resin using a TFA:H2O:TIPS:EDT (95:2:2:1) cocktail. After 2 hours, the peptide was precipitated into ice-cold diethyl ether, the precipitate collected by centrifugation, dissolved in water and freeze-dried to obtain a white powder. The peptide was purified by reversed-phase HPLC using a C18 column and a gradient from A (water) to B (MeCN) of 0 – 50% over 30 minutes. The purified peptide was identified by LC-MS spectroscopy.

For the conjugation of the NLS to the GNRs, 1 ml containing 1 mg of NLS peptide was added to 4 ml of GNR dissolved in PBS. The resulting solution was left to stir for 1 hour before centrifugation. Subsequently, the supernatant was removed and the GNRs were resuspended in PBS.

Cell culture and Hoechst staining

HeLa cells were cultured in Dulbecco's Modified Eagle's Medium (DMEM) (Gibco) supplemented with 10% fetal calf serum (FCS). Cells were kept at 37 °C and 5% CO_2. One day prior to injection, 1.0 x 10^5 HeLa cells were plated in each well of a 6-well plate (Sarstedt) in which coverslips of Ø 25 mm with 1.5 mm thickness (Thermo Scientific) were located. The wells contained 2 ml DMEM supplemented with 10% FCS. When necessary, cells were stained with Hoechst 3442* (*) prior to injection. A 1:2000 dilution of made of the Hoechst (*concentration) in PBS. Cells were washed once with PBS and incubated with the Hoechst solution for 20 minutes. Subsequently, cells were washed 3 times with PBS and kept in DMEM until used for experiments.

Single-cell microinjection

On the day of injection, coverslips containing cell monolayers with 50-80% confluency were selected and placed in a metal ring holder. One ml of DMEM was placed on top of the cells. The sample was placed on a relief phase contrast microscope (CKX41, Olympus) using a 20x objective (Olympus). This microscope contained an additional support beam holding an injection arm (Eppendorf). A microinjection capillary (Femtotip II needle (Eppendorf)) was loaded with 3 µl 0.12 nM PEGylated GNRs or carboxyfluorscein in PBS (Sigma Aldrich, Zwijndrecht, Netherlands). The needle was placed in the holder on the injection arm and connected to a Femtojet Microinjector (Eppendorf). A constant pressure of 150-250 hPa was supplied. After injection, cells were incubated at 37 °C and 5% CO_2 for 30 minutes.

Confocal and two-photon imaging

Cells injected with carboxyfluorescein were imaged using a confocal microscope (Leica SPE) with a 63x 1.2 NA water immersion objective.

A two-photon multifocal scanning microscopy setup [14] was used for two-photon imaging. The excitation beam, generated with a pulsed IR laser (Chameleon Ultra, Coherent), was split into an array of 25x25 focal spots by a diffractive optical element (custom-made by Holoeye Photonics). The array of beams was then scanned by a scanning mirror (FSM-300, Newport). A square wide-field illumination was thus obtained, covering an area in the sample of approximately 60 µm x 60 µm. A piezo-actuator (P-726 Pifoc, PI) was used to move the objective (60x APOTIRF, Nikon) in the z direction to acquire frames at different z positions. A LED light was used to obtain transmission images of the cells. We acquired image sequences of GNRs in cells, alternating z-stacks of fluorescence images with transmission images of the cells. A fluorescence stack was made of typically 15 to 20 2D frames, spaced 0.5 µm between each other. The acquisition rate was 8 frames/s, allowing for 2-3 s/3D stack. One movie typically contained 300-1000 stacks. Fluorescence images were acquired with an excitation wavelength of 770 nm, exciting both GNRs and the Hoechst dye. When the Hoechst intensity was too high to clearly distinguish GNRs, a long-pass filter at 515 nm was used to partially filter the signal of the dye.

IMAGE ANALYSIS

We distinguished the GNRs in the cytoplasm, in the nucleus and in the nuclear membrane using the 3D fluorescence images of each cell. The GNRs of which the signals did not overlap with that of the Hoechst dye were counted as residing in the cytoplasm. GNRs on the edges of the Hoechst staining were counted as membrane-bound, while GNRs inside the regions labeled by Hoechst staining were counted as localized in the nucleus.

In every frame of the 3D movie we localized small volumes of interest (typically 10 x 10 pixels in x, y and 5 slices in z) around each bright fluorescent signal attributed to a GNR. Subsequently, we performed a 3D Gaussian fit on each volume of interest to obtain nanometer accurate 3D coordinates of the GNRs. The coordinates of a GNR at each time point were then connected into a trace, using a nearest-neighbor algorithm. Traces shorter than 4 frames were excluded from the analysis. In each movie we defined the regions corresponding to cell nuclei using the Hoechst staining. We analyzed the

mobility of GNRs in the cytoplasm, both for NLS-GNRs and sulfo-SMCC-GNRs. We did not analyze the mobility of GNRs in the nucleus and nuclear membrane separately due to the difficulty to automatically distinguish between these populations. In a few cases, GNRs were present outside the cells: we did not include these GNRs in the analysis. To analyze the mobility of the particles, we calculated the mean squared displacement (MSD) for each trajectory, which is defined as the average of the squared displacements covered by the particle in time steps of duration τ. In the case of a freely diffusing particle, the MSD exhibits a linear dependence on τ, that defines the diffusion coefficient D of the particle:

$$MSD(\tau) = 6\sigma^2 + 6D\tau \qquad \text{Eq. 1}$$

In equation 1 *D* is the diffusion coefficient of a particle, which depends on the size of the particle and on the temperature and viscosity of the medium, according to the Stokes-Einstein equation. From fitting the MSD we obtain the diffusion coefficient *D*. The localization accuracy σ was for every single GNR a fixed value. Based on the typical photon emission of the GNRs we use for our experiments, the localization accuracy in 3D is approximately 40 nm. GNRs showing an MSD at any time point lower than 6 times the square of the localization accuracy (~0.01 μm^2) were considered immobile.

When the MSD is plotted against τ, the presence of a confinement limiting the particle mobility results in a flattening of the curve that depends on the confinement radius *R.* If an active component is present in the motion, a steepening of the curve will be observed, that depends on the velocity *v* of the particle. However, using the current measurement parameters, it was not possible to accurately obtain *R* or *v* from individual traces. The acquired GNR traces were typically less than 10 frames long. The error on each determined MSD value is strongly influenced by the length of the trajectory. This error gets larger with increasing τ,due to the decreasing number of values used to calculate the mean. Therefore, it was not possible to distinguish a curvature in MSD plots from stochastic variations of a single trace and to reliably determine the mobility mode (free diffusion or confined diffusion) from the curve. Instead, we analyzed the ensemble distribution of MSD values at each time lag to distinguish populations with different mobility

modes by thresholding the MSD at the largest τ. We then fitted the MSD plot of individual traces with the corresponding mode. From this we obtained the diffusion coefficient and the radius of confinement. This approach allows for distinguishing free from confined populations, but not from active populations. This MSD analysis of GNR traces was performed in LabVIEW. For statistical analysis of the data we used a Single-Factor Analysis of Variance (ANOVA), with a p-value threshold of 0.05. For non-Gaussian distributions, a non-parametric ANOVA (Kruskal-Wallis test) was used.

REFERENCES

1. Kodiha M, Wang YM, Hutter E, Maysinger D, Stochaj U. Off to the organelles - killing cancer cells with targeted gold nanoparticles. Theranostics. 2015;5(4):357–70.

2. Dreaden EC, Austin LA, Mackey MA, El-Sayed MA. Size matters: gold nanoparticles in targeted cancer drug delivery. Ther Deliv [Internet]. NIH Public Access; 2012 Apr [cited 2017 Dec 11];3(4):457–78. Available from: http://www.ncbi.nlm.nih.gov/pubmed/22834077

3. Lévy R, Shaheen U, Cesbron Y, Sée V. Gold nanoparticles delivery in mammalian live cells: a critical review. Nano Rev [Internet]. 2010;1(1):4889. Available from: https://www.tandfonline.com/doi/full/10.3402/nano.v1i0.4889

4. Derfus AM, Chan WCW, Bhatia SN. Intracellular delivery of quantum dots for live cell labeling and organelle tracking. Adv Mater. 2004;16(12):961–6.

5. Doyon JB, Zeitler B, Cheng J, Cheng AT, Cherone JM, Santiago Y, et al. Rapid and efficient clathrin-mediated endocytosis revealed in genome-edited mammalian cells. Nat Cell Biol [Internet]. Nature Publishing Group; 2011;13(3):331–7. Available from: http://dx.doi.org/10.1038/ncb2175

6. Chithrani DB. Intracellular uptake, transport, and processing of gold nanostructures. Mol Membr Biol [Internet]. 2010 Oct 7 [cited 2017 Dec 11];27(7):299–311. Available from: http://www.ncbi.nlm.nih.gov/pubmed/20929337

7. Yang C, Uertz J, Yohan D, Chithrani BD. Peptide modified gold nanoparticles for improved cellular uptake, nuclear transport, and intracellular retention. Nanoscale [Internet]. Royal Society of Chemistry; 2014;6(20):12026–33. Available from: http://xlink.rsc.org/?DOI=C4NR02535K

8. Chen ZP, Xu RZ, Zhang Y, Gu N. Effects of proteins from culture medium on surface property of silanes- functionalized magnetic nanoparticles. Nanoscale Res Lett. 2009;4(3):204–9.

9. Zhang W, Ji Y, Wu X, Xu H. The Trafficking of Gold Nanorods in Breast Cancer Cells : Uptake , Lysosome Maturation and Elimination The Trafficking of Gold Nanorods in Breast Cancer Cells : Uptake , Lysosome Maturation and Elimination. ACS Appl Mater Interfaces [Internet]. 2013;5(19):9856–65. Available from: http://dx.doi.org/10.1021/am4033857%5Cnhttp://www.ncbi.nlm.nih.gov/pubmed/24033123%5Cnhttp://pubs.acs.org/doi/abs/10.1021/am4033857%5CnAll Papers/Z/Zhang et al. 2013 - The Trafficking of Gold Nanorods in Breast Cancer C ... ods in Breast Cancer Cells - Up

10. Nativo P, Prior IA, Brust M. Uptake and intracellular fate of surface-modified gold nanoparticles. ACS Nano. 2008;2(8):1639–44.

11. Zu Y, Huang S, Liao WC, Lu Y, Wang S. Gold nanoparticles enhanced electroporation for mammalian cell transfection. J Biomed Nanotechnol. 2014;10(6):982–92.

12. Lißе D, Monzel C, Vicario C, Manzi J, Maurin I, Coppey M, et al. Engineered Ferritin for Magnetogenetic Manipulation of Proteins and Organelles Inside Living Cells. Adv Mater [Internet]. 2017 Nov [cited 2017 Dec 11];29(42):1700189. Available from: http://www.ncbi.nlm.nih.gov/pubmed/28960485

13. Lee KJ, Nallathamby PD, Browning LM, J C, Xu XN. NIH Public Access. In Vivo (Brooklyn). 2009;1(2):133–43.

14. Bar-Ilan O, Albrecht RM, Fako VE, Furgeson DY. Toxicity assessments of multisized gold and silver nanoparticles in zebrafish embryos. Small. 2009;5(16):1897–910.

15. Abdelrasoul GN, Magrassi R, Dante S, d'Amora M, d'Abbusco MS, Pellegrino T, et al. PEGylated gold nanorods as optical trackers for biomedical applications: an *in vivo* and *in vitro* comparative study. Nanotechnology [Internet]. 2016 Jun 24;27(25):255101. Available from: http://stacks.iop.org/0957-4484/27/i=25/a=255101?key=crossref.9ec8c30785c91b2d429b9b3ded6d37c4

16. Huo S, Jin S, Ma X, Xue X, Yang K, Kumar A, et al. Ultrasmall gold nanoparticles as carriers for nucleus-based gene therapy due to size-dependent nuclear entry. ACS Nano. 2014;8(6):5852–62.

17. Pante N, Kann M. Nuclear Pore Complex Is Able to Transport Macromolecules with Diameters of 39 nm. Mol Biol Cell [Internet]. 2002;13(2):425–34. Available from: http://www.molbiolcell.org/cgi/doi/10.1091/mbc.01-06-0308

18. Oyelere AK, Chen PC, Huang X, El-Sayed IH, El-Sayed MA. Peptide-conjugated gold nanorods for nuclear targeting. Bioconjug Chem. 2007;18(5):1490–7.

19. Luby-Phelps K. The physical chemistry of cytoplasm and its influence on cell function: an update. Mol Biol Cell [Internet]. American Society for Cell Biology; 2013 Sep [cited 2017 Dec 11];24(17):2593–6. Available from: http://www.ncbi.nlm.nih.gov/pubmed/23989722

20. Fushimi K, Verkman AS. Low viscosity in the aqueous domain of cell cytoplasm measured by picosecond polarization microfluorimetry. J Cell Biol [Internet]. The Rockefeller University Press; 1991 Feb [cited 2017 Dec 11];112(4):719–25. Available from: http://www.ncbi.nlm.nih.gov/pubmed/1993739

21. Huff TB, Hansen MN, Zhao Y, Cheng J, Wei A. Controlling the Cellular Uptake of Gold Nanorods Controlling the Cellular Uptake of Gold Nanorods Controlling the Cellular Uptake of Gold Nanorods. Langmuir. 2010;23(4):1–6.

22. Hyman AA, Weber CA, Jülicher F. Liquid-Liquid Phase Separation in Biology. Annu Rev Cell Dev Biol [Internet]. 2014;30(1):39–58. Available from: http://www.annualreviews.org/doi/10.1146/annurev-cellbio-100913-013325

23. Chu Z, Zhang S, Zhang B, Zhang C, Fang C-Y, Rehor I, et al. Unambiguous observation of shape effects on cellular fate of nanoparticles. Sci Rep [Internet]. Nature Publishing Group; 2014 Mar 28 [cited 2017 Dec 11];4:4495. Available from: http://www.ncbi.nlm.nih.gov/pubmed/24675513

5.5 SUPPLEMENTARY FIGURES

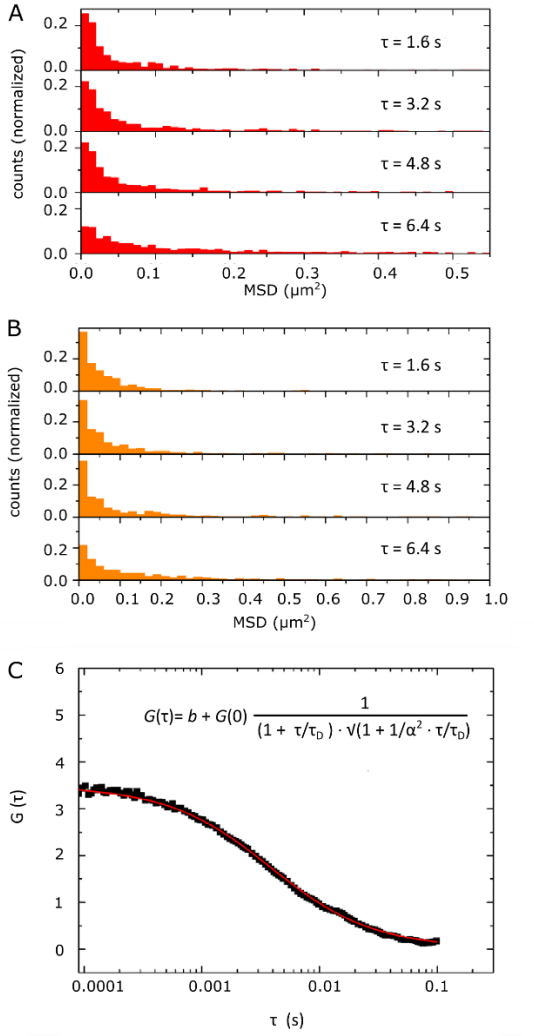

Supplemental figure 1. A. MSD histograms from traces of GNRs injected in the cytoplasm at different timelags (τ). B. MSD histograms from traces of GNRs injected in the nucleus at different timelags (τ). A small fraction, typically < 5%, exceeding MSD = 1 μm² was attributed to artifacts originating from erroneous connection of peaks and was omitted. C. FCS measurement of GNRs. Fluorescence correlation spectroscopy on a solution of 47 nm x 14 nm GNRs in water. The fit gave τ_D = 3.85x10^{-3}s, from which the diffusion coefficient (D) is calculated to be 7.5x10^{-2} μm²/s is calculated. The hydrodynamic radius, calculated using Eq. 2.4, is 29.1 nm. The equivalent radius of our GNRs is 21 nm. Subtracting this value from the hydrodynamic radius, we obtained a PEG layer of 8.1 nm.

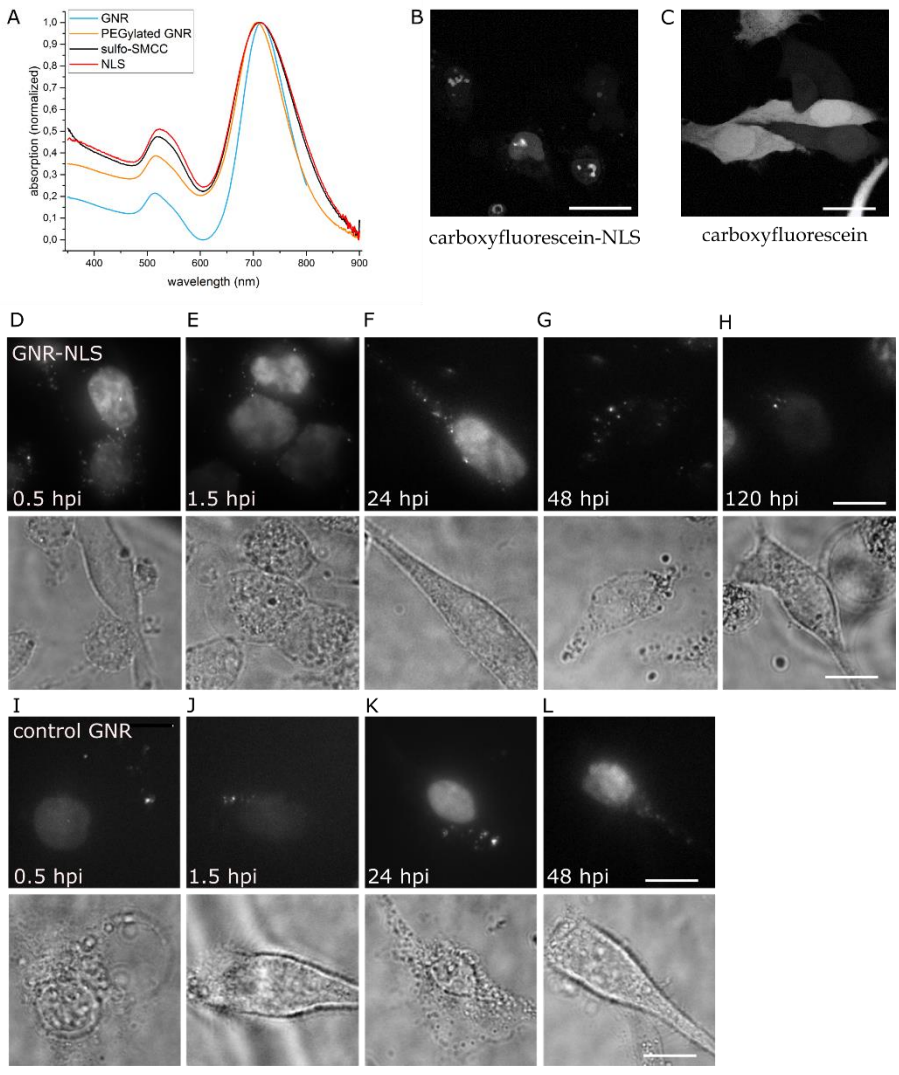

Supplemental figure 2. A. UV-vis spectrum of GNR, bare (blue), after PEGylation (yellow), after conjugation with the sulfo-SMCC peptide (black) and after NLS functionalization (red). B. Confocal image of carobxyfluorsecein-NLS injected in the cytoplasm of HeLa cells. The scale bar corresponds with 20 µm. C. Confocal image of carboxyfluorescein injected in the cytoplasm of HeLa cells. The scale bar corresponds with 20 µm. D-H. Representative two-photon image and brightfield image of GNRs functionalized with a sulfo-SMCC peptide and subsequently with a NLS peptide (NLS-GNR) over time. The scale bars correspond with 10 µm. I-K. Representative two-photon image and brightfield image of GNRs functionalized with a sulfo-SMMC peptide only (control GNR) over time. The scale bars correspond with 10 µm.

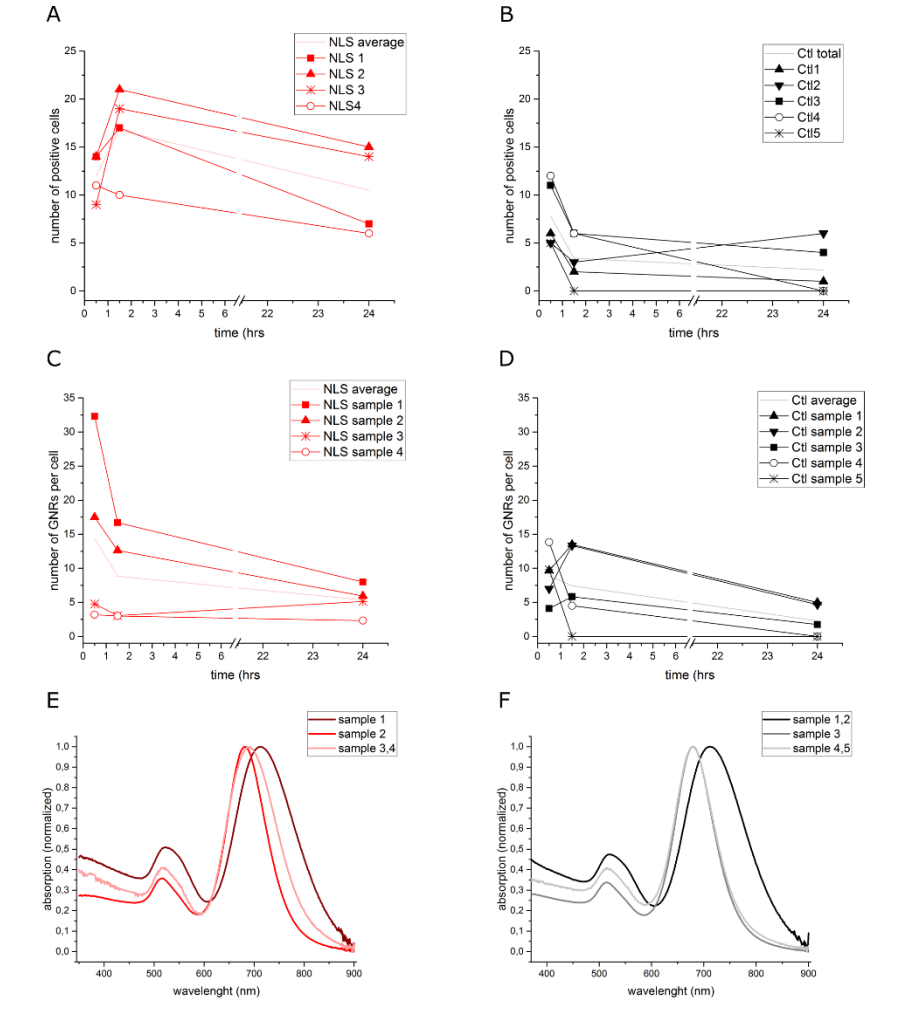

Supplemental Figure 3. Robustness of the method. A. Number of positive cells injected with NLS-GNR or control GNR. B. Number of GNRs injected per cell with NLS-GNR or control GNR. C. Number of GNRs injected per cell with NLS-GNR for the different injections (3, 4), functionalization (2, 3/4) and sedimentation times (1, 2). D. Number of GNRs injected per cell with control GNR for different injections (3, 4), functionalization (2, 3/4) and sedimentation times (1, 2). E. UV-vis spectrum of NLS-GNR under different conditions. F. UV-vis spectrum of control GNR under different conditions. G. Percentage of NLS-GNRs in the nucleus at 0.5 hours after injection.

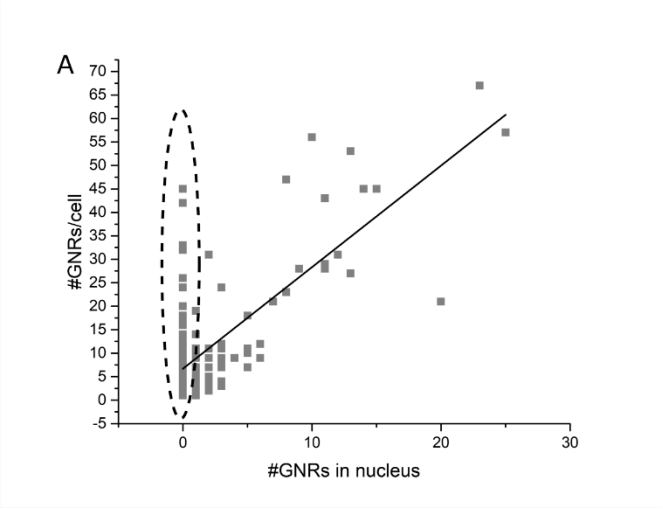

Supplemental figure 4. Effect of number of GNRs injected on nuclear translocation. A. Number of NLS-GNRs per cell as a function of the number of NLS-GNRs in the nucleus. The adjusted R value for the correlation is 0.53. A group of non-responding cells containing NLS-GNRs that show no nuclear translocation is circled.

6 SUMMARY AND DISCUSSION

The glucocorticoid receptor is a well-studied transcription factor that serves as a model for transcription factor dynamics. In this thesis, we have developed a framework to advance our understanding of glucocorticoid receptor dynamics in the nucleus of live cells. To this end, we set out to gain biological insight as well as advance the analysis and technology used to investigate these processes. In this chapter, major findings are summarized and discussed and future directions are proposed.

The study carried out in **chapter 2** of this thesis has led to the discovery of several GR dynamics states and insight into how the receptor finds its target, which included repetitive switching between states. We also identified specific amino acids involved in long binding times of the GR. Quantification of single molecule data and FRAP experiments led us to develop a continuous time Markov chain model through which we could obtain information about switching even when using data obtained on shorter time scales. In **chapter 3**, through correction for the loss of fast molecules through a limiting depth of focus we obtained true fraction size for GR molecules in the nucleus of live cells. Through this, we could understand that switching of GR between states occurred at a larger time scale. In addition, **in chapter 4** GR clusters were revealed. Through quantification, we could describe these clusters and find characteristic that distinguished GR clusters from clusters of a closely related ER. Moreover, we could exclude that the distribution of the receptor within receptor specific foci was dependent on specific DNA binding. In particular, we have achieved progress in the analysis of single-molecule data. We have investigated alternative labeling methods for proteins in live cells in **chapter 5,** to observe the dynamics and localization of individual GRs on longer time scales. To this end, we have characterized the behavior of golden nanorods (GNRs) in both cytoplasm and nucleus. We showed that functionalization of GNR with NLS enables nuclear translocation. This indicates that GNRs can be functionalized and used as a label for GR tracking.

6.1 THE DYNAMICS OF THE GR (CHAPTER 2 AND 3)

In this thesis, we provide the most complete picture of GR dynamics to date. In **chapter 2**, GR dynamics in the nucleus of live cells was investigated by combining single-molecule microscopy and FRAP experiments. To this end, COS-1 cells were used that transiently expressed YFP labeled GR proteins. Four states with different dynamic properties were identified for the GR: two binding states and two diffusion states. Moreover, a mathematical framework was employed based on a continuous time Markov chain model to investigate the time spent in each of these states as well as the transition probabilities between states. In addition, DNA-binding domain mutants were exploited with a range of DNA-binding affinities to investigate the molecular mechanisms that underlie each of the states. When these results were combined, we concluded that GRs in the fast diffusion state is are freely diffusing through the nucleus, that GRs in the slow diffusion state are transiently interacting with DNA, that indirect binding to DNA leads to immobilizations with a short residence time and that direct DNA binding results in immobilization with a long residence time. Moreover, we show that the GR spends relatively long periods of time in the free diffusion state and once it leaves this state, it repeatedly alternates between brief nonspecific DNA interactions and longer immobilizations due to specific DNA binding ('repetitive switching'). Together these results provide a picture of how the GR finds its target on the DNA. This picture fits well within the theoretical description for target searching strategies of transcription factors, which propose a combination of 1D and 3D diffusion as the most effective way to reach a specific DNA target motif (1–3). Since the GR serves as a well-studied example of transcription factor functioning, it is likely that this mechanism is used by other transcription factors as well, but further studies should be carried out on other transcription factors to confirm this.

It is striking that the receptor has a high chance to switch from a free diffusion state to a slow diffusion state, but a low chance of switching from the free diffusion state to a direct or indirect binding state. This implies that the receptor has to switch to a different conformation or become part of a (different) multiprotein complex or that it reaches a different environment. This is supported by the long time that the receptor spends in the free

diffusion state. In this novel conformation, protein complex or nuclear environment, it is slowed down due to the increased number of (nonspecific) interactions with other (DNA) molecules. Another striking aspect of this research is alternating of the receptor between slow diffusion and binding. This indicates that once it reaches the slow diffusion state it is likely to remain within a limited region of the nucleus as it now only diffuses slowly. This allows for effective searching and binding within this region.

To better interpret the results obtained using single-molecule microscopy, in **chapter 3** we have developed novel analysis methods to faithfully determine the fraction of diffusing receptors and understand the timescales at which switching occurs. We can correct for the depletion of fast mobile fractions due to the axial limitation of the observation volume. Due to the limited detection volume, the fraction of fast diffusing molecules is depleted when longer time scales are used. We derived an analytical solution for a system with two populations based on the chance of a molecule to remain in the observation volume and integrated over the depth of the volume. We did single molecule microscopy on YFP-GR in COS-1 cells using increasing time between frames from 6.25 milliseconds up to 100 seconds. Through application of particle image correlation spectroscopy, we could correlate particles between consecutive frames as well as every other frame (4). When we corrected the obtained fraction size of the two populations, the fraction of GR molecules remained stable over time scales that we have observed (up to 150 milliseconds). This indicates that switching must occur on a much time scales larger than 150 milliseconds. This is congruent with the findings from chapter 2, in which we employed continuous time Markov chain models and find that switching must occur on the time scale of 600 milliseconds to tens of seconds.

6.2 THE LOCALIZATION OF THE GR (CHAPTER 4)

In the light of the results obtained in chapter 2, we expected to find regions in the nucleus of live cells to which the receptor is confined due to the slow diffusion and binding. Indeed, the occurrence of GR clusters has been observed previously, but thus far they had not been characterized extensively in a quantitative manner (5,6). In **chapter 4,** we carefully

characterized these clusters, or foci, in a quantitative manner. To this end, GFP-GR was stably expressed in U2OS cells, and spinning disk microscopy was used to obtain high-resolution images. An analysis pipeline was created in which individual nuclei were identified, a triangle threshold was applied and individual foci were identified. A Gaussian curve was fitted to the individual foci to obtain their width and intensity. We characterized the number of foci, their size and the relative number of molecules inside foci.

The molecular mechanism underlying the occurrence of these foci remains unclear. To obtain further insight into how foci differ between transcription factors, we compared GR foci with estrogen receptor (ER) foci. The ER was localized in significantly more, but smaller, foci than the GR. Together these findings imply that ER and GR foci are distinct entities. It has been hypothesized that foci correspond with specific DNA binding and subsequent transcriptional regulation. The GR and ER each recognize a different DNA binding motif (glucocorticoid or estrogen response elements (GREs or EREs)). Within the DNA-binding-domain of these receptors, the p-box dictates binding of the receptor to either GREs or GREs. Previous studies have shown that exchanging three amino acids within the p-box of the ER to those corresponding with the GR led to the recognition of GREs by the ER (7,8). This mutant was termed ERpGR. We exchanged the same amino acids in the GR, thereby generating GRpER. We have demonstrated that the foci's characteristics (like width and number) of these mutant receptors do not change compared to their WT receptors. This suggests that clustering of EREs or GREs in the nucleus, either pre-existing or formed upon ER or GR binding, does not explain the presence of foci.

Seemingly in contrast, previous studies have shown that the GR DNA-binding domain is required for the formation of focal domains inside the nucleus (5). In addition, the degree of inhomogeneity is dependent on the specific ligand that is bound to the GR (5,6). These results suggest that the receptor-specificity of the formation of foci depends largely on the ligand-binding-domain, but that specific DNA binding to EREs or GREs through the DBD is a prerequisite for the formation of foci in general. Binding of cofactors might play an important role in this as well as dimerization. Indeed, the latter was

previously shown to be of importance in the number of foci (9). To understand whether GR and ER foci are separate entities as their number and size suggest, colocalization experiments are essential. As the width of the foci show a wide range of distributions for both receptors, it is possible that ER and GR foci with an identical size colocalize. Furthermore, colocalization studies of the mutant receptors described earlier, with their original receptors might provide further clues as to which processes are dependent on direct DNA binding. To understand the role of response elements in the formation of transcription factor foci, future experiments should also aim at combining live cell imaging techniques of transcription factors and methods such as HiC and ChIP-seq.

It would be interesting to quantify the relative position of foci in the nucleus to understand their possible interactions with structural components of the nucleus, such as nucleoli, PML bodies or Cajal bodies. Additionally, it has been noted that the N-terminal-domain of the GR is quite disordered. Disordered proteins can undergo liquid-liquid phase separation under the right conditions, which may result in the formation of nuclear foci (10–12).

In order to study the functional role of the foci, we could study colocalization with markers for active chromatin in live cells, for example by using mintbodies (13). Colocalization with markers for active transcription such as RNA poll II could also be used. It has been shown that RNA poll II also exists in foci (14). However, van Steensel et al. (15) showed no correlation of RNA poll II. with GR foci. Colocalization with known interaction partners based on the GR interactome could also provide useful to disentangle the molecular mechanisms behind each state. These include many other transcription factors.

6.3 Coupling localization and dynamics

To obtain a full understanding of how the GR functions as a transcription factor we need to combine methods that capture dynamics (as described in **chapter 2**) with methods that provide information on the spatial distribution (as described in **chapter 4**). We would like to understand if DNA-bound receptors are the ones present in foci, whether these are different from

indirectly bound molecules and whether the slow diffusion occurs inside or close to the foci. Experimentally, this could be done using combined expression of receptors labeled with two different fluorescent molecules: one at a high concentration for the visualization of the distribution (in particular the localization of the foci), and one at a low concentration of imaging and tracking of individual molecules. This could be performed using two different fusion proteins, or by using a Halo-tagged receptor and labeling with a combination of two Halo ligands.

During the life-cycle of the receptor heat-shock proteins and subunits of the proteasome are involved in multiple steps. In the absence of ligand, the GR is confined to the cytoplasm (16). It is present in a complex that includes heat shock proteins as well as immunophilins (17,18). Once activated by the ligand, the GR is translocated to the nucleus and will find and bind to response elements in the DNA. Where heat shock proteins might stabilize GR interactions with the chromatin, the proteasome promotes GR removal from the chromatin (19,20). Whether the receptor is then targeted directly for degradation or can be recycled remains unclear. It is likely that both processes occur. This is supported by studies that show that the receptor is more stable in the absence of a DBD, but that in the presence of a DBD activation of the receptor by a ligand leads to increased degradation (Schaaf and Cidlowski, unpublished data). Moreover, this is ligand-specific. It is possible that the foci that were identified in chapter 4 represent clustering of the receptor with components of the proteasome in the process of, or after unloading from the DNA and could even represent degradation sites.

Furthermore, it was striking to find that the long immobilizations were dependent on the presence of two specific amino acids in the DNA-binding-domain, whereas the short immobilizations were completely independent of the integrity of the DNA-binding-domain. This suggests that these are really two different processes. We suggest that short immobilization corresponds with tethering to other transcription factors. Alternatively, it could represent other processes such as degradation of the receptor. In this light, it would be interesting to investigate colocalization of the GR with well-known tethering

partners such as AP-1 or block degradation using drugs such as geldanamycin.

6.4 Long-term visualization and tracking of individual GRs (chapter 5)

It would be interesting to be able to assess whether receptors alternate between long and short immobilization times, and whether this occurs with intermittent slow diffusion. To obtain this kind of information tracking of individual receptors over longer periods of time is necessary. Ideally, we would like to be able to track a single receptor through multiple cycles of DNA binding and unbinding. This requires imaging on the time scale of minutes, with a high framerate (~200 Hz). Fluorophores currently available are prone to blinking and bleaching and hence these types of measurements are not feasible with these tools. Thus, there is a need to develop methods that allow for long-term visualization. In **chapter 5**, we explored the use of a material that could serve as a label for proteins and allows for tracking of arbitrarily long times. Once this method has been established, the work provided in chapter 2 will serve as a benchmark to control for the effect of a different label on the behavior of transcription factors.

To this end, we have investigated a new method that allows prolonged tracking of the GR in the nucleus of live cells in chapter 5. Gold nanorods are unaffected by bleaching and easily functionalized. To assess their feasibility as a label for the GR, we have characterized the behavior of gold nanorods in live cells. We developed a delivery method using microinjection of the gold nanorods into the nucleus or the cytoplasm and subsequently assessed the diffusion properties and confinement radius of these particles in both the nucleus and the cytoplasm. The diffusion coefficient for the particles used in this study was much smaller than theoretically expected and much smaller than that of the GR (21,22), although it was consistent with previous reports or particles this size (23). When the GNR would be coupled to the GR this might influence the diffusion of the receptor and therefore its function. In addition, the number of freely diffusing and translocating particles was found to be limited. In the nucleus as well as the cytoplasm only ~45% of the particles were freely diffusing.

The gold particles we used were coated with polyethylene glycol (PEG) molecules of 5000 kDa. These are large proteins that likely form brush-like structures around the GNR with which other proteins or structures inside the cell can easily interact. In addition, the percentage of nuclear translocation of gold nanospheres was previously found to be size-dependent (24). These findings lay bare the current limitations of gold nanorods as labeling probes for the GR. By decreasing the size and interactions with the cellular environment these particles might still be promising as a probe for the GR in the future. To reduce interactions with the cellular environment the coating of GNR proteins could be altered. Alternatives could be a smaller polymer or a silica shell.

To function as a label for the GR it is essential that these particles translocate to the nucleus only upon active translocation of the GR after induction with the ligand. We showed successful functionalization of these particles with a nuclear localization signal is possible (NLS). However, only 8% of the particles translated to the nucleus after functionalization with this NLS. It is likely that this limitation is related to the low number of freely diffusing particles, since free diffusion seems like a prerequisite for translocation to the nucleus. Together these findings indicate that the GNR could be used as a label for the GR, but that the efficiency would be very low.

6.5 Future perspective

Together, the chapters of this thesis provide an outlook for the investigation of transcription factors such as the GR. In particular, it seems essential to carefully quantify the processes involved. To this end, we must keep on developing novel analysis techniques. In addition, we need to couple localization in foci with binding and diffusion of the receptor. Looking at colocalization of the receptor with other nuclear factors will uncover the underlying biological mechanisms that dictate the distribution and dynamics of the GR. To this end microscopy tools, in particular single molecule approaches, remain a powerful tool. These tools should be combined with information on the conformation of DNA through tools such as HiC. Finally, the most information would be obtained through following a single receptor through multiple DNA binding and unbinding cycles. Therefore, increased

efforts to develop methods for high frame rate acquisition (milliseconds) over long time periods (hours) must be are required.

REFERENCES

1. Izeddin I, Récamier V, Bosanac L, Cissé II, Boudarene L, Dugast-Darzacq C, et al. Single-molecule tracking in live cells reveals distinct target-search strategies of transcription factors in the nucleus. Elife. 2014;3:e02230.

2. Normanno D, Dahan M, Darzacq X. Intra-nuclear mobility and target search mechanisms of transcription factors: A single-molecule perspective on gene expression. Biochim Biophys Acta - Gene Regul Mech. 2012;1819(6):482–93.

3. Normanno D, Boudarène L, Dugast-Darzacq C, Chen J, Richter C, Proux F, et al. Probing the target search of DNA-binding proteins in mammalian cells using TetR as model searcher. Nat Commun. 2015;6.

4. Semrau S, Schmidt T. Particle image correlation spectroscopy (PICS): retrieving nanometer-scale correlations from high-density single-molecule position data. Biophys J. 2007;92(2):613–21.

5. Schaaf MJ, Lewis-Tuffin LJ, Cidlowski JA. Ligand-selective targeting of the glucocorticoid receptor to nuclear subdomains is associated with decreased receptor mobility. Mol Endocrinol. 2005;19(6):1501–15.

6. Presman DM, Alvarez LD, Levi V, Eduardo S, Digman MA, Martí MA, et al. Insights on glucocorticoid receptor activity modulation through the binding of rigid steroids. PLoS One. 2010;

7. Voss TC, Schiltz RL, Sung MH, Yen PM, Stamatoyannopoulos JA, Biddie SC, et al. Dynamic exchange at regulatory elements during chromatin remodeling underlies assisted loading mechanism. Cell. 2011;

8. Mader S, Kumar V, De Verneuil H, Chambon P. Three amino acids of the oestrogen receptor are essential to its ability to distinguish an oestrogen from a glucocorticoid-responsive element. Nature. 1989;

9. Paakinaho V, Presman DM, Ball DA, Johnson TA, Schiltz RL, Levitt P, et al. Single-molecule analysis of steroid receptor and cofactor action in living cells. Nat Commun. 2017;8:15896.

10. Uversky VN, Kuznetsova IM, Turoverov KK, Zaslavsky B. Intrinsically disordered proteins as crucial constituents of cellular aqueous two phase systems and coacervates. FEBS Lett. 2015;

11. Strom AR, Emelyanov A V., Mir M, Fyodorov D V., Darzacq X, Karpen GH. Phase separation drives heterochromatin domain formation. Nature. 2017;547(7662):241–5.

12. Hyman AA, Weber CA, Jülicher F. Liquid-Liquid Phase Separation in Biology. Annu Rev Cell Dev Biol [Internet]. 2014;30(1):39–58. Available from: http://www.annualreviews.org/doi/10.1146/annurev-cellbio-100913-013325

13. Sato Y, Mukai M, Ueda J, Muraki M, Stasevich TJ, Horikoshi N, et al. Genetically encoded system to track histone modification in vivo. Sci Rep. 2013;

14. Cisse II, Izeddin I, Causse SZ, Boudarene L, Senecal A, Muresan L, et al. Real-time dynamics of RNA polymerase II clustering in live human cells. Science (80-). 2013;

15. van Steensel B, Jenster G, Damm K, Brinkmann AO, van Driel R. Domains of the human androgen receptor and glucocorticoid receptor involved in binding to the nuclear matrix. J Cell Biochem. 1995;

16. Keppler BR, Archer TK, Kinyamu HK. Emerging roles of the 26S proteasome in nuclear hormone receptor-regulated transcription. Biochimica et Biophysica Acta - Gene Regulatory Mechanisms. 2011.

17. Kadmiel M, Cidlowski JA. Glucocorticoid receptor signaling in health and disease. Vol. 34, Trends in Pharmacological Sciences. 2013. p. 518–30.

18. Petta I, Dejager L, Ballegeer M, Lievens S, Tavernier J, De Bosscher K, et al. The Interactome of the Glucocorticoid Receptor and Its Influence on the Actions of Glucocorticoids in Combatting Inflammatory and Infectious Diseases. Microbiol Mol Biol Rev [Internet]. 2016;80(2):495–522. Available from: http://mmbr.asm.org/lookup/doi/10.1128/MMBR.00064-15

19. Stavreva D a, Müller WG, Hager GL, Smith CL, McNally JG. Rapid glucocorticoid receptor exchange at a promoter is coupled to transcription and regulated by chaperones and proteasomes. Mol Cell Biol. 2004;24(7):2682–97.

20. Freeman BC, Yamamoto KR. Disassembly of transcriptional regulatory complexes by molecular chaperones. Science. 2002;

21. Luby-Phelps K. The physical chemistry of cytoplasm and its influence on cell function: an update. Mol Biol Cell [Internet]. American Society for Cell Biology; 2013 Sep [cited 2017 Dec 11];24(17):2593–6. Available from: http://www.ncbi.nlm.nih.gov/pubmed/23989722

22. Fushimi K, Verkman AS. Low viscosity in the aqueous domain of cell cytoplasm measured by picosecond polarization microfluorimetry. J Cell Biol [Internet]. The Rockefeller University Press; 1991 Feb [cited 2017 Dec 11];112(4):719–25. Available from: http://www.ncbi.nlm.nih.gov/pubmed/1993739

23. Huff TB, Hansen MN, Zhao Y, Cheng J, Wei A. Controlling the Cellular Uptake of Gold Nanorods Controlling the Cellular Uptake of Gold Nanorods Controlling the Cellular Uptake of Gold Nanorods. Langmuir. 2010;23(4):1–6.

24. Pante N, Kann M. Nuclear Pore Complex Is Able to Transport Macromolecules with Diameters of 39 nm. Mol Biol Cell [Internet]. 2002;13(2):425–34. Available from: http://www.molbiolcell.org/cgi/doi/10.1091/mbc.01-06-0308

SAMENVATTING

De aanmaak van eiwitten is essentieel voor het functioneren van ons lichaam. De blauwdruk voor deze eiwitten ligt opgeslagen in ons DNA. Om de juiste eiwitten te maken binden transcriptiefactoren aan specifieke sequenties in het DNA om de aanmaak te initiëren (zoals geïllustreerd in figuur 1). Een van de intrigerende vragen met betrekking tot transcriptie is hoe de dynamica en distributie van transcriptiefactoren bijdragen aan hun functie. Om dit te onderzoeken hebben wij de glucocorticoïd receptor (GR) gebruikt, een transscriptie factor die vaak bij onderzoek wordt ingezet. De GR maakt onderdeel uit van de familie van steroïde-receptoren en functioneert als stress-receptor. Wanneer een stress-signaal van de hersenen naar de bijnier wordt gezonden, wordt er cortisol aangemaakt (zoals geïllustreerd in figuur 2). Cortisol verdeelt zich over het lichaam via de bloedbaan en wanneer het de cellen binnen komt, bindt het aan de GR. Activatie van de GR zorgt voor translocatie van het cytoplasma naar de kern van de cel waar het DNA ligt opgeslagen. Hoe de GR vervolgens zijn bindingsmotief van 6 baseparen vindt in de zee van 6 miljard baseparen, dat ons genoom telt, is onderwerp van onderzoek en blijft vooralsnog onduidelijk (zoals geïllustreerd in figuur 3). Om dit te onderzoeken hebben wij in dit proefschrift op verschillende wijzen gewerkt aan het vergroten van zowel het biologisch inzicht als de methodologische vooruitgang om meer inzicht te kunnen vergaren.

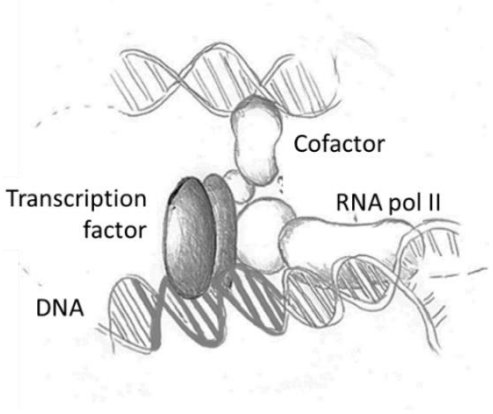

Figuur 1. Transcriptie initiatie. Transcriptie factoren binden aan een specifieke DNA sequentie (hier in donker grijs aangegeven). Vervolgens worden er verschillende cofactoren gerekruteerd. Samen zorgen deze ervoor dat het DNA meer toegankelijk word voor zover het dat nog niet was en kan RNA polymerase II (RNA pol II) binden. Deze initieert de transcriptie, waarbij de DNA streng deels uit elkaar word gewikkeld en er RNA kan worden gemaakt. Deze wordt uiteindelijk omgezet in eiwitten die allerlei functies in ons lichaam uitvoeren.

We hebben daarmee een raamwerk gecreëerd om de ruimtelijke en temporele distributie van de GR in de kern van levende cellen beter te begrijpen om zo inzicht te krijgen hoe de aanmaak van eiwitten word gereguleerd op dit niveau. Om ruimtelijke en temporele informatie over de GR te verkrijgen moeten we deze visualiseren. Dat is gedaan door er een fluorescent eiwit aan te verbinden. Wanneer er licht op fluorescente eiwitten valt of schijnt, zenden zij zelf ook licht uit, maar in een andere kleur. Door dit licht via de camera vast te leggen kunnen wij de positie van de GR zeer nauwkeurig bepalen. In deze thesis hebben we gebruik gemaakt van verschillende microscopie technieken om met behulp van fluorescente eiwitten de GR in de kern van de levende cel te kunnen filmen en fotograferen.

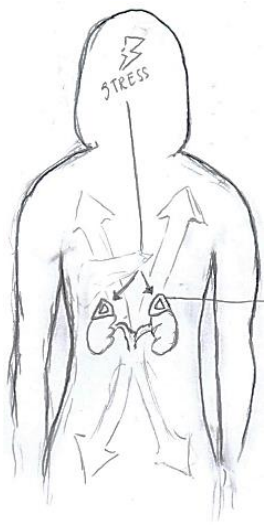

Figuur 2. Stress signalering. Wanneer wij stress ervaren kunnen er via de zogenaamde HPA-as hormonen worden gestuurd naar de bijnier (dunne pijlen naar driehoek vormige bijnier bovenop de nieren). De bijnier produceert dan cortisol. Cortisol wordt vervolgens via het bloed verspreid over het hele lichaam (brede pijlen).

Er is gebruik gemaakt van single-molecule microscopie en fluorescencie recovery after photobleaching (FRAP), zoals in hoofdstuk 2 wordt beschreven. Met behulp van single-molecule microscopie konden we de diffusie van individuele moleculen observeren. FRAP, daarentegen, is beter geschikt voor het observeren van bindingen. Door beide technieken te combineren kregen we een overzicht van twee bindingstypen en twee diffusiemodi van de GR. De overstap van de GR van de ene modus naar de

andere is niet direct te observeren. Om ook de transities tussen de verschillende modi in kaart te brengen hebben we een continuous time Markov chain model ontwikkeld. Hieruit bleek dat de GR voorkeur heeft voor bepaalde transities.

Door de verschillende DNA-bindende mutanten te bestuderen ontdekten wij welke van deze modi afhankelijk waren van DNA binding. In totaal hebben we zes mutanten gebruikt die een breed scala aan affiniteiten voor DNA hebben. Zo hebben we twee mutanten gebruikt die via een aminozuur niet aan het specifieke DNA-motief konden binden, twee mutanten die verminderd aspecifieke bindingen konden maken, een mutant waarvan de 3D-structuur binnen het DNA bindend domein was verstoord en een mutant die het volledige domein voor DNA binding miste. Samen representeren deze mutanten een scala aan affiniteiten voor DNA.

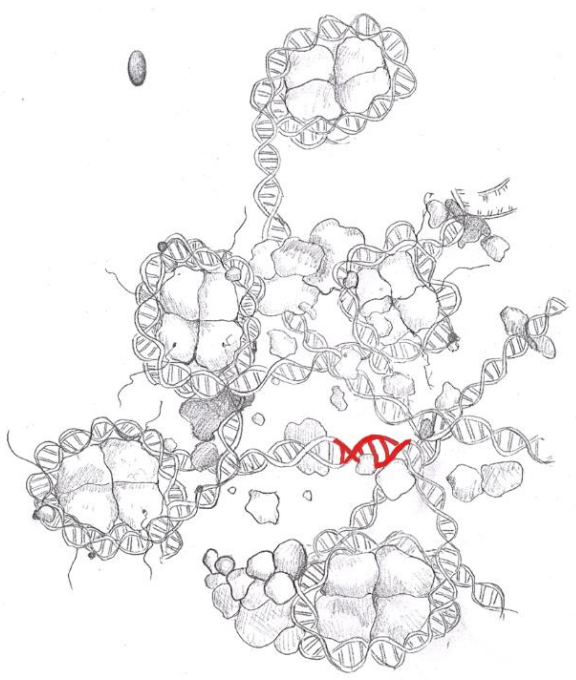

Figuur 3. Illustratie van het paradigma. Hoe kan een transcriptie-factor zoals de GR (ovaal links boven) zijn specifieke bindings-site (rood) binden, op en efficiënte manier tussen al het andere DNA en eiwitten in de kern?

Hierdoor kwamen we er ten eerste achter dat de lange bindingstijden volledig afhankelijk waren van binding aan specifieke DNA motieven. Het is goed mogelijk dat we hiermee de bindingstijden hebben geïdentificeerd die nodig zijn om de aanmaak van eiwit te initiëren. Ten tweede bleek dat de korte bindingstijden volledig onafhankelijk waren van het DNA bindende domein. Dit suggereert indirecte binding aan DNA. Het is bekend dat de GR kan binden aan andere transcriptiefactoren die aan DNA gebonden zijn om zo hun functie te beïnvloeden. Het was echter onbekend dat deze functie van de GR geassocieerd zou kunnen zijn met andere bindingstijden. Ten derde was de langzame diffusie gedeeltelijk afhankelijk van niet specifieke interacties DNA. Dit impliceert dat dit type diffusie korte interacties met het DNA aan kan gaan in de gehele kern van de cel, mogelijk door elektrostatische interacties. Mogelijk is dit een manier om te vertragen waardoor interacties met specifieke bindingsplaatsen (direct dan wel indirect) worden vergemakkelijkt. Ten slotte was de snelle diffusiemodus volledig onafhankelijk van DNA-binding. Wij nemen aan dat dit vrije diffusie is. De kans op transities tussen de vier modi was niet afhankelijk van DNA binding, wat impliceert dat deze transities worden veroorzaakt door een ander mechanisme.

Op basis van deze informatie over de verschillende modi en de transities komt een duidelijk mechanisme naar voren dat de GR gebruikt om zijn functie uit te oefenen (zoals geïllustreerd in figuur 4). Na lang vrij te diffunderen is er een grote kans om eerst langzaam te diffunderen en vervolgens korte dan wel lange bindingen uit te voeren. De GR switcht meerdere keren tussen langzame diffusie en binding. Zodoende kan de receptor lokaal zijn functie uitvoeren. Dit alles leidt tot een effectieve manier van vinden en binden van de receptor.

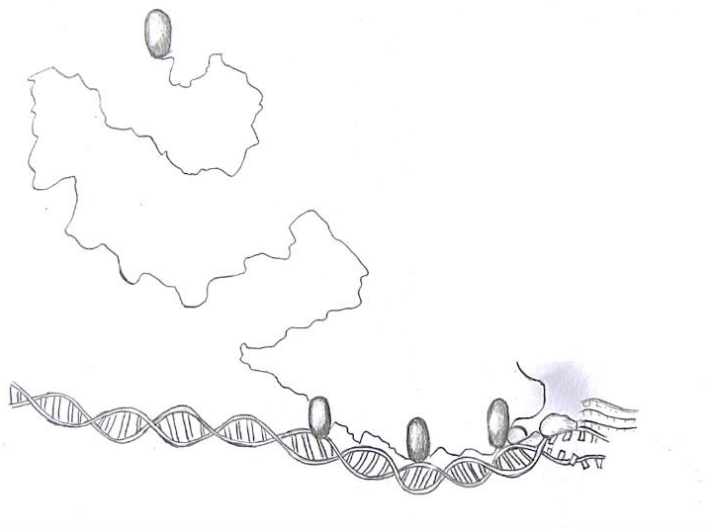

Figuur 4. Diffusie en binding van de GR. Resultaten uit hoofdstuk 2 van dit proefschrift wijzen uit dat de GR voor een langere periode (meer dan tien seconden gemiddeld) vrij beweegt door de kern van de cel zonder interacties met het DNA. Wanneer de GR een switch maakt vertoont hij daarna korte, zwakke interacties met DNA (hij beweegt als het ware langs het DNA). Deze langzame beweging wordt afgewisseld met bindingen aan DNA die direct (3 seconden) of indirect (0.6 seconden, via andere eiwitten) kunnen zijn.

Om single-molecule data beter te kunnen interpreteren hebben we een nieuwe methode ontwikkeld om de fractie GR-moleculen dat diffundeert beter te kunnen corrigeren op langere tijdschalen. Dit wordt beschreven in **hoofdstuk 3**. Met deze nieuwe methode konden we bepalen op wat voor tijdschalen de transities tussen modi voorkomen. Doordat we met de gebruikte microscoop een (tweedimensionaal) vlak bekijken in een (driedimensionale) cellulaire kern, verliezen we snel diffunderende moleculen sneller uit beeld dan gebonden moleculen (zoals geïllustreerd in figuur 1 van hoofdstuk 3 (blz.76)). Daarom dragen we een analytische oplossing aan voor een systeem met twee populaties om hiervoor te corrigeren. Deze is gebaseerd op de kans dat een molecuul binnen het twee dimensionale vlak blijft dat voor ons zichtbaar is. Op deze manier konden we de fractie diffunderende moleculen corrigeren voor het verlies van moleculen ten opzichte van de immobiele moleculen. Dit hebben we gedaan tot een tijdschaal van 150 milliseconden. Waar eerder het percentage

moleculen in de diffunderende fractie afnam in de tijd, bleek na correctie dat deze juist stabiel blijft op deze tijdschaal. Dit duidt erop dat er geen veranderingen plaatsvinden op deze tijdschaal en er dus geen transities plaatsvinden. Dit komt overeen met onze bevindingen in hoofdstuk 2 waar het ons niet lukte om de transities te visualiseren, maar waar we een model hebben ingezet om deze transities te bestuderen. Uit de analyse met behulp van het model bleek dat de transities op een tijdschaal van 600 milliseconden tot meerdere seconden moest plaatsvinden.

Daarnaast hebben we gekeken naar de distributie van de GR in de kern. Op basis van de resultaten uit hoofdstuk 2 verwachtten we dat er regio's in de kern van de cel zijn waar de receptor langzaam diffundeert en bindt. We weten ook uit vorige bevindingen dat er clusters van de GR aanwezig zijn in de kern, maar deze zijn tot nu toe nog niet uitvoerig gekwantificeerd (1,2). Daarom beschrijven we in **hoofdstuk 4** de kwantitatieve analyse van GR clustering en vergelijken we deze met een nauw verwante hormoon receptor namelijk de oestrogeen receptor (ER) (afbeeldingen van de distributie van de GR en ER in de kern van de cel zijn te zien in figuur 1 van hoofdstuk 4 (blz. 95)). Door op hoge resolutie afbeeldingen te maken en hierin individuele clusters te identificeren, konden we het aantal, de grootte en relatieve aantal moleculen in de clusters bepalen. De clusters van de GR waren beduidend groter dan die van de ER. Daarnaast waren er significant minder GR clusters dan ER clusters. Dit wijst erop dat de GR en ER clusters aparte entiteiten zijn. De hypothese is dat deze clusters verband houden met specifieke bindingen aan DNA. Het zou kunnen dat er lokaal meerdere bindingsplaatsen aanwezig zijn of dat er andere factoren zijn waardoor de receptor lokaal blijft.

Om dit verder te onderzoeken hebben we gebruik gemaakt van het feit dat deze receptoren nauw verwant zijn. Eerder onderzoek had al laten zien dat het verwisselen van drie aminozuren (bouwstenen) in het DNA bindende domein van deze receptoren ervoor zorgt dat de GR het bindingsmotief van de ER aan het DNA herkent en vice versa (3,4). Dit bleek echter geen effect te hebben op de clustervorming van de GR of de ER. Het is goed mogelijk dat ~~al~~hoewel cluster formatie afhankelijk is van het DNA bindende domein (zoals eerder onderzoek uitwijst), andere cofactoren een belangrijke rol spelen in

de uiteindelijke vorm van het cluster. Om dit mechanisme beter te kunnen begrijpen is het van belang om ruimtelijke en temporele informatie te combineren. Uiteindelijk zal het voor ons begrip van GR-dynamica van essentieel belang zijn om de GR voor langere tijd te kunnen volgen, waardoor we de transities beter in kaart te kunnen brengen.

Idealiter zouden we de receptor willen volgen gedurende enkele bindingscycli. Dit vereist microscopie op de tijdschaal van minuten met een zeer korte tijd tussen de opeenvolgende beelden (kleiner dan 5 milliseconden). De labels die op dit moment gebruikt worden om eiwitten, zoals de GR, die zelf niet gekleurd zijn zichtbaar te maken, zijn hiervoor niet geschikt. Deze labels verbleken snel en knipperen, waardoor het lastig is om deze te volgen. Om toegang te krijgen tot langere tijdschalen moeten we nieuwe methoden ontwikkelen waarmee we de GR langer kunnen volgen. Hiervoor hebben we het gebruik van gouden nanodeeltjes onderzocht als labelings methode voor eiwitten zoals de GR. In **hoofdstuk 5** wordt hiervan verslag gedaan. Gouden nanodeeltjes knipperen en verbleken niet en zijn gemakkelijk te gebruiken als label. Om in kaart te brengen hoe deze nanodeeltjes zich gedragen in cellen, hebben wij ze geïnjecteerd in de kern of in het cytoplasma van de cel. Het bleek dat deze deeltjes veel langzamer bewogen dan verwacht werd. Ook was het opvallend dat zij niet van het cytoplasma naar de kern of andersom gingen. Om te functioneren als label voor de GR is het namelijk essentieel dat deze deeltjes in het cytoplasma aan de GR worden gekoppeld en niet uit zichzelf naar de kern kunnen. Echter wanneer de GR naar de kern gaat waar het deeltje aan vast zit, moet het wel door de poriën van de kern kunnen. Om dit te testen koppelden wij een nucleair lokalisatie-signaal aan de gouden deeltjes en injecteerden wij deze in het cytoplasma. Hierna gingen de deeltjes wel naar de kern. Ondanks dat dit vrij snel gebeurde (binnen 30 minuten), waren er maar weinig deeltjes die dit deden (ongeveer 10%). Wel konden we hiermee laten zien dat gouden nanodeeltjes uiteindelijk wel geschikt zouden kunnen zijn als label voor de GR, maar dat deze nog wel geoptimaliseerd zouden kunnen worden.

TOEKOMSTPERSPECTIEF

Deze thesis biedt een raamwerk voor het onderzoek naar transcriptie factoren zoals de GR. In het bijzonder komt naar voren dat het essentieel is om de processen die hierbij een rol spelen zorgvuldig te kwantificeren. Om dit te kunnen blijven doen is het van belang om analyse technieken te blijven ontwikkelen. Daarnaast zal het koppelen van ruimtelijke en temporele informatie in de kern een belangrijk doel zijn. Specifiek het koppelen van informatie over clusters en de diffusie en binding van de receptor met het DNA en de staat daarvan zal een belangrijk doel van studie voor de toekomst zijn. Om dit te bereiken is het belangrijk om op het niveau van een enkel molecuul te kunnen kijken en dit voor langere tijd te kunnen volgen. Methodes die hieraan bijdragen dienen in ontwikkeling te blijven.

CURRICULUM VITAE

Veer Keizer was born on the 16th of February 1989 in Utrecht, The Netherlands. She attended secondary school at the Marnix College in Ede and obtained her bilingual VWO diploma in 2007. During this period, she also obtained her International Baccalaureate in English. In 2007 she started her studies in Beta-Gamma at the University of Amsterdam with a major in Biomedical Sciences. During this period she performed an internship entitled "Whole blood model for sepsis" under the supervision of Dr. C. van 't Veer at the Amsterdam Medical Center. This period was successfully concluded with a BSc degree in 2010. In this period, she also obtained a minor in Biochemistry. From 2010 to 2012, she studied Biomedical Science to obtain a MSc degree (cum laude). This included an internship entitled "Amino acid signaling in autophagy" under the supervision of Dr. A.J. Verhoeven at the Amsterdam Medical Center. In addition she completed an internship at Weill Cornel Medical College in New York, entitled "Intracellular trafficking of the Insulin receptor" under the supervision of Dr. T.E. McGraw. From 2009 to 2011 she taught Chemistry at the Martinus College in Grootebroek. In 2012, she started her PhD research at the Institute of Biology of Leiden University. From 2013 to 2015, she was Vice President of the Central Works Council of FOM, NWO. In November 2017, she started her postdoctoral research in the laboratory of Dr. Maxime Dahan at Institut Curie in Paris.

LIST OF PUBLICATIONS

Veer I.P. Keizer, Stefano Coppola, Adriaan B. Houtsmuller, Bart Geverts, Martin E. van Royen, Thomas Schmidt, Marcel J.M. Schaaf: Repetitive switching between DNA binding modes enables target finding by the glucocorticoid receptor, *submitted*, 2018.

Carattino A., Keizer V.I.P., Schaaf M.J.M., Orrit M.A.G.J.: Background Suppression in Imaging Gold Nanorods through Detection of Anti-Stokes Emission, Biophysical Journal, 2016.

Harkes R.*, Keizer V.I.P.*, Schaaf M.J.M., Schmidt T.S.: Depth-of-focus correction in single molecule data allows analysis of 3D diffusion of the glucocorticoid receptor in the nucleus. PLoS One, 2015. * Authors contributed equally.

Groeneweg F., van Royen M.E., Fenz S., Keizer V.I.P., Gevers B., Prins, J., de Kloet E.R., Houtsmuller A.B., Schmidt T.S., Schaaf, M.J.M.: Quantitation of Glucocortioid Receptor DNA-binding Dynamics by Single-Molecule Microscopy and FRAP. PLoS One, 2014.

Veer I.P. Keizer, Stefano Coppola, Thomas Schmidt, Marcel J.M. Schaaf: Differences in glucocorticoid receptor and estrogen receptor intranuclear distribution, *in preparation*, 2018.